STRUCTURAL ORDERING IN SEMICONDUCTING ORGANIC MOLECULES OR POLYMERS

Thesis submitted to the University of Calcutta

for the degree of Doctor of Philosophy (Science)

in Physics

BY

ISHANI ROY

UNIVERSITY OF CALCUTTA

October 2015

To my parents

ACKNOWLEDGEMENT

As I look back at the years of my Ph.D. life at Saha Institute of Nuclear Physics, I feel thankful to the many people who have made it possible for me to write this thesis, despite the road being a rocky one. Their ceaseless help and support has been the biggest driving force behind the successful completion of this doctoral research work. First of all I must thank my Ph.D. supervisor, Prof. Satyajit Hazra, for introducing me to the world of conducting polymers and the exciting techniques of X-ray scattering. His guidance and valuable suggestions regarding experimental matters will always be gratefully acknowledged. I am deeply indebted to my seniors, Jayanta-da and Paramita-di, for teaching me the basics of the experimental procedures and helping me out with their invaluable suggestions whenever I asked for it. I express my sincere gratitude to Prof. Alokmay Datta and Prof. P.M.G. Nambissan for extending the UV-vis spectroscopy facilities, Prof. Manabendra Mukherjee for providing DLS facility, Dr. S.V. Roth for his help in GISAXS measurements at PETRA-III, DESY and Dr. Srihari Valega and Dr. Sanjay Singh for their help in carrying out experiments at Photon Factory, KEK. I must also thank Prof. Supratic Chakraborty for the DSC facility, Dr. B. Satpati for TEM and Prof. S. Bhunia for PL spectroscopy facility. The financial supports received from SINP under the DST-DESY and DST-KEK projects

for carrying out experiments at DESY, Germany and KEK, Japan are thankfully acknowledged. I would like to thank the Center for Research in Nanoscience and Nanotechnology, University of Calcutta for providing the SEM facility, and Prof. Debnarayan Jana of University of Calcutta for providing PL spectroscopy facility. I will be ever so grateful to my seniors at the Surface Physics and Material Science Division—Maidul-da, Abhisakh-da, Santanu-da, Nupur-di, Tanusree-di and Manjula-di for every little help I have received from them during the early years of my Ph.D. Sumona, Mala and Sruti have been more than just lab-mates for me—without them life at '126' would not have been so enjoyable. These three, along with Sudipta, have made the everyday tea-times to be remembered for years to come. Mala needs special mention for devoting so much of her precious time working with me, helping me with the AFM, and doing me small and big favors whenever there was a need. I take this opportunity to thank Goutam-da for his assistance in several technical matters, Ms. Soma Roy for helping with UV-vis measurements, Haren-da and Gobardhan-da for helping in various non-academic matters, and Mukul-da, Manoj-da and Subhashis-da for making official procedures simpler for me. There are, of course, many more people in my division and institute than I have mentioned here, who have helped me in some way or the other during the years I have spent at SINP. My sincere apologies to them for not mentioning them individually. Lastly, I must thank my parents who have been my main motivation for continuing with higher studies and without whose wholehearted support and encouragement I would never have been able to complete my doctoral research. I am also thankful to my husband Somdeb who has been by my side through thick and thin, and has given me all the help he could in both academic and non-academic matters.

Kolkata, October 2015 *Ishani Roy*

CONTENTS

CHAPTER 1

PROLOGUE

1.1 Foreword

"There's plenty of room at the bottom"

–Richard Feynman, 1959.

It was these words of Feynman that triggered the modern concept of *nanotechnology*. Feynman talked about manipulating or controlling matter on a small scale, in particular, controlling the arrangement of individual molecules or atoms. In fact, the last couple of decades have seen an enormous growth in the field of nanotechnology as foreseen by him way back in 1959. *Nanomaterials* are materials whose units are sized between 1 and 1000 nm in at least one dimension. The reduction in size can be in all three dimensions as in case of *quantum dots*, or in two dimensions as in *nanowires*, or in only one dimension as in *thin films*. The discovery of a wide variety of nanomaterials, offering fascinating mechanical, optical and electronic properties, has taken material science to amazing new heights.

Organic molecules, both small molecules and polymers, have emerged as prospective candidates for application in 2-dimensional thin films having interesting semiconducting and optical properties. They surpass the efficacy of silicon-based devices as they combine the semiconducting property of inorganic semiconductors with the mechanical properties of organic materials. For example, an organic thin film transistor can be as thin as a few hundred nanometers, compared to around 20 μm for the thinnest silicon based transistor, and they are flexible enough to withstand repeated deformation. Moreover, they operate at remarkably low voltages. Another reason for the soaring interest in organic thin film devices is that they can be fabricated using much less complicated processes compared with conventional Si technology involving high-temperature and high-vacuum deposition processes and sophisticated photolithographic patterning methods. Organic devices can, in general, be prepared by low-temperature deposition and solution processing instead of the more complicated processes involved in fabricating Si-based devices [1]. To earn the maximum possible benefit from organic thin films devices, highly ordered layers of organic small molecules and polymers are needed. Such ordered organic layers find their uses not only in electronic devices, but also in biological membranes, corrosion protection, electrochemistry, etc. In this thesis work, however, we have concentrated only on the ordering of polymers, having semiconducting properties, in thin films on a substrate.

Semiconductors, ever since their inception, have been an indispensable part of the technological progress of mankind. It is because of them that our need to communicate and process data could have been simplified beyond imagination. Extensive research on semiconducting materials have ushered in an era of immense technological advancement in terms of innovative electronic devices. Semiconductors have undergone a massive evolution over time — from elements like silicon and germanium to compounds like GaAs, oxides and organic molecules. The state-of-the-art is molecular electronics, which operates

in the quantum regime, and has gained supreme importance in the post-microelectronics days. Microelectronics uses silicon as the preferred material and photolithography as the fabrication technique. Devices can be made to operate faster by decreasing their size. However, as devices become faster and smaller, problems related to removal of heat dissipated by the transistors and physical limitations to keep two binary states arise. This has led to the search for new alternatives using components fabricated by other procedures such as self-assembly and chemical deposition, which may encode information using lower energetic means. In the attempt to reduce the size of electronic circuits, devices are being fabricated using the bottom-up approach, that is, by using single molecules or small ensembles of molecules. This has paved the way for the extremely important field of molecular electronics, which mostly uses single molecules, small groups of molecules, carbon nanotubes, or nanoscale metallic or semiconductor wires in the active layer [2].

Organic semiconducting materials serve as a low-cost alternative to inorganic semiconductors for applications in devices such as organic thin film transistors (OTFTs) [3, 4], light-emitting diodes (OLEDs) [5, 6], solar cells [7, 8], sensors, and radio frequency identification (RF-ID) tags for integration into low-cost, large-area electronics [9]. These organic materials are typically π-conjugated molecules and polymers substituted with solubilizing alkyl side groups when needed. Since they are compatible with solution-processing techniques, they eliminate the need for expensive lithography and vacuum deposition steps, which are compulsory for inorganic semiconducting devices. Structural ordering in these semiconducting organic materials is of utmost importance as it plays a key role in controlling the device performance. Thus, controlling the orientation and ordering of organic small molecules and polymers in the active layer has become a topic of intense research in the recent years [10–13].

Unlike metal, oxide and semiconductor surfaces, organic materials cannot be organized

into ordered surfaces by orienting, cutting (or cleaving), and polishing single crystal substrates and subsequent cleaning in ultra high vacuum (UHV) by ion bombardment, as they are usually soft and tend to sublime readily if placed in UHV [14]. Thus, surfaces of organic molecules or polymers typically exhibit a lower degree of order and lower thermal stability than inorganic surfaces. They are also difficult to characterize by electron or ion scattering techniques as they are easily affected by radiation damage. However, recent developments in the field of organic thin film preparation, like Langmuir-Blodgett technique, self assembly, organic vapor phase deposition, etc. have provided efficient means of preparing remarkably ordered organic surfaces. In addition, innovations in non-destructive characterization techniques have conquered the shortcoming of radiation damages. These techniques include Scanning Probe Microscopy (SPM) for mapping the surface topography, X-ray scattering techniques such as X-ray Reflectivity (XR) and Grazing Incidence X-ray Scattering (GIXS) for measuring the thickness and order in thin films, spectroscopic techniques such as Near-Edge X-ray Absorption Fine Structure Spectroscopy (NEXAFS), X-ray and Ultraviolet Photoelectron Spectroscopies (XPS and UPS) for probing the electronic structure of metal-organic semiconductor interfaces, Ultra-violet and Visible Absorption Spectroscopy (UV-vis) for knowing the molecular packing and electronic structure, etc [15]. The added effect of such fabrication and characterization methods has manifested itself in an enormous progress in the field of organic electronics in the recent years.

Among the host of organic molecules that have shown considerable importance as semiconducting materials, π-conjugated polythiophenes deserve special mention owing to their outstanding optical and electronic properties. Often, alkyl chains are incorporated into polythiophene molecules to make them soluble in common organic solvents and thus facilitate simple solution processing techniques for device fabrication. These *poly(3-alkylthiophenes)* or *P3ATs* tend to crystallize into lamellar stacks, along with some amor-

phous interlamellar regions, in thin films. The degree of ordering in these stacks and their orientation on a substrate are of prime importance in the performance of devices using them in the active layer. The mechanism of ordering in these polymers is the focus of our work in this dissertation. In particular, we concentrate on *poly(3-dodecylthiophene)* or *P3DDT* which has a 12-membered alkyl side chain. The orientation and ordering in P3DDT thin films have been studied using two different fabrication methods as well as two types of casting solutions, and the structures thus obtained have been correlated to the different processing parameters. Finally we briefly investigate the effect of post-deposition treatments like solvent vapour and thermal annealing on thin films of P3DDT. Structure characterization has been done mainly using different X-ray scattering techniques, along with other techniques like atomic force microscopy, dynamic light scattering and UV-vis spectroscopy.

1.2 Outline of the thesis

Here we briefly describe the plan of this thesis in order to help the reader maneuver through it. The following chapter (Chapter 2) gives an introduction to the vast subject of conducting polymers and their uses as semiconducting materials in devices like thin film transistors, solar cells, light-emitting diodes, etc. The particular class of polymer used in our works is also described in this chapter and its importance in the field of organic electronics is elaborated. Moreover, a brief review of previous works using such materials is presented in this chapter. Chapter 3 deals with the various experimental methods used. Here we describe the sample preparation procedures as well as the characterization techniques used to understand their morphology. Brief discussions are made on the basic principles underlying the techniques and also the instruments used to carry out the measurements.

The rest of the thesis is devoted to the experimental findings of our studies. Firstly, in Chapter 4, we present the results we have obtained for thin films of P3DDT prepared from a single good solvent, i.e., a solvent in which the polymer exhibits good solubility, by using spin-coating technique. Three different solvents have been used and the concentration of the solutions varied in order to investigate their effect on the films' morphology. Dependence of morphology on spinning speed and substrate nature is also presented here. We also mention briefly the dependence of film thickness on the concentration of the casting solution.

Chapter 5 concerns P3DDT films prepared from solutions in a mixture of a good and a poor solvent. These films have been prepared by drop-casting method. In this chapter we discuss the effect of solvent mixing on the morphology of the films and determine the optimal mixing ratio for obtaining well ordered P3DDT lamellae. Thereafter we examine the effect of thermal annealing on these films in order to ascertain the optimal annealing temperature for forming P3DDT lamellae with considerably good crystallinity as well as directionality.

Lastly, in Chapter 6, we demonstrate the effects of solvent vapour and thermal annealing on the morphology of spin-coated P3DDT films. *In-situ* XR studies have been carried out to monitor the time evolution of the morphology during solvent vapour annealing (SVA). The influence of subsequent drying by annealing on the crystallinity of the films has also been studied in order to determine whether there is any improvement in this regard due to such post-deposition treatments.

We wrap up this thesis by summarizing the main points we have gathered through our studies and mentioning some of the future avenues that our work might lead to.

CHAPTER 2

SEMICONDUCTING ORGANIC THIN FILMS: THE BEGINNING AND THE FUTURE

In this chapter we lay the foundation for the rest of the thesis by giving a short introduction to conducting polymers, the mechanism of ordering in these polymers and how the ordering affects the charge transfer processes. Thereafter we introduce the reader to the class of polymers of our interest, namely, poly(3-alkylthiophenes) or P3ATs, their structural characteristics and their uses in organic electronic devices.

2.1 Conducting polymers: A primer

Conducting polymers were discovered by Alan J. Heeger, Alan MacDiarmid and Hideki Shirakawa in 1976 for which they were awarded the Nobel Prize for chemistry in 2000.

The discovery that the conductivity of these polymers could be tuned over the entire range from insulators to metals by doping paved the way for new research and technology that could not have been imagined before. Besides creating the possibility to explore several unsolved mysteries of chemistry and condensed matter physics, they also opened the door to a completely new class of materials, "materials that exhibit the electrical and optical properties of metals or semiconductors and that retain the attractive mechanical properties and processing advantages of polymers", as stated by Heeger himself in his Nobel lecture in 2000 [16].

The polymers of interest in this respect are the *conjugated polymers* which have an electronic configuration distinctly different from saturated polymers. In saturated polymers all four valence electrons of the carbon atoms take part in covalent bonds, whereas in conjugated polymers there is one unpaired electron (the π-electron) per carbon atom. The orbitals of the successive carbon atoms along the polymer backbone overlap, which is known as π-bonding, and which eventually leads to delocalization of electrons along the backbone. This electron delocalization is responsible for the charge carrier mobility along the polymer backbone. So, the chain symmetry, i.e., the number and type of atoms within the repeat unit, decides the electronic properties of a conjugated polymer and as a consequence these polymers can exhibit semiconducting or even metallic properties. This control over the electrical conductivity over the entire range from metal to insulator can be achieved by chemical or electrochemical doping. Doping introduces charge carriers in the polymer and the ability of these charge carriers to move along the π-bonded paths results in the electrical conductivity of the polymer. Conjugated polymers are interesting to study even in the undoped state as they pave the way for what we know as *plastic electronic* devices. These include organic light emitting diodes (OLEDs), photovoltaic cells, lasers, organic thin film transistors (OTFTs) and much more. All these devices use in their active

layer a thin film of conjugated polymer deposited from its solution. Solution processability is, in fact, a big advantage of using these polymers as it reduces the hassles of film deposition to a great extent. Disorder in conjugated polymer systems is, however, a stumbling block in the way to achieve high charge carrier mobility, and hence, high electrical conductivity. It has been shown that improving the chain extension and chain alignment not only improves the conductivity but also the mechanical properties of conjugated polymers. In this connection it is noteworthy that organic small molecules do not suffer from this drawback since they can be vacuum evaporated to form extremely well ordered polycrystalline deposits showing better electrical conductivity than solution processed thin films [9]. The need for ordered polymer films has thus resulted in a huge amount of research aimed at preparing conjugated polymer systems with a high degree of structural order.

2.2 Ordering in conjugated polymer films

Polymers crystallize in a peculiar way, totally different from the mechanism of crystallization in oligomers. In fact, polymers are able to crystallize only partially, i.e., there are crystalline regions separated by disordered amorphous regions. Oligomers readily crystallize into stacked layers where each layer is assembled of chain molecules with identical helical conformations and the endgroups of the molecules form the interfaces. In a crystallizable polymer, on the other hand, a separation process takes place whereby chains that can be stretched and added to a growing crystal are separated from chains near entangled parts that can only be removed to the amorphous regions. The amorphous part also contains endgroups, chemical perturbations like short chain branches, or stereo defects [17].

The electronic properties of conjugated polymer films originate from the stepwise bottom-up construction of π-conjugated units at the molecular level into continuous paths for

charge transport at the mesoscopic, microscopic or even macroscopic levels. For the majority of conjugated polymers the intrachain conjugation is responsible for the delocalozation of the π-electrons and the interchain interactions for their overlap between adjacent backbones. In some conjugated polymers with flexible main-chains such as poly(9-vinylcarbazole) the electronic conjugation is caused by the π-π interaction between pendant conjugated side groups. The prime factors affecting the charge transport in conjugated polymer films are (i) the internal order within crystalline regions in the molecular scale (1 Å–10 nm), (ii) the connectivity between these crystalline regions at the meso and macroscopic scales (10 nm–1 μm) and (iii) the amount and orientation of such crystallites in the film [18].

2.2.1 Internal order within crystalline regions

A good internal order within crystallites essentially means an extended intra-chain conjugation length and an ordered inter-chain stacking. These features can be understood by observing the UV-vis and photoluminescence (PL) spectra of the films, considering the J- and H-aggregate model. In short, a J-aggregate is one in which neighboring chromophores are oriented in a head-to-tail fashion leading to negative excitonic coupling whereby the optically allowed ($k = 0$) Frenkel exciton is at the bottom of the exciton band. On the other hand, in an H-aggregate the neighboring chromophores are oriented in a side-by side manner causing positive excitonic coupling and the $k = 0$ exciton is at the top of the exciton band [19]. When the chromophores interact electronically, the vibronic progressions in the absorption and photoluminescence spectra are distorted from the spectra of isolated chromophores and these changes in the vibronic line strength provide information about the exciton bandwidth, disorder in the system and exciton coherence length. The changes are of opposite nature in H- and J-aggregates which enables one to distinguish between the

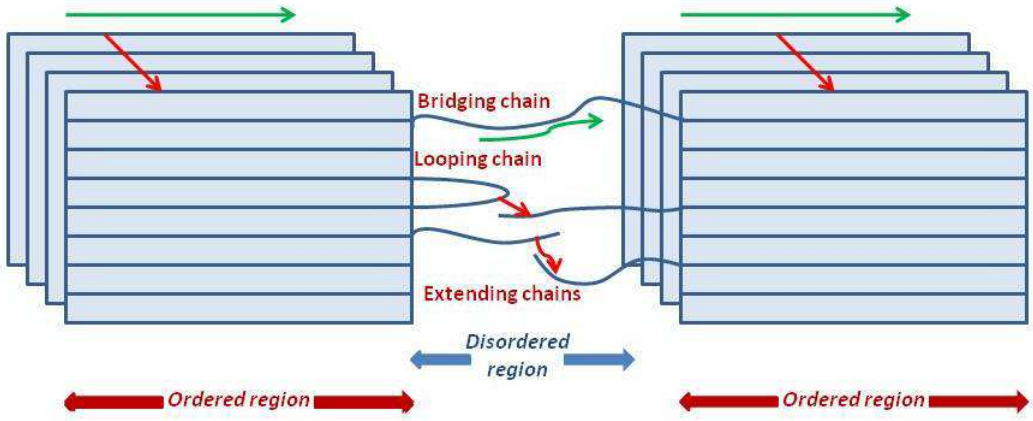

Figure 2.1: Schematic figure showing ordered and disordered regions in a semicrystalline polymer. The disordered region has three types of chains, extending, looping and bridging chains. The possible charge transport paths are shown by arrows, green arrows represent intrachain transport and red arrows represent interchain transport.

two types of aggregates. In the absorption spectrum of J-aggregates the ratio of intensities of the 0-0 and 0-1 vibronic peaks, I_A^{0-0}/I_A^{0-1}, increases with exciton bandwidth, whereas in H-aggregates the ratio decreases with exciton bandwidth. Again, in the PL spectrum the corresponding ratio, $I_{PL}^{0-0}/I_{PL}^{0-1}$, decreases in case of J-aggregates and increases in case of H-aggregates with increasing disorder. A π-stacked conjugated polymer has both J- and H-aggregate nature. This is because the intrachain head-to-tail arrangement of the repeat units favour J-type behaviour and the side-by-side arrangement of neighboring chains favour H-type behaviour. Thus, the polymer displays unique hybrid photophysical characteristics resulting from a competition between the two types of aggregates and such a π-stacked polymer aggregate is known as an HJ-aggregate [20].

2.2.2 Connectivity between crystalline regions

The connectivity between adjacent crystallites is a crucial factor in controlling the charge transport in conjugated polymer films as the presence of grain boundaries interrupts the path of the charge carriers and reduces the mobility. It has been shown that grain boundaries affect several important properties of conjugated polymer devices like activation energy, threshold voltage and field-effect mobility. An *end-to-end* connection between neighboring crystallites is beneficial for charge transport, while a *face-to-face* connection hinders charge transport. Also, the disordered regions between ordered crystallites limit the charge carrier mobility. The chains in the disordered regions connecting adjacent crystalline regions can be of three types, namely, extending, looping and bridging chains, as shown in Fig. 2.1. The presence of larger number of bridging chains than chain ends or loops is essential for efficient charge transport between crystallites as they can provide electrical pathways between crystallites. However, if these bridging chains undergo sharp bends or twists while going from one crystallite to another, there is slowing down of electrical transport due to the formation of localized states associated with the breaks in conjugation [21]. The charge transport in the disordered regions can also take place due to interchain crossover between close enough loops or chain ends. The ratio of the amount of crossing points and bridging chains actually determines the average charge carrier mobility in the disordered regions [22].

2.2.3 Amount and orientation of crystallites in the film

The total amount of crystallites present in a thin film of conjugated polymer is another important parameter in deciding the charge transport properties of the film. A larger number of crystallites in the film implies a larger number of pathways for transport of charge

carriers and fewer grain boundaries to restrict the flow of charge carriers. The amount of crystallites is reflected in X-ray diffraction (XRD) patterns where a larger amount of crystallites means an increased Bragg peak intensity. A more intense peak in the XRD pattern could also mean a larger size of the crystallites which is also beneficial for charge transport. The orientation of the crystallites on the substrate also plays an important role in controlling the charge transport in thin films. For organic photovoltaic (OPV) devices, where charge transport perpendicular to the substrate is required, the direction of π-stacking has to be in a direction normal to the substrate which is known as the *face-on* orientation. On the other hand, in field-effect transistors (FETs) charge transport should be parallel to the substrate, and hence, the π-stacking direction has to be along the substrate. This is known as the *edge-on* orientation. It has been shown that for poly(3-hexylthiophene) or P3HT based thin film transistors the mobility differs by more than a factor of 100 depending on whether the orientation is edge-on or face-on [23]. Controlling the orientation of the polymer lamellae on the substrate is thus vital in preparing efficient devices.

2.3 Poly(3-alkylthiophenes) and why they are interesting

Polythiophenes or PTs are polymerized thiophenes, which are heterocyclic aromatic compounds having the chemical formula C_4H_4S (see Fig. 2.2). The thiophene molecule has a flat five-membered ring of which one is a sulfur atom. Predominantly, the monomeric units are coupled to each other via their 2,5 positions, known as the α-α' coupling, but the presence of α-β' coupling, i.e., coupling through 2,4 positions, have also been observed. *Poly(3-alkylthiophenes)* or P3ATs are polythiophenes with alkyl chains substituted at their 3 positions. This substitution by a donor group results in a more regular structure of the polymer and makes them easily soluble in common organic solvents. An excellent

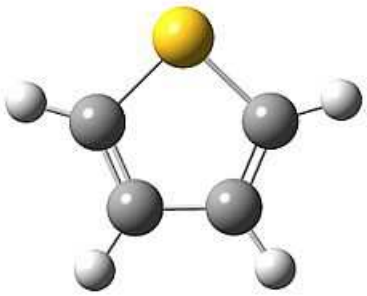

Figure 2.2: The structure of a thiophene monomer—the sulfur atom is represented by the yellow sphere, carbon atoms by bigger grey spheres and hydrogen atoms by smaller grey spheres.

review on polythiophenes can be found in Ref. [24]. P3ATs are one of the most widely studied conducting polymers. The reason behind this growing interest is not only the appreciable electrical conductivity of this class of polymers, but also their thermochromism, electrochromism, solvatochromism, ionochromism and color changes under pressure and electricity. P3ATs are easily deposited from their solutions onto solid substrates which makes them perfect candidates for applications in organic electronic devices.

2.3.1 Structural aspects of P3ATs

Several groups have investigated the structure of P3AT molecules [25, 26] and the general agreement is that these materials are semicrystalline in nature as concluded from the presence of a strong Bragg peak in their XRD patterns. Their crystalline structure is shown in Fig. 2.3, where d is the separation between consecutive polythiophene backbones along the alkyl side chain direction. The chemical incompatibility between the alkyl side chains and the polythiophene backbone is responsible for the crystalline ordering of the polymer [27, 28]. The P3AT molecule adopts a comblike structure with the flexible alkyl chains on both sides of the polythiophene backbone [29]. These alkyl chains play the role of

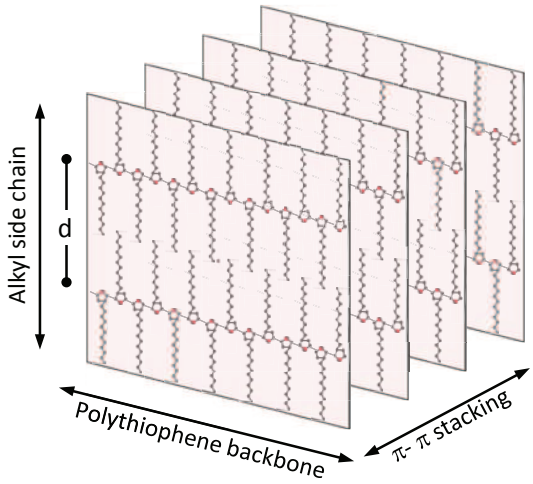

Figure 2.3: Schematic of the P3AT crystallite structure, showing π-π stacking, polythiophene backbone (or conjugation) and alkyl side chain directions, and also separation (d) between alternate layers of polythiophene backbones along alkyl side chains.

spacers between the comparatively stiffer polythiophene backbones, where the distance between two backbones is decided by the length of the alkyl chain. The side-by-side arrangement of these comblike structures gives rise to the crystalline part and the amorphous part consists of randomly oriented P3AT chains. These polymer systems also display a polymorphic character, Phase-I and Phase-II [30]. Phase-I has a longer separation distance between backbones than Phase-II, and is more commonly found. Phase-II is characterized by interdigitation among the alkyl chains, whereas in Phase-I an end-to-end arrangement between alkyl chains is prevalent. These two types of morphologies are shown schematically in Fig. 2.4. The crystal structure is seen to be modified due to doping [31, 32]. The separation between consecutive polythiophene backbones along the alkyl chain direction increases and the separation between adjacent conjugation planes decreases due to doping. The extent to which these variations take place are found to depend on the alkyl chain length and the size of the dopant ion.

The alkylthiophene monomers are coupled to each other via their 2 or 5 positions [33].

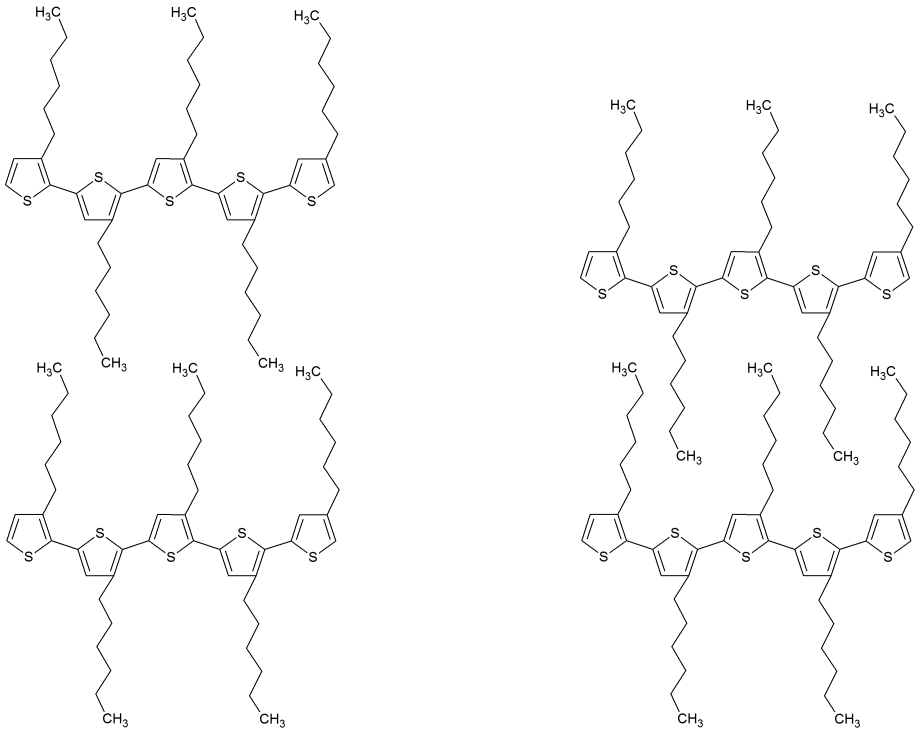

(a) Phase-I (b) Phase-II

Figure 2.4: The two types of morphologies of P3AT polymers.

The possible couplings are shown in Fig. 2.5—a head-to-tail-head-to-tail coupling (HT-HT) is one where the 2 position of one monomer is attached to the 5 position of the next monomer, i.e., a 2,5-2,5 coupling. Similarly, a tail-to-tail-head-to-tail coupling (TT-HT) is a 5,5-2,5 coupling, a head-to-tail-head-to-head coupling (HT-HH) is a 2,5-2,2 coupling and a tail-to-tail-head-to-head coupling (TT-HH) is a 5,5-2,2 coupling. Usual synthetic methods for preparing P3AT polymers result in random attachments at the 2,5 positions and such polymers are called *regiorandom*. A *regioregular* system is one in which majority of the couplings are of one particular type. Usually the HT-HT coupling is preferred as it is conducive to electrical, optical and magnetic performances of the polymers.

The evolution of structural order of P3AT molecules and their orientation on a substrate

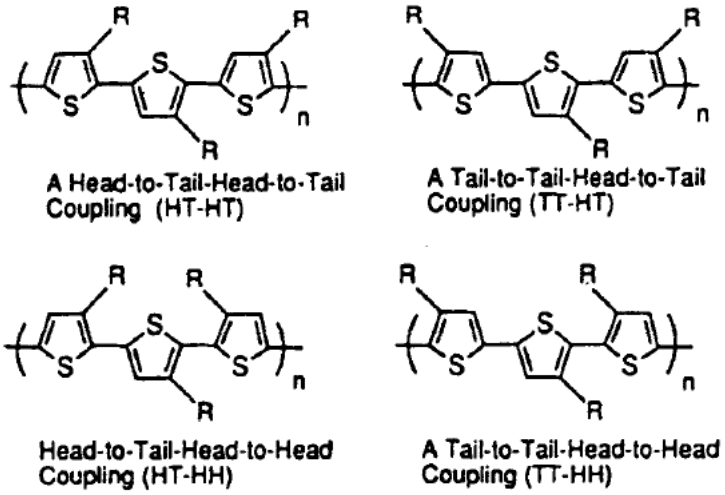

Figure 2.5: The possible coupling types of P3AT [24].

due to thermal treatments has been a topic of extensive research for several years [30, 34–37]. It has been observed that P3ATs with shorter alkyl side chains have higher melting temperatures than those with longer side chains since shorter alkyl chains makes the polymer less flexible. In addition to Phase-I and Phase-II, nematic mesophases, characterized by twisting of the polythiophene backbone, have also been discovered in P3ATs due to temperature changes. In case of P3ATs with longer alkyl chains like poly(3-dodecylthiophene) or P3DDT, this phase cannot be differentiated from Phase-I by XRD as the flexible side chains counteract the effect of twisting and tilting of the polythiophene backbones and preserve the Bragg reflections.

The orientation of P3AT crystallites on a substrate plays a pivotal role in determining the charge transport properties of P3AT-based devices [23, 38]. As in other conjugated polymers, two types of orientations are possible, *edge-on* and *face-on* (Fig. 2.6). Several methods exist for orienting the crystallites according to our specific needs. These include orientation by shear forces like mechanical rubbing, friction transfer, strain alignment and

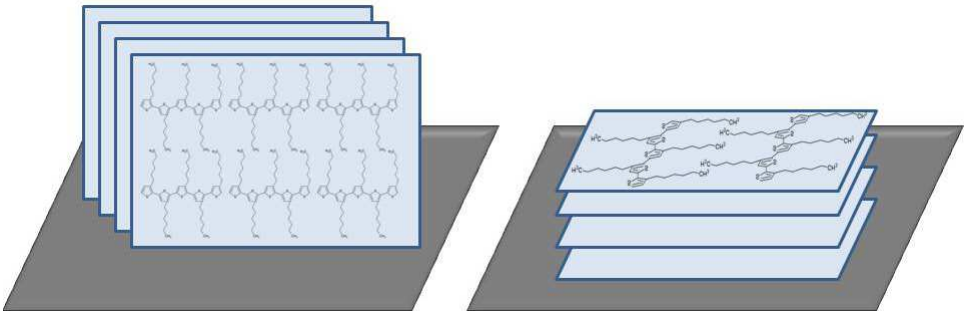

Figure 2.6: The possible orientations of P3AT on a substrate—the figure on the left shows *edge-on* orientaion and the one on the right shows *face-on* orientation.

flow coating, epitaxial growth on an inorganic crystal, an aromatic crystal, or a semicrystalline polymer substrate, directional epitaxial crystallization, etc. Ref. [39] gives a detailed account of these processes. Substrate surface modifications are also known to influence the orientation of the P3AT lamellae. Porzio *et al.* showed that on a functionalized Si substrate the P3AT layers near the substrate exhibit a greater degree of order and orientation than layers near the top while on bare Si the layers are more randomly oriented, especially near the buried interface [40]. Furthermore, the orientation on a substrate can be changed from edge-on to face-on by varying the self-assembled monolayer used to functionalize the substrate [41]. Salammal *et al.* have shown that for spin-coated thin films the proportion of face-on oriented crystallites in a P3AT film increases with the length of the alkyl side chain and that for a particular polymer the proportion increases with increasing annealing temperature [28]. For monolayer-thick films on highly oriented pyrolytic graphite (HOPG), it has been directly evidenced by scanning tunneling microscopy (STM) imaging, that P3AT molecules adopt an edge-on orientation with chain foldings, typical of semicrystalline polymers [42]. Interdigitation was also clearly seen in case of P3ATs with longer alkyl chains.

2.3.2 Structure-property correlation in P3AT films: A short review

There has been a huge amount of research on P3AT-based devices, their structure-property correlation and how to optimize their performance. Here we only attempt to present to the reader a very brief account of the applications of P3AT films in organic electronic devices. P3ATs, especially *poly(3-hexylthiophene)* or P3HT, have emerged as potential candidates for applications in thin film transistors and organic solar cells due to their easy processability, high charge carrier mobilty and environmental stability [3, 23, 27]. Their high conjugation length endows them with high charge carrier mobility, whereas the flexible long alkyl side chains attached to their stiff backbones makes them easily soluble in common organic solvents [43, 44], which is why they are suitable for the fabrication of photovoltaic devices using simple solution processing techniques [45]. The charge carrier mobility of P3AT-based devices strongly depends on the orientation and order of the polymer film in the active layer. The orientation and order of P3AT molecules on a substrate can be influenced by various factors such as regioregularity and molecular weight [23, 46], length of alkyl side chain [30, 47], the solvent from which the film is cast [48], nature of the substrate [49] and deposition techniques like drop-casting, spin-coating, dip-coating and directional epitaxial crystallization [11, 50–52]. Mobility increases with increasing molecular weight of the polymer as longer chains provide longer paths for the charge carriers to travel without hopping to another chain [46]. When several polymer chains are locally aligned they have a strong wave function overlap which leads to the π-stacking. This π-stacking causes the charge carriers and excitons in P3AT to delocalize over several neighboring chains [53, 54]. Improving the π-stacking is thus an important issue in preparing efficient devices using P3ATs. The dependence of crystalline structure on the length of the alkyl side chain has been studied by Causin *et al.* for poly(3-butylthiophene) (P3BT), poly(3-octylthiophene)

(P3OT) and poly(3-dodecylthiophene) (P3DDT) [30]. Polymorphism has been found to be present in case of P3BT and P3DDT but not in case of P3OT, probably because the intermediate length of the octyl group is the optimum length for producing purely Phase-I morphology. A nematic mesophase also exists in P3BT and P3DDT, which is differentiable from Phase-I from X-ray diffraction results in case of P3BT but not in P3DDT as its long side chains counteract the effect of twisting and tilting of the thiophene rings. Chang *et al.* showed that spin-coating from a high boiling point solvent, in which P3ATs have good solubility, promotes the growth of better crystalline films than low boiling point solvents. This improvement in crystallinity is seen to result in a considerable increase in mobility [48]. Post-deposition treatments such as annealing has also been reported to influence the orientation of the crystalline domains [36]. The effect of substrate surface on the morphology of P3AT films has been investigated by numerous groups. It is found that P3HT is adsorbed readily on SiO_2 substrate in an edge-on fashion and the adsorption is much higher if the SiO_2 surface is modified with a perfluorohexyl monolayer [55]. On the other hand, on a HOPG substrate no edge-on orientation is seen and P3HT adopts a face-on orientation. Face-on oriented crystallites have also been found on a substrate modified with an octyltrichlorosilane (OTS) self-assembled monolayer (SAM) [56]. By changing the SAM it is possible to change the orientation of P3AT crystallites from face-on to edge-on [41]. Another factor that affects the stability of these films is the ambient atmosphere. P3AT films are extremely stable under humidity and atmospheric oxygen but are affected to a much greater extent by volatile organic solvents [57, 58].

The applicability of P3AT films in organic electronic devices has been well documented [3, 23, 46, 59–61]. Regiorandom P3HT films spin-coated from chloroform solution onto gold source and drain electrodes have been found to have mobilities between 10^{-5} and 10^{-4} $cm^2V^{-1}s^{-1}$ [62]. Field-effect mobility decreases with increasing alkyl

chain length [63]. The field-effect mobility is strongly enhanced if regioregular P3HT with greater than 98.5% HT-linkages is drop-cast from a chloroform solution. The mobility of such a field-effect transistor can be as high as 0.045 $cm^2V^{-1}s^{-1}$ [64]. On the other hand, P3HT with lower regioregularity (81% HT-linkages) give rise to much lower mobilities, about 2×10^{-4} $cm^2V^{-1}s^{-1}$. This variation is attributed to the different orientations adopted by P3HT with different regioregularities. Various kinds of post-deposition treatments have been devised to increase the mobility and on-off ratio of P3AT-based FETs. For example, treating P3HT drop-cast films with ammonia results in an increase in on-off ratio by more than an order of magnitude [65], whereas immersing the film in hydrazine increases the ratio by four orders of magnitude. In addition to spin-coating and drop-casting, horizontal deposition on a hydrophobic substrate by Langmuir-Schaeffer method has also been used to prepare P3HT films [66]. Such films displayed an edge-on orientation of the polymer and mobilities ranged between 3×10^{-3} and 2×10^{-2} $cm^2V^{-1}s^{-1}$ for multilayer films and lower for monolayer films. P3AT nanofibers also find extensive use in OFETs [67]. Lee and co-workers have reported that FETs using P3HT nanofibers prepared by electrospinning can give rise to a mobility of 0.017 $cm^2V^{-1}s^{-1}$ and an on-off ratio of 100 [68]. Shimomura *et al.* have shown that field-effect mobilities of P3HT nanofibers prepared by mixed solvents method varies between 3.8×10^{-2} and 5.6×10^{-2} $cm^2V^{-1}s^{-1}$ depending on the ratio of good and poor solvents [69]. P3HT is also one of the most widely used materials in organic photovoltaic cells. Composites of P3HT and 1-(3-methoxycarbonyl)propyl-1-phenyl[6,6]C_{61} (PCBM) find abundant use as active materials in bulk heterojunctions [70, 71] and power conversion efficiency of upto 5% have been reported.

From the above discussion the importance of P3ATs is obvious. Suffice it to say here that they are among of the most promising materials for modern day electronic applica-

tions. It is this expanding interest in this class of materials that prompts us to study their structural behaviour under various circumstances, as their properties are directly related to their structures.

2.3.3 Poly(3-dodecylthiophene)

The most widely studied member of the P3AT family is, perhaps, P3HT, which owes its popularity to its optimal alkyl chain length (6 carbon atoms). P3HT-based devices are shown to give rise to higher field-effect mobilities than devices based on P3ATs with longer or shorter alkyl chains. However, P3ATs with longer alkyl side chains, such as *poly(3-dodecylthiophene)* (P3DDT) is found to give rise to stronger photoluminescence [72] and electroluminescence [59] intensities than P3ATs with shorter alkyl chains. Even then, P3DDT is less studied due to its lower crystallizability arising from longer side chain interactions [47, 61, 73–76]. However, the longer alkyl chains of P3DDT are responsible for its better solubility, which is conducive for preparing films with better continuity and smoothness, useful for device applications. So understanding the effects of several processing parameters on the crystalline structure of P3DDT films and efforts to increase its crystallinity are undeniably of immense importance in order to make it useful in organic electronics.

2.4 The future of conducting polymer thin films

The future of organic electronics is bright and conducting polymer thin films are expected to play a very important role in its development. It is not only because polymer thin film devices are flexible and offer appreciable charge carrier properties, but also because they are biologically compatible which can make them potential candidates for use in bio-electronic

sensors [77]. Moreover, these systems are more eco-friendly and are expected to be more energy-efficient than inorganic devices in the future. However, in order to achieve these goals, the difficulties related to defects and disorder in polymer films, understanding the behaviour of polymer-substrate interfaces, etc. need to be addressed and controlled. Only then can we hope to exploit the full power of conducting polymers and use them in multifarious applications like light-emitting diodes, light-emitting electrochemical cells, photovoltaic cells, photodetectors, field-effect transistors and sensors.

CHAPTER 3

EXPERIMENTAL TECHNIQUES

In this chapter we will discuss the various processes used for preparing the polymer films and the techniques and instruments used to characterize them.

3.1 Sample preparation

Sample preparation consists of two steps, (i) modification of the substrate surface and (ii) deposition of the polymer on the substrate to form a film.

3.1.1 Substrate surface modification

Different types of substrates were used in the present work and their methods of preparation are discussed below.

3.1.1.1 Native oxide-coated silicon

Silicon (Si) wafers, both (001) and (111) oriented ones, were cut into pieces of desired dimensions and were fist cleaned by sonication in acetone and ethanol for 10 minutes each. This helps in removing any organic contaminant on the substrates and the substrates are covered with a native oxide layer. These substrates are termed O-Si.

3.1.1.2 H-passivated silicon

For preparing *weakly hydrophobic* substrates the sonicated Si wafers were etched with hydrogen fluoride by immersing the substrates in HF [Merck, 10%] solution for 60 s at room temperature (25°C) to terminate the Si surface with H after removing the native oxide layer [78–82]. These substrates are termed H-Si.

3.1.1.3 Freshly prepared oxide-coated silicon

For preparing *weakly hydrophilic* substrates the sonicated Si wafers were subjected to RCA treatment [83]. The substrates were heated in a solution containing ammonium hydroxide (NH_4OH, Merck, 30%), hydrogen peroxide (H_2O_2, Merck, 30%) and Milli-Q water taken in the ratio 1:1:5 by volume for about 10 minutes. The substrates thus prepared have a layer of freshly prepared oxide on them and are termed OH-Si.

3.1.1.4 Quartz glass

For optical spectroscopy studies quartz glass substrates were used after cleaning them by sonication in acetone and ethanol for 10 minutes each.

3.1.2 Film deposition

Polymer films were deposited in two ways, (i) spin-coating and (ii) drop-casting. These two methods are described in the following sections.

3.1.2.1 Spin-coating

Basic principles

Spin-coating is a widely used technique for preparing uniform thin films on substrates. It is used for preparing films of thickness ranging from a few nm to a few μm. Spin-coating process involves the following steps (Fig. 3.1) — first, a drop of the solution containing the material to be deposited is applied on the substrate and then the substrate is accelerated to a high rotational speed so that most of the solution is flung off immediately. Next, the film thins gradually as the remaining solution flows radially outward due to centrifugal force and simultaneously the solvent evaporates, increasing the viscosity of the solution and thus decreasing the radial flow. The remaining solution dries at a rate depending on the air-flow, the viscosity and volatility of the solvent, the concentration of the solution, etc., leaving a uniform film of the desired material on the surface.

The process of spin-coating is a complex one involving several mechanisms like fluid inertia, Coriolis forces, surface tension, solution concentration, volatility of the solvent, etc. which can also vary with time. In addition, the solute molecules may interact with the solvent giving rise to non-Newtonian nature of the fluid [84]. Emslie *et al.* [85] performed the earliest modeling of the process considering a Newtonian fluid. Later on, Acrivos *et al.* [86] and Jenekhe *et al.* [87] modified the above model considering non-Newtonian effects. That the evaporation of the solvent is an important controlling parameter in the process was first suggested by Meyerhofer [88]. The spin-coating speed (ω) is also a very

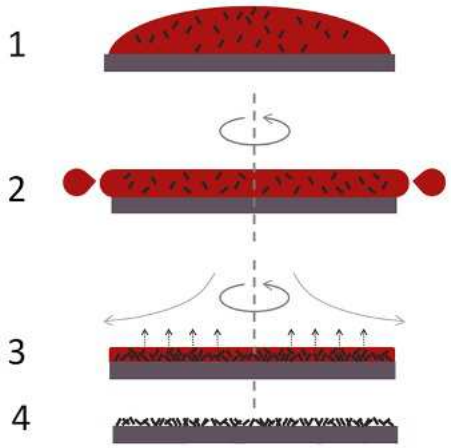

Figure 3.1: Schematic diagram showing the steps involved in the process of spin-coating.

important parameter affecting the thickness (D) of the deposited film which is related to ω as

$$D \sim \frac{1}{\sqrt{\omega}}.$$

In fact, the film thickness has a well-known empirical relationship with different internal physical parameters (such as viscosity of solution and evaporation-rate, etc. of solvent) and external parameter (such as spinning speed) as [89]

$$D \approx K_0 \omega^{-0.50} (E\lambda/C_p)^{0.60} \eta^{0.36}, \tag{3.1}$$

where ω is the rotational speed, K_0 is a constant for volatile organic solvents, which is related to the other external conditions such as temperature, relative humidity, air velocity,

Figure 3.2: Spin coater SCS 6800.

etc., E, λ and C_p are the evaporation rate, latent heat of evaporation and heat capacity of the solvent, respectively, and η is the viscosity of the solution.

Instrument

The spin-coater used in our experiments was SCS 6800 Spin-coater series, shown in Fig. 3.2. It has a coating chamber mounted on a stage and enclose a vacuum chuck for holding the substrate. The chuck can be rotated with the help of a high speed motor attached below the horizontal stage and the maximum rotating speed is around 10,000 rpm. A rotary vacuum pump is used for sucking the air between the chuck and the substrate and thus hold the substrate firmly during spinning. A control unit with a display panel is attached to the spin-coating unit for adjusting the speed, acceleration and duration of spinning.

3.1.2.2 Drop-casting

Spin-coating produces films with high uniformity but usually with low degree of order. Since it involves rapid evaporation of the solvent, the molecules of the dissolved material do not have enough time to self-assemble into ordered structures. Drop-casting, on the other hand, produces films with a high degree of ordering at the cost of decreased uniformity.

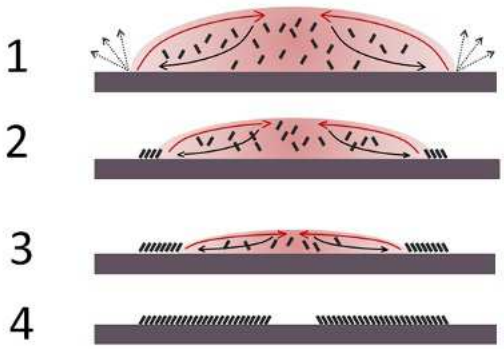

Figure 3.3: Schematic diagram showing the steps involved in drop-casting.

This method involves putting a drop of the solution containing the desired material on a substrate and allowing the drop to dry on its own, leaving a film on the substrate. As the solvent evaporates, the drop shrinks in size, depositing the molecules at the receding edges (Fig. 3.3). This being a slow drying process, it gives the dissolved molecules ample time to organize themselves into well ordered structures. Even better ordering can be achieved by slowing down the evaporation time, e.g., by keeping the substrate with the drop inside a covered arrangement.

3.2 Characterization tools

Characterization of the samples prepared was done primarily using different X-ray scattering techniques. Additionally, other techniques like scanning probe microscopy, optical absorption spectroscopy and dynamic light scattering were employed to provide us with a

complete description of the samples. In the following sections these techniques are discussed in detail.

3.2.1 X-ray scattering

Since its discovery by W.C. Röntgen in 1895, X-rays have played a pivotal role in the determination of the structure of materials. Tremendous progress, both in the theoretical understanding of its interaction with matter as well as in the technical know-how needed to exploit them experimentally, has enabled X-ray scattering to be used in a variety of problems ranging from the determination of the structures of simple compounds to that of DNA, proteins, etc.

X-rays are electromagnetic waves having wavelength of the order of an Angström, i.e, 10^{-10} m. The relation between its wavelength λ in Å and photon energy E in keV is given by

$$\lambda = \frac{hc}{E}. \tag{3.2}$$

An X-ray photon impinging on a material can interact with it in two ways— it can either be scattered or be absorbed [90,91]. We are mainly interested in the scattering of X-rays by matter. X-ray scattering provides a host of non-destructive techniques to probe the internal structure of materials, both in bulk and in thin films. These include X-ray Diffraction (XRD), X-ray Reflectivity (XR), Grazing Incidence Diffraction (GID), Grazing Incidence Small Angle X-ray Scattering (GISAXS), diffuse scattering, etc. In this work we have used a combination of these techniques to analyze our samples.

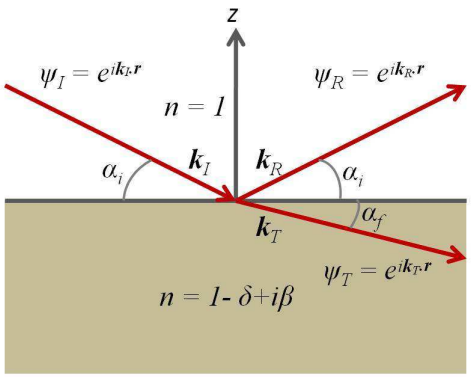

Figure 3.4: Reflection and transmission of X-rays from an interface.

3.2.1.1 Basic theory

The refractive index *n* of electromagnetic waves displays resonant behaviour near the frequencies corresponding to electronic transitions in atoms and molecules. *Normal dispersion* occurs on the low frequency side of a resonance, where refractive index *n* increases with frequency ω. On the high frequency side *n* decreases with ω and this is known as *anomalous dispersion*. Since the frequency of X-rays is higher than most transition frequencies, in this region *n* turns out to be less than unity. This indicates a phase shift of π in the Thomson scattering of X-rays and results in *total external reflection* of X-rays from a flat, sharp interface, i.e., for incident angles α less than a critical angle α_c the incident X-ray beam does not penetrate the sample, but is totally reflected from it.

The refractive index *n*, of a homogeneous medium, for X-rays is given by

$$n = 1 - \delta + i\beta, \tag{3.3}$$

where

$$\delta = \frac{2\pi\rho r_0}{k^2} \tag{3.4}$$

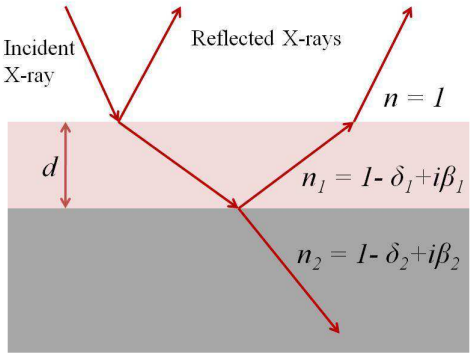

Figure 3.5: Reflection and transmission of X-rays from a slab of finite thickness.

and

$$\beta = \frac{\mu}{2k}. \tag{3.5}$$

Here ρ is the electron density of the material, k is the wave-vector and is related to the wavelength of radiation λ by $k = \dfrac{2\pi}{\lambda}$, r_0 is the classical electron radius whose value is 2.82×10^{-5} Å and μ is the absorption coefficient of the medium. According to Snell's law the glancing angles α_i and α_f are related by

$$\cos\alpha_i = n\cos\alpha_f. \tag{3.6}$$

The critical angle α_c is obtained by setting α_f = 0 and is given by

$$\alpha_c = \sqrt{2\delta} = \frac{\sqrt{4\pi\rho r_0}}{k}. \tag{3.7}$$

Using typical values it can be inferred that α_c is of the order of one milli-radian.

3.2.1.2 X-ray Reflectivity

X-ray Reflectivity (XR) has emerged as a very important surface-sensitive technique for analyzing the thickness, roughness and electron density of smooth films and multilayers on substrates [92]. It consists in reflecting a beam of X-rays from a smooth interface and measuring the intensity in the specular direction, i.e, in a direction such that the reflected angle is equal to the incident angle. The basic expressions for specular reflection and transmission at a smooth interface can be derived from Maxwell's equations for electromagnetic waves, considering boundary conditions for continuity of the electric and magnetic fields and their derivatives at the interface [93]. These are known as Fresnel's equations for the *amplitude* reflectivity (r) and transmittivity (t) and are given by

$$r \equiv \frac{a_R}{a_I} = \frac{\alpha_i - \alpha_f}{\alpha_i + \alpha_f}, \tag{3.8}$$

$$t \equiv \frac{a_T}{a_I} = \frac{2\alpha_i}{\alpha_i + \alpha_f}. \tag{3.9}$$

The *intensity* reflectivity and transmittivity, denoted by R and T, respectively, are obtained from the absolute squares of r and t. Since α_i and α_f are small, by expanding the cosines in Snell's law we obtain

$$\alpha_i^2 = \alpha_f^2 + \alpha_c^2 - 2i\beta. \tag{3.10}$$

From the above equation we find that α_f is a complex number and can be written as

$$\alpha_f \equiv \mathbb{R}(\alpha_f) + i\mathbb{I}(\alpha_f). \tag{3.11}$$

Thus, the transmitted wave falls off with increasing depth into the medium and its intensity falls with a 1/e penetration depth Λ as

$$\Lambda = \frac{1}{2k\mathbb{I}(\alpha_f)}. \tag{3.12}$$

Converting angular variables to wave vector transfers

$$Q \equiv 2k \sin\alpha \approxeq 2k\alpha, \tag{3.13}$$

$$Q_c \equiv 2k \sin\alpha_c \approxeq 2k\alpha_c, \tag{3.14}$$

and their dimensionless counterparts

$$q_i \equiv \frac{Q_i}{Q_c} \approxeq \frac{2k}{Q_c}\alpha_i, \tag{3.15}$$

$$q_f \equiv \frac{Q_f}{Q_c} \approxeq \frac{2k}{Q_c}\alpha_f, \tag{3.16}$$

we obtain

$$r(q) = \frac{q_i - q_f}{q_i + q_f}, \tag{3.17}$$

$$t(q) = \frac{2q_i}{q_i + q_f}, \tag{3.18}$$

$$\Lambda(q) = \frac{1}{Q_c\mathbb{I}(q_f)} \tag{3.19}$$

When the wave vector transfer is very large in comparison to q_c, i.e, $q \gtrsim 3q_c$, R displays an asymptotic behaviour,

$$R = \frac{q_c^4}{16q^4}. \tag{3.20}$$

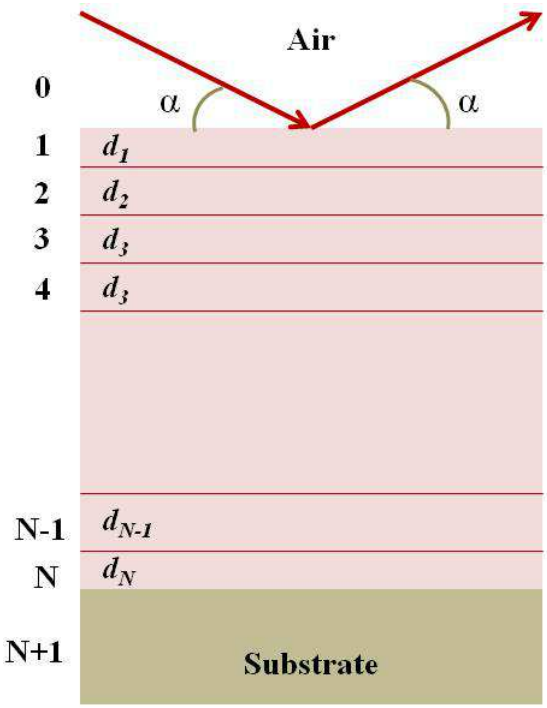

Figure 3.6: Schematic of reflection of X-rays from a multilayer stack.

Reflectivity of a film: The reflectivity and transmittivity of a film is derived by considering reflection and transmission from a thin slab of thickness d. The situation is depicted in Fig.3.5. In this case there is an infinite number of possible reflections from the two interfaces. Using Fresnel's equations at the two interfaces, we obtain the total amplitude reflectivity as

$$r_{slab} = \frac{r_{01} + r_{12}p^2}{1 + r_{01}r_{12}p^2}, \tag{3.21}$$

where r_{ij} is the amplitude reflectivity for X-rays incident from the i-th onto the j-th medium, p^2 is the phase factor of the rays reflected from the top and bottom faces of the slab and is given by $\exp[iQ_1d]$, and $Q_1 = 2k\sin\alpha_1$. The reflectivity thus obtained displays oscillations due to interference of waves reflected from the top and bottom interfaces. These are known as *Kiessig fringes* and occur with a period of $\frac{2\pi}{d}$ in Q [94].

Reflectivity of a multilayer system: The above treatment can be extended to calculate the reflectivity of a multilayer system, i.e, a system consisting of N layers where the n-th layer has thickness d_n (Fig.3.6). We thus arrive at a recursive formula [95],

$$r_{n-1,n} = \frac{r_{n,n+1} + F_{n-1,n}}{1 + r_{n,n+1}F_{n-1,n}} \exp[iq_n d_n], \tag{3.22}$$

where

$$F_{n-1,n} = \frac{q_{n-1} - q_n}{q_{n-1} + q_n}. \tag{3.23}$$

The reflectivity of this system is obtained by solving the above equation 3.22 under the assumption that $r_{N,N+1} = 0$, as the $(N + 1)$-th layer is the substrate whose thickness is usually taken to be infinite. The thickness of the 0-th layer (air) is also infinite.

Reflectivity considering roughness: Until now we have considered only smooth surfaces with sharp interfaces. However, real surfaces and interfaces are hardly ever perfectly smooth. Instead, the height of an interface has a certain degree of randomness, which we call the *roughness* of the interface. A rough interface is described by a statistical distribution and the heights of different points on it are correlated in a way characteristic of the type of roughness [96, 97]. Consequently, the reflectivity is no longer strictly specular, but has a *diffuse* or *off-specular* component. Reflectivity of a rough interface is less than that of a smooth interface and this deviation increases as we go to higher values of q [98]. The effect of roughness can be estimated by decomposing the scattering density profile into a series of layers as described above and using the iterative scheme. Generally, the first derivative of the scattering density profile can be described as a Gaussian function, as a result of which

the reflectance of a rough interface can be written, using Born approximation, as

$$r_{n-1,n} = r^F_{n-1,n} \exp\left[-\frac{1}{2} q_{n-1} q_n \sigma_n^2\right], \tag{3.24}$$

where σ_n gives us a measure of roughness between the $(n-1)$-th and n-th layers and r^F is the reflectance from a smooth interface. The above equation can be simplified to get the reflectivity in case of an interface separating two media 1 and 2 as

$$R_{rough} = R_F \exp[-q^2 \sigma_{12}^2], \tag{3.25}$$

where R_F is the Fresnel reflectivity and σ_{12} is the roughness of the interface separating media 1 and 2. σ_{12} is given by $\sqrt{\langle h^2 \rangle}$, where $2\langle h^2 \rangle$ is the ensemble average of height differences and is given as follows,

$$\langle [h(0,0) - h(x,y)]^2 \rangle = 2\langle h^2 \rangle. \tag{3.26}$$

In general, the roughness of the film-air interface results in a faster fall in the reflectivity curve, while roughness of the film-substrate interface decreases the amplitude of multilayer peaks.

Resolution function: So far we have considered an X-ray beam which is strictly monochromatic, has no angular divergence and a detector that is perfectly point-like. But in a real life experiment the conditions obviously deviate from these assumptions and in that case we have to convolute the data obtained with a *resolution function* for proper analysis. The resolution depends primarily on the wavelength dispersion ($\Delta\lambda/\lambda$), the angular divergence of the incoming beam ($\Delta\alpha_i$) and the acceptance of the outgoing beam ($\Delta\alpha_r$). In the usual geometry of XR experiments, the aperture of the detector slits perpendicular

to the scattering plane is kept wide open so that the scattered intensity in the q_y direction is integrated out. The wave-vector transfer q can be resolved into components in the x-z co-ordinate system as

$$q_x = k(\cos\alpha_r - \cos\alpha_i), \tag{3.27}$$

$$q_z = k(\sin\alpha_i + \sin\alpha_r). \tag{3.28}$$

Differentiating the above equations with respect to α_i and α_r, we get

$$dq_x = k(\sin\alpha_i d\alpha_i - \sin\alpha_r d\alpha_r) - dk(\cos\alpha_i - \cos\alpha_r), \tag{3.29}$$

$$dq_z = k(\cos\alpha_i d\alpha_i - \cos\alpha_r d\alpha_r) + dk(\sin\alpha_i + \sin\alpha_r), \tag{3.30}$$

where $dk = -d\lambda/\lambda$. With the assumption that $d\alpha_i$ and $d\alpha_r$ are randomly distributed, the resolution widths in q_x and q_z are given by

$$\Delta q_x^2 = k^2(\sin^2\alpha_i\Delta\alpha_i^2 + \sin^2\alpha_r\Delta\alpha_r^2) + \Delta k^2(\cos\alpha_i - \cos\alpha_r)^2, \tag{3.31}$$

$$\Delta q_z^2 = k^2(\cos^2\alpha_i\Delta\alpha_i^2 + \cos^2\alpha_r\Delta\alpha_r^2) + \Delta k^2(\sin\alpha_i + \sin\alpha_r)^2. \tag{3.32}$$

In the specular condition $\alpha_i = \alpha_r = \alpha$ and neglecting the effect of wavelength dispersion when compared to the angular spread, the resolution widths are given by

$$\Delta q_x = k\sin\alpha[\Delta\alpha_i^2 + \Delta\alpha_r^2]^{1/2}, \tag{3.33}$$

$$\Delta q_z = k\cos\alpha[\Delta\alpha_i^2 + \Delta\alpha_r^2]^{1/2}. \tag{3.34}$$

Defining $[\Delta\alpha_i^2 + \Delta\alpha_r^2]^{1/2}$ as the half width at half maxima (HWHM), σ_d, of the direct

beam, we have

$$\Delta q_x = q_z \sigma_d / 2, \tag{3.35}$$

$$\Delta q_z = k \sigma_d \cos \alpha. \tag{3.36}$$

3.2.1.3 Grazing Incidence Small Angle X-ray Scattering

Grazing Incidence Small Angle X-ray Scattering or GISAXS [99] has developed as an enormously powerful technique for the characterization of the morphology of nanoparticles and their clusters in the last couple of decades. It is a non-destructive reciprocal space technique which allows investigation of nanoobjects, either on a surface or embedded in a matrix, with size ranging from a nanometer to a few microns. The small interaction of hard X-rays with matter was a hurdle in the path of using it for surface or interface studies. However, with the advent of high brilliance synchrotron radiation coupled with grazing incidence geometry, X-rays could be used for probing surfaces with appreciable signal-to noise ratio [100]. GISAXS is a subset of Grazing Incidence X-ray Scattering or Diffraction (GIXS or GIXD) [101, 102] techniques, which has several advantages [103], e.g, the technique is fully non-destructive, it gives a statistical average information of the entire sample surface in contrast to microscopy, it has the ability to probe the surface as well as buried interfaces and bulk by a mere change in the incident angle, it can be used in a variety of sample environments and also for *in-situ* measurements. GIXS techniques have been employed in widely differing situations like granular multilayer systems [104], implanted systems [105], semiconductor quantum dots [106, 107], cluster formation of metal nanoparticles [108], semicrystalline polymers [28, 109], studies of dewetting of polymer films [110] and swelling of block copolymer films [111].

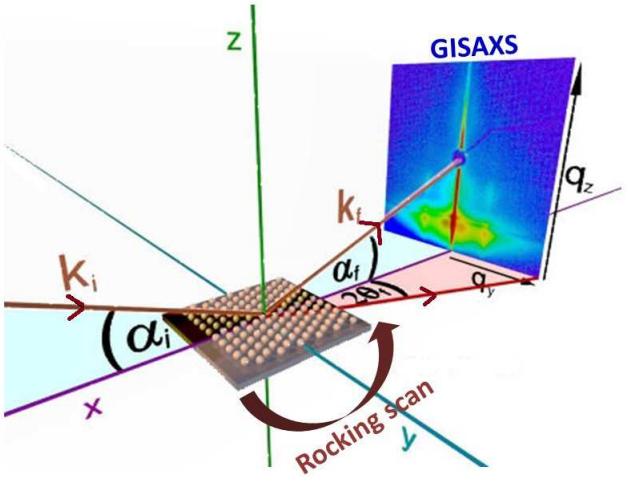

Figure 3.7: The scattering geometry of a GISAXS experiment.

The scattering geometry: The scattering geometry of a GISAXS experiment is shown in Fig. 3.7. The incident beam, of wave vector $\mathbf{k}_i$, is kept at grazing angle to the sample, i.e the incident angle α_i is small and kept constant, usually at a value close to the critical angle α_c. The scattered beam, of wave vector $\mathbf{k}_f$, makes an angle α_f with the sample surface and an in-plane angle $2\theta_f$ with the direction of the transmitted beam. The wave vector transfer $\mathbf{q} = \mathbf{k}_f - \mathbf{k}_i$ is decomposed into two components, $\mathbf{q}_{||}$ and $\mathbf{q}_\perp$, which are, respectively, parallel to and perpendicular to the substrate. The absolute value of $\mathbf{q}_\perp$ is q_z and is related to α_i and α_f as

$$|\mathbf{q}_\perp| = q_z = k_0[\sin\alpha_f + \sin\alpha_i], \tag{3.37}$$

where $k_0 = |\mathbf{k}_f| = |\mathbf{k}_i| = \dfrac{2\pi}{\lambda}$ represents the elastically conserved wave vector modulus. The relation between the angular coordinates and the wave vector transfer coordinates, for

GIXS techniques, can be expressed as

$$q_x = k_0[\cos 2\theta_f \cos \alpha_f - \cos \alpha_i], \tag{3.38}$$

$$q_y = k_0[\sin 2\theta_f \cos \alpha_f], \tag{3.39}$$

$$q_z = k_0[\sin \alpha_f + \sin \alpha_i]. \tag{3.40}$$

GISAXS is used to probe the morphology both parallel to (along q_y) and perpendicular to (along q_z) the sample surface at length scales typically ranging from a few nm to a few hundred nm. On the other hand, GIWAXS or Grazing Incidence Wide Angle X-ray Scattering is used to probe order at the atomic scale. For GISAXS all angles are assumed to be small (less than a few degrees). In that case

$$q_x \simeq 0, \tag{3.41}$$

$$q_y \simeq k_0 \sin 2\theta_f \simeq k_0 2\theta_f, \tag{3.42}$$

$$q_z \simeq k_0 \alpha_f, \tag{3.43}$$

i.e., the reciprocal space scales with the angular coordinates. In a typical GISAXS measurement beam-stops are used to block the direct beam and the specularly reflected beam from hitting the 2-D detector. Due to refraction and reflection effects the Yoneda peak, which is the maximum of the off-specular diffuse scattering intensity, is located at the critical angle for total external reflection, i.e, at α_c.

3.2.1.4 Lab source X-ray scattering facility

The lab source X-ray scattering facility used in our experiments is the Versatile X-ray Diffractometer (VXRD) from Bruker AXS, Germany (Fig.3.8) [112]. It has a Cu sealed

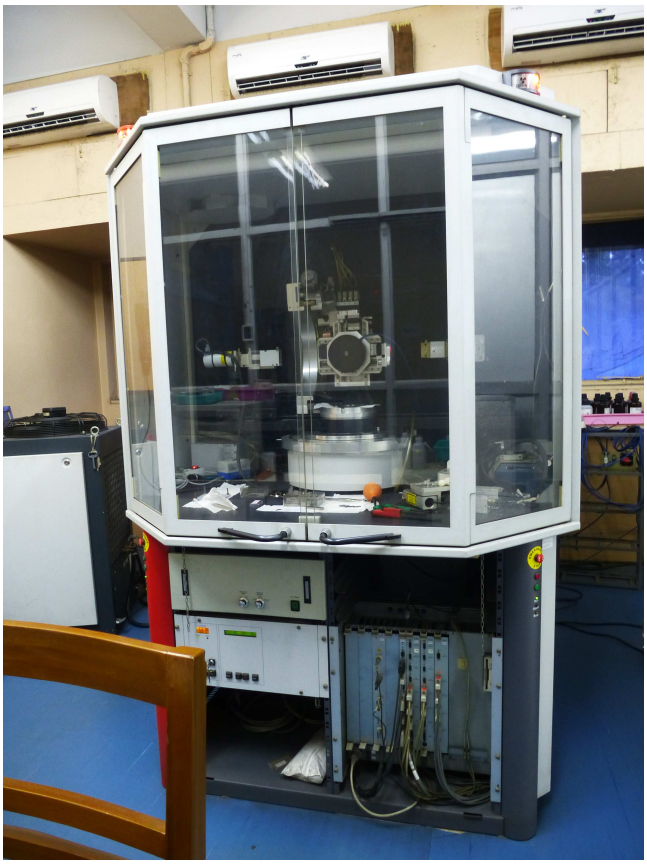

Figure 3.8: Bruker D8 Discover, the Versatile X-ray Diffractometer used in the experiments.

tube which generates X-rays of the required energy, focal spot and intensity by bombarding the target sample with electrons generated from the cathode. The focal spot (also called focal spot on target) and takeoff angle are critical features in the production of X-rays by sealed tube. The focal spot on the target is the area bombarded by electrons and the takeoff angle is the angle between the primary X-ray beam and the surface. The takeoff angle can be set from 3° to 7°. In this system the normal emission angle is 5°. Normally, sealed tube has 2 to 4 beryllium windows through which X-rays exit. The focal spot is typically rectangular in shape with a length-to-width ratio of 10 to 1. The projection along the length of the focal spot at a takeoff angle from the anode surface is called spot focus. For fine

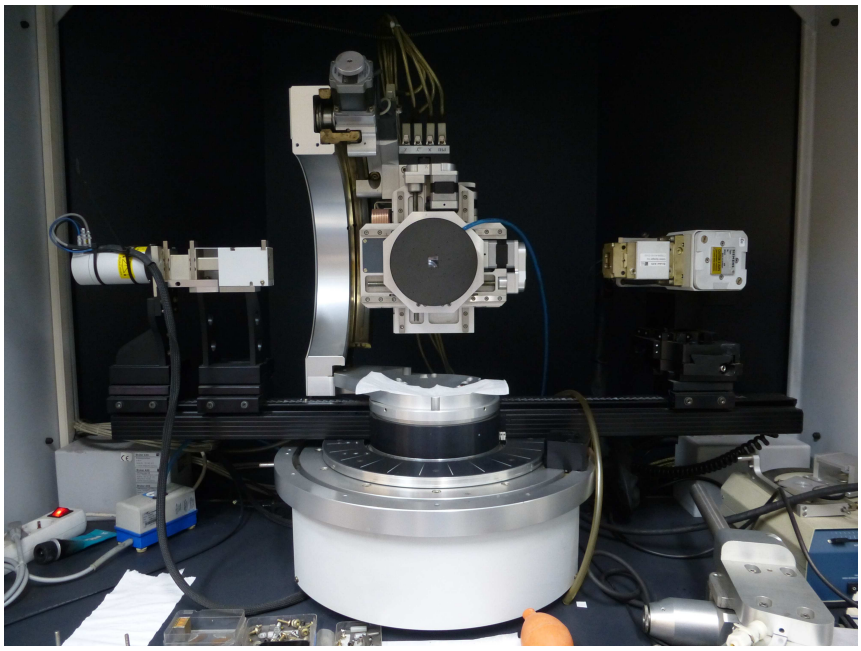

Figure 3.9: Close-up of the sample stage, source and detector of Bruker D8 Discover.

focus the focal spot size at anode is 0.4×8 mm^2 and spot focus size is 0.4×0.8 mm^2. The emerging primary X-rays then pass through the beam optics components consisting of a monochromator, a pinhole collimator and a Göbel mirror. A graphite crystal monochromator is typically used which gives the strongest beam intensity but cannot resolve the $K_{\alpha1}$ and $K_{\alpha2}$ lines. So the monochromator is aligned to K_α line of wavelength λ = 1.54 Å and X-rays of other wavelengths are filtered out. The monochromatized X-ray beam then passes through the Göbel mirror which is a parabolic multilayer mirror. The Göbel mirror is the bent gradient multilayer optics. The standard lengths of the multilayer optics are 40 mm and 60 mm. This mirror is used to convert the divergent beam emitted from the X-ray source into an intense parallel beam. These special diffractive properties are valid for the K_α radiation of the source, so that the mirror is mainly diffracting the K_α part of the spectrum.

In VXRD setup, a high-precision, two-circle goniometer with independent stepper mo-

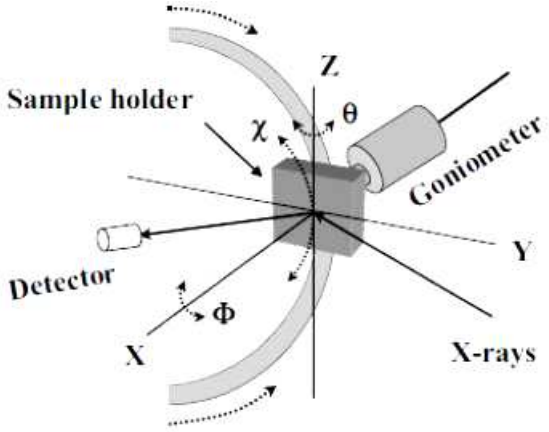

Figure 3.10: Rotation geometry of the θ, ϕ and χ motors in VXRD setup with quarter-circle Eulerian cradle.

tors and optical encoders for θ and 2θ circles is used. The sample stage is usually mounted on the inner θ circle of the goniometer. The goniometer can be used in horizontal θ-2θ, vertical θ-2θ and vertical θ-θ geometries. In θ-2θ mode, the sample rotation is defined as ω rotation and the sample stage directly mounted on the goniometer inner circle is called ω-stage. The used sample stage is a quarter-circle Eulerian cradle having two rotational (χ and ϕ) and three translational (X, Y and Z) motions. The corresponding θ, ϕ and χ motor movements have been shown schematically in Fig.3.10.

The sample stage in the VXRD consists of a 5 inch vacuum chuck connected to a rotary pump in order to hold the sample in place during its movement. The instrument is connected to a cooling water unit (ERL2000 chiller) to maintain the source at a constant temperature. Software controlled stepper motors operate the movement of all the parts of the instrument. The scattered beam is detected using a NaI scintillation (point) detector. The detector interface board generates high voltage required for the operation of scintillation and proportional counters. It contains a high speed pulse amplifier with a pulse shaping stage, line shift correction and baseline restoration unit and also two discriminator

windows including complete pulse counting unit. In addition there is a digital count input for various kinds of detectors having digital pulse output. The VXRD unit is kept in a radiation protection housing as shown in Fig.3.8 . A lead glass window at the front of the radiation protection housing enables the samples to be changed and or the diffractometer mounts to be modified. The window shutter of the X-ray tube stand closes automatically when this window is opened. Two red LEDs glow when the window shutter is open and a green LED glows when the window shutter is closed.

Sample alignment and types of scans: Sample alignment is done in two steps—first the detector angle is set to zero and the sample holder is translated to a position where the detected intensity is half the direct beam intensity. This aligns the sample holder to the direct beam. Next, the sample holder is rocked about its axis (θ-scan at 2θ = 0) to ensure that the sample surface is parallel to the incident beam. If it is correctly aligned then the detected intensity is maximum at θ = 0, as expected. Otherwise the intensity is maximum at an angle away from 0 and in that case the offset angle is to be adjusted in order to achieve the specular condition. The specular condition implies that the incident angle, α is equal to the reflected angle, β ($\alpha = \beta = \theta$). Under such a condition there exists a non-vanishing wave vector component, q_z, which is equal to $(4\pi/\lambda)\sin\theta$ with resolution 0.002 Å^{-1}. The qualitative idea about the samples has been obtained from the Kiessig fringes of the XR profiles. To get a quantitative information i.e., in-plane (x-y) average electron density (ρ) as a function of depth (z) in high resolution, all XR profiles have been analyzed using Parratt's formalism [95] from which one can estimate the total film thickness, the average electron density and the roughness of the film-substrate and film-air interfaces. For this purpose, each film has been divided a into number of bilayers and roughness has been incorporated at each interface. The thickness, electron density, and roughness associated with each layer were then set as fitting parameters. Other than the specular reflectivity scan, another type

of scan that has been very crucial in our studies is the rocking scan or the diffuse scattering scan. This is performed about a specular point by scanning the θ-motor with 2θ-motor fixed. Here the transverse component of wave vector q_x changes continuously and keeps the normal component of wave vector q_z almost unchanged at small angular positions of the motors. Normal XRD scans were also performed to investigate the crystalline order in thicker polymer films.

Footprint correction of reflectivity data: An important correction to be made to specular reflectivity data is the *footprint correction*. This is an instrumental effect arising due to the footprint or size of the beam on the sample. The size of the beam is important because reflectivity data are usually taken from below the critical angle of total external reflection. Considering a rectangular beam of dimensions $t_1 t_2$, where t_2 is the dimension parallel to the sample surface, incident at an angle α, we can show that the footprint of the beam on the sample is

$$F = \frac{t_1}{\sin\alpha} t_2. \tag{3.44}$$

For reflectivity measurements the sample size L (along the incident beam) must be at least equal to F at the critical angle for total reflection to occur. In such a situation the loss of reflectivity below the critical angle (expected to be unity otherwise) can be compensated simply by multiplying the experimental data with F/L [91, 98].

3.2.1.5 Synchrotron source X-ray scattering facilities

The basic principle behind synchrotron radiation was discovered by the German physicist Heinrich Hertz who found that charged particles emit electromagnetic radiation when accelerated. *Synchrotron radiation* (SR) is the radiation emitted by a charged particle moving in a circular path with constant, relativistic speed [113]. However, nowadays the term is

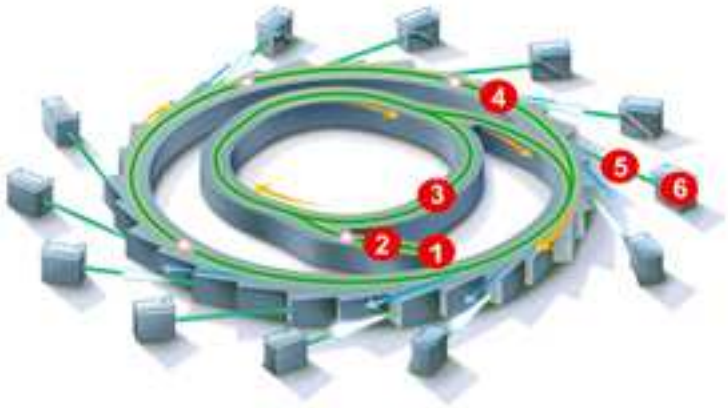

Figure 3.11: Schematic view of a synchrotron radiation source showing (1) the electron gun, (2) the linear accelerator, (3) the booster synchrotron, (4) the storage ring, (5) beamlines, and (6) experiment stations.

used as a generic term to describe radiation from charged particles moving with relativistic speeds along curved trajectories under the influence of a magnetic field. So synchrotron radiation is not only produced in synchrotrons, but also in storage rings where it is generated either by *bending magnets* or by insertion devices such as *wigglers* or *undulators* [90]. The spectrum of synchrotron light spreads from the far infrared up to near gamma rays. The radiation is highly polarized and the intensity much higher than other sources. The figure of merit for an X-ray source is the *brilliance* which is defined as

$$\text{Brilliance} = \frac{\text{Intensity(photons/sec)}}{\text{Angular divergence(mrad}^2\text{).Source area(mm}^2\text{).(0.1\%bandwidth)}}. \tag{3.45}$$

The maximum brilliance for a third generation undulator is about 10 orders of magnitude higher than that for a rotating anode at the K_α-line. a Owing to these properties, SR has proven to be useful in a large number of physical, chemical, geological, and biological processes.

The main components of a syncrotron source are described below (Fig. 3.11). These

are—the injection and accelerator system, the storage ring, insertion devices and beam controls.

Injection and accelerator system: The injection system comprises an electron source, a low energy linear accelerator (LINAC), and a booster synchrotron (circular accelerator) where the electrons reach the operating energy, in one turn, before being transferred to the storage ring in a synchronized way. To reach high beam intensities in the storage ring, many booster pulses are injected. The process is initiated in the electron gun where high voltage electric field through a heated metallic cathode produces pulses of electrons which are directed toward the LINAC. In the LINAC, the electrons enter into the first radio frequency cavity which accelerates them and at the same time groups them into bunches. The electrons pre-accelerated in the LINAC are directed by a bending magnet toward a circular accelerator (booster synchrotron) where they are strongly accelerated to reach the final energy in the range of several giga-electron-volts (GeV) before being transferred to the storage ring. The booster synchrotron is a sequence of both bending magnets and focus-defocus magnets and radio frequency cavities along the circle.

Storage ring: A storage ring is a circular ring, whose structure is essentially the same as a synchrotron, and in which the electrons are kept circulating at constant energy for several hours. A storage ring consists of vacuum chambers for keeping an ultra-high vacuum along the particle trajectory, magnets for bending and focusing the circulating beam and radio frequency accelerating cavities for making up for energy lost as synchrotron radiation.

A low pressure ($\leq 10^{-9}$ torr) in the vacuum chamber is necessary for the electron beam to survive. Due to gas desorption caused by the radiation hitting the vacuum chamber surface a continuous pumping is required and it is carried out by placing many vacuum pumps along the circular path.

The magnetic system consists of bending magnets and focusing quadrupole and sextupole magnets. Dipole magnets are arranged along the electron orbit to modify the trajectory of the electron beam. The magnetic field of the magnets is kept constant in the storage ring because the electron beam energy has to be kept constant. There are photon beam ports at the location of the dipole magnets so that the synchrotron radiation may be utilized. Between the dipole magnets on the straight beam line section there are quadrupole magnets, which provide magnetic fields with gradients to act as lenses for the electron optics system. Sextupole magnets are used to correct the chromatic aberrations caused by focusing errors because of energy spread of electrons within a bunch. The electron beam is maintained in a stable oscillation (betatron oscillation) around an equilibrium orbit by the lens action with the magnets. In the arc sections of the storage ring, the electron beam loses energy by emitting synchrotron radiation. This energy loss is supplied by radio frequency cavities, which are set up on a straight section of the ring, and an associated power supply.

Insertion devices: Synchrotron radiation obtained from the bending magnets does not always fulfill the requirements of desired radiation characteristics like photon energy, broad band, narrow band,etc. In order to achieve the desired characteristics insertion devices are placed in the magnet-free, i.e, the straight sections of the orbit. An insertion device is made up of periodic magnets with periodically alternating polarity in the direction of motion of the electron beam. Therefore, the trajectory of electrons inside the insertion device wiggles like a section of sinusoidal curve. The insertion devices can be turned on or off without affecting the functioning of the storage ring. The insertion devices are wavelength shifters, wigglers, and undulators. In a wiggler the amplitude of the oscillations is rather large and the radiation from different wiggles add incoherently, whereas in undulators, the small-amplitude oscillations from the passage of a single electron produce a coherent addition of the radiation from each oscillation.

Beam controls: Beam controls are used to measure the circulating beam current, beam lifetime, and transverse beam position. The synchrotron radiations generated in the bending magnets or insertion devices are taken from the ports of the ring and delivered to the experimental station through a beam line. The main beam line is a light-path connecting the storage ring and the experimental station, and performs the function of extracting or cutting off the photon beam. Different types of optical instruments, such as reflection mirrors and monochromators, are set up in the beam line according to the characteristics of the synchrotron radiation to be used and the purpose of the experiment. A standard synchrotron beamline has the following parts:

Monochromator: Monochromators are used in order to extract a particular wavelength or energy from the white beam. For X-rays, silicon or germanium crystals are used as monochromators. When the white light impinges on the crystal, its lattice planes diffract X-rays of different wavelengths in different directions in accordance with Bragg's law. Another similar crystal parallel to the first is used to redirect the diffracted beam along the incident beam direction. Such an arrangement is called a *double crystal monochromator*.

Windows: Thin sheets of metal, often Beryllium, which transmit almost all of the beam, but protect the vacuum within the storage ring from contamination, are generally used as windows.

Slits: In order to define the horizontal and vertical beam size, several slits are used before impinging the beam on the sample.

Focussing mirror: One or more mirrors, which may be flat, bent-flat, or toroidal are used to collimate or focus the X-ray beam. Specialized lenses are also used.

Spacing tubes: Vacuum tubes which provide the proper space between optical elements, and shield any scattered radiation, are generally used in beamlines.

GISAXS experiments for our samples have been performed at P03 beamline of PETRA-

Beamline	P03, PETRA-II, DESY	BL-18B, PF, KEK
Source	Undulator	Bending magnet
Energy (keV)	13	10
Monochromator	Double crystal Si(111)	Double crystal Si(111) or Ge(220)
Detector	PILATUS 300k, Dectris	Cyberstar point detector
Image area (pixels)	487×619	NA
Pixel size (μm)	172	NA

Table 3.1: Specifications of the synchrotron X-ray scattering facilities used.

III, DESY, Germany [108, 114, 115] and some XR measurements have been carried out at the Indian Beamline BL-18B of Photon Factory, KEK, Japan. The specifications of the two beamlines are listed in Table 3.1.

3.2.2 Scanning probe microscopy

Scanning probe microscopy (SPM) is a family of surface imaging techniques that allows us to view the surface of samples with an amazing resolution. The first scanning probe microscope, the *scanning tunneling microscope* or STM, was invented by Binnig and Rohrer in 1982 [116, 117] and has proved to be extremely useful in many fields of condensed matter physics, chemistry and biology. The STM can resolve the local electronic structure at an atomic resolution on any conducting solid surface, thereby revealing the atomic structure of the surface. The STM utilizes the phenomenon of quantum mechanical tunneling in order

to image solid surfaces. It essentially consists of a probe tip attached to a piezodrive which consists of three mutually perpendicular piezoelectric transducers for motion in three directions. When the tip is brought to within a few angstroms of the sample surface the electron wave-functions in the tip and the sample overlap due to the proximity of the tip and the sample. On applying a bias voltage V between the two, an electrical current is made to flow. This current originates from the quantum mechanical tunneling effect and depends exponentially on the tip-sample separation. Thus the topography of the sample surface is obtained by plotting the tunneling current at each point of the scanned area [118, 119].

The STM, however, has certain limitations. In an STM, variations in the tunneling current are not necessarily due to variations in the tip-sample distance—variations may also arise from variations in the conductivity of the surface. So, an STM image may not represent the exact topography of the surface. Moreover, a scanning tunneling microscope cannot image thick insulating layers. Since the probing currents lie in the picoampere range, the maximum thickness of an insulating layer can be about 2 nm. These difficulties were overcome by the *atomic force microscope* or AFM [120] which images the sample surface by measuring the force between the sample and the probe tip on an atomic scale. The AFM is an extremely powerful instrument in that it can image almost any type of sample surface—from very hard samples like ceramic materials or dispersions of metallic nanoparticles, to very soft materials like polymers, human cells and molecules of DNA [121]. Also, it can be used both in ambient conditions as well as in vacuum according to the specific requirement of the experiment. Although initial images with the AFM did not have a resolution as high as that obtained with an STM, atomic resolution with an AFM was soon reported [122]. The Basic principle of the AFM has also led to the invention of a host of similar techniques like *magnetic force microscopy* (MFM), *friction force microscopy* (FFM), *dipping force microscopy* (DFM) and *electrostatic force microscopy* (EFM) [123].

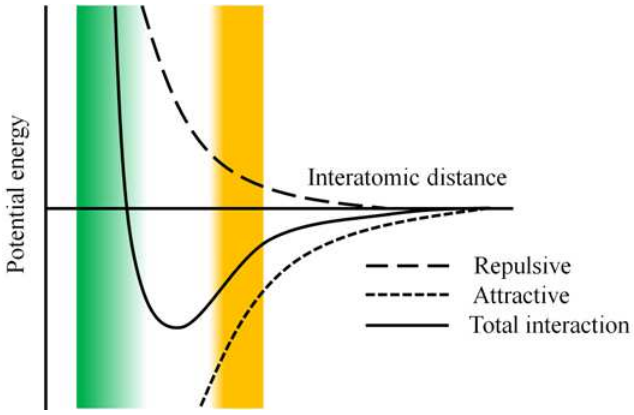

Figure 3.12: The Lennard-Jones potential.

In our work we have used atomic force microscopy technique to obtain the topography of the sample surface, the details of which are described in what follows.

3.2.2.1 Basic principles

The forces between the tip and the sample can be understood by considering the attractive and repulsive forces at different distances. The attractive van der Waals forces and the Pauli repulsion due to overlapping electron orbitals can be described together by the Lennard-Jones potential (Fig. 3.12)

$$V(d) = 4\varepsilon\left[\left(\frac{\sigma}{r}\right)^{12} - \left(\frac{\sigma}{r}\right)^{6}\right], \tag{3.46}$$

where ε is the depth of the potential well, σ is the finite distance at which the inter-particle potential is zero and r is the distance between the particles. When r is large weak attractive forces exist between the tip and the sample. When the tip and the sample are brought closer to each other, attractive forces increase until the distance becomes so small that the electron clouds start repelling each other electrostatically. The increasing repulsive force weakens the attractive force as the interatomic distance decreases and at a distance of about 2 Å the

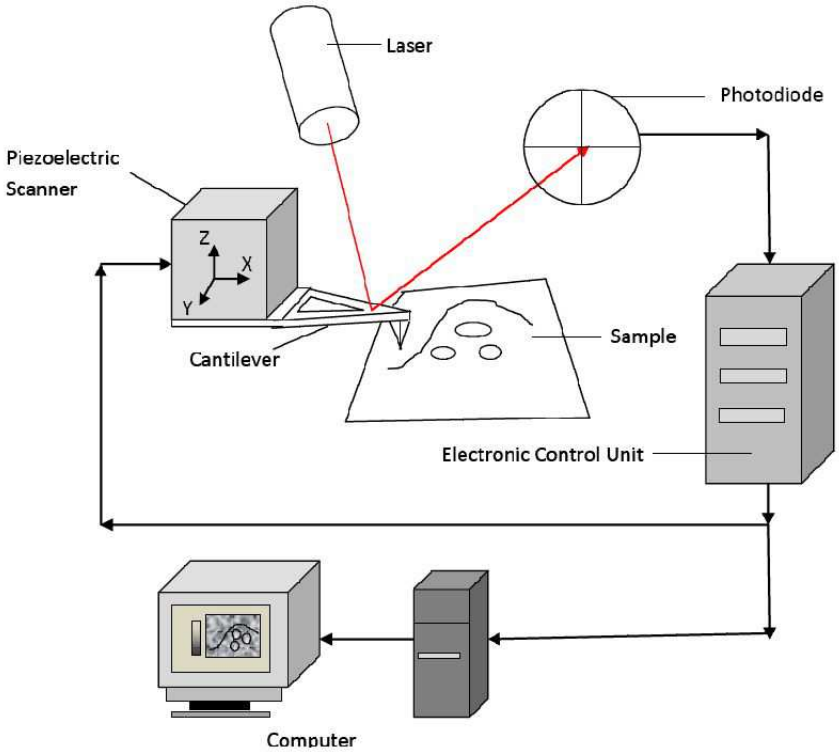

Figure 3.13: Schematic diagram of an atomic force microscope.

interatomic force becomes zero. When the distance is even smaller, the interatomic force is fully repulsive [124].

A typical AFM essentially consists of a probe tip attached to a cantilever which is mounted on a piezoelectric transducer (scanner) for moving the tip over the sample surface, a force transducer (sensor) that senses the force between the tip and the sample, and a feedback control that feeds the signal from the sensor back to the piezoelectric scanner in order to maintain a constant force. The expansion coefficient for a single piezoelectric device is on the order of 0.1 nm per applied volt, i.e, approximately the radius of a single atom. The ability to control such tiny movements makes piezoelectric materials the perfect choice for use in AFM. Piezoelectric transducers come in various shapes and sizes and are used in complex geometries so that they can control the movement of the tip in multiple

directions across the sample surface.

The force between the sample and the tip is measured by the force transducer. When the tip comes in contact with the sample surface the voltage output from the transducer increases. Generally, an AFM uses a cantilever with integrated tip (the probe), and an optical lever as the force transducer. The optical lever consists of a laser beam which is focused to a point on the back of the reflecting cantilever. The beam is then reflected to a four-segment photo-detector which measures the position of the laser spot. When the probe tip, mounted on the front side of the cantilever, interacts with the sample, the reflected light changes its path. The change in light is monitored by the four quadrants of the photo-detector and this gives a measure of the force. The control electronics take the output from the force transducer and use it to drive the scanner, so as to maintain a fixed tip-sample distance and hence, a constant force between the sample and the tip. Thus, if the sensor detects an increase in force, e.g, due to a particle on the surface, the feedback control makes the tip move away from the surface and vice-versa.

Modes of operation: The AFM is typically operated in three topographic modes—(i) contact mode, (ii) non-contact mode and (iii) tapping mode.

(i) Contact mode: The simplest mode of operation is the contact mode, which was the first mode developed for the AFM. It is also the fastest of all topographic modes, as the deflection of the cantilever gives us the topography of the sample directly. In this mode the tip remains in close contact with the sample surface and the interaction force between the tip and the sample is the repulsive van der Waal's force, which dominates over any other attractive force that may try to act. Additionally, two other forces are operational in this regime—capillary force due to the presence of a contaminant layer on the sample surface and the force exerted by the tip itself, which is the shear force component of the interaction force acting on the cantilever. Assuming that the contaminant layer is homogeneous, the

capillary force is constant throughout the sample and is attractive in nature. The magnitude and direction of the cantilever forces acting on the sample, however, depend on the deflection and spring constant of the cantilever. The force exerted on the surface by the probe tip in contact mode is given by Hooke's law,

$$F = -k \times D, \tag{3.47}$$

where F is the force, k is the probe force constant and D is the deflection.

The AFM can be operated in two ways in the contact mode—the *constant force mode* and the *constant height mode*. In the constant force mode a feedback system keeps the cantilever deflection at a constant predetermined value known as the *set-point*. As the tip scans the sample surface, the AFM software can display the deflection signal as a line plot or as an image. In the contact mode, the topography is measured by the voltage applied by the feedback amplifier to the piezo element and this applied voltage is expressed as a function of the lateral position of the sample. This function is used to generate the surface topography of the specimen. In the constant height mode the feedback loop is turned off altogether and the piezo scanner holding the cantilever scans the sample surface without moving in the z-direction. So the image signal comes entirely from the deflection of the cantilever and not from the voltage applied to the z-piezo which is kept constant. The constant height mode suffers from the disadvantage that any steep step in the sample surface may cause the tip to crash against the sample and thus damage the tip. So the constant force mode is the most commonly used mode of operation. The main advantage of using contact mode AFM is its high resolution. In spite of that, it finds limited use as the applied normal force leads to a high lateral force on the sample as well which might lead to distortion, deformation or even removal of weakly adsorbed layers on the surface. So contact mode

AFM is not suitable for imaging soft samples.

(ii) Non-contact mode: Non-contact mode AFM is carried out in the attractive regime of the potential energy-distance curve. The tip has to be close enough to the surface to achieve high sensitivity, without passing on to the repulsive regime. Usually the tip remains about 50 Å to 150 Å above the surface. Since these attractive forces are much weaker than repulsive forces appearing in contact mode, the cantilever has to be give a small oscillation and by monitoring the dynamic effects of the attractive force, i.e, the change in oscillation, the tip can be maintained at a close proximity to the sample surface without plunging into the repulsive regime. The forces between the cantilever and the sample surface, normally the attractive van der Waals force, leads to a change in the cantilever resonant frequency, which in turn leads to changes in the oscillation amplitude and phase. Far from the sample surface the resonant frequency is given by

$$\omega_0 = c\sqrt{k}, \tag{3.48}$$

where c is a function of the cantilever mass and k is the spring constant. However, when there is an additional force f from the surface, the new resonant frequency is given by [125]

$$\omega_0' = c\sqrt{k - f'}, \tag{3.49}$$

where f' is the derivative of force f normal to the surface. Either the change in amplitude or the change in phase, which is derived from the change in frequency, can be used in the feedback circuit to maintain the tip at a fixed distance from the sample surface. In order to avoid the possibility of damaging or contaminating the tip by slipping into the repulsive regime, a high frequency cantilever, with ω_0 between 300 and 400 kHz, is generally used.

Additionally, oscillation amplitudes are kept small, typically about 10 nm, and scanning speed is lower than in contact mode. Frequency modulation is often used when scanning in UHV conditions.

Non-contact mode AFM can be employed in almost any situation but suffers from a main drawback that in ambient conditions the force between the tip and the sample is mainly governed by the capillary force due to a contaminant layer, which significantly affects the resolution of the image. However, since it offers imaging with little or no contact between the tip and the sample, the non-contact mode is highly effective in imaging soft materials like polymers and biological samples.

(iii) Intermittent contact or tapping mode: In this case, the feedback is based on amplitude modulation and the tip-sample interaction passes through all three regimes, namely, the zero-force regime, the attractive regime and the repulsive regime. As the interaction passes through the repulsive regime, there can be damage of the sample or tip due to tip-sample contact. However, as the tip moves perpendicular to the sample, lateral forces are almost absent. It is noticeable that in this case the tip passes through the contamination layer. This is the reason for the huge success of the intermittent contact mode—on the one hand it avoids the possibility of tip crashing due to lateral forces as in contact mode, while on the other it overcomes the problem of losing information due to capillary forces (due to contamination layer) as in non-contact mode. Here the restoring force of the cantilever withdraws the tip from the contamination layer in each cycle, thereby diminishing the effect of capillary forces on the image. In intermittent contact AFM the amplitude of oscillation of the probe is large, typically in the range of 1 to 100 nm, and the feedback is usually based on the amplitude signal.

At present, intermittent contact is the most widely used mode for imaging in ambient conditions. It can also be used for imaging in liquid, although it is limited by the presence

of certain difficulties specific to operation in liquids. It is not commonly used in vacuum, due to restrictions in bandwidth due to increase of Q in vacuum.

Analysis of AFM images: Characterization of surface morphology can be done by performing Power Spectral Density (PSD) analysis. It describes the content of spatial frequencies in the surface. The PSD (S) is given by the modulus of the Fourier transform of the height z as

$$S(k_x) \propto \lim_{L\to\infty} \frac{1}{2L} \left| \int_{-L}^{L} z(x) \exp\left(ik_x x\right) dx \right|^2 , \tag{3.50}$$

where $2L$ is the scan length and k_x is the spatial frequency.

PSDs reflect two features of the surface—the distribution of heights from a mean plane and the lateral distance over which this height variation takes place [126]. Using the ABC or K-correlation model,

$$S(k_x) = \frac{A}{\left[1 + (Bk_x)^2\right]^{C/2}}, \tag{3.51}$$

one can extract the correlation length of the surface from the experimentally obtained PSD plotted against spatial frequencies [127–129]. Here A is the value of the spectrum in the low frequency limit, B is a correlation length or the *shoulder parameter* which marks the transition from the low frequency to the high frequency behavior and C is the exponent of the power law fall-off at high frequencies. The correlation length is complementary in nature to the *in-plane* feature size obtained from GISAXS images.

3.2.2.2 Instruments

For our experiments AFM imaging in UHV conditions was performed using the Variable Temperature Ultra High Vacuum Scanning Probe Microscope (VT UHV-SPM) (beam deflection AFM, Omicron Nanotechnologies) (Fig. 3.14). It uses a single tube scanner with

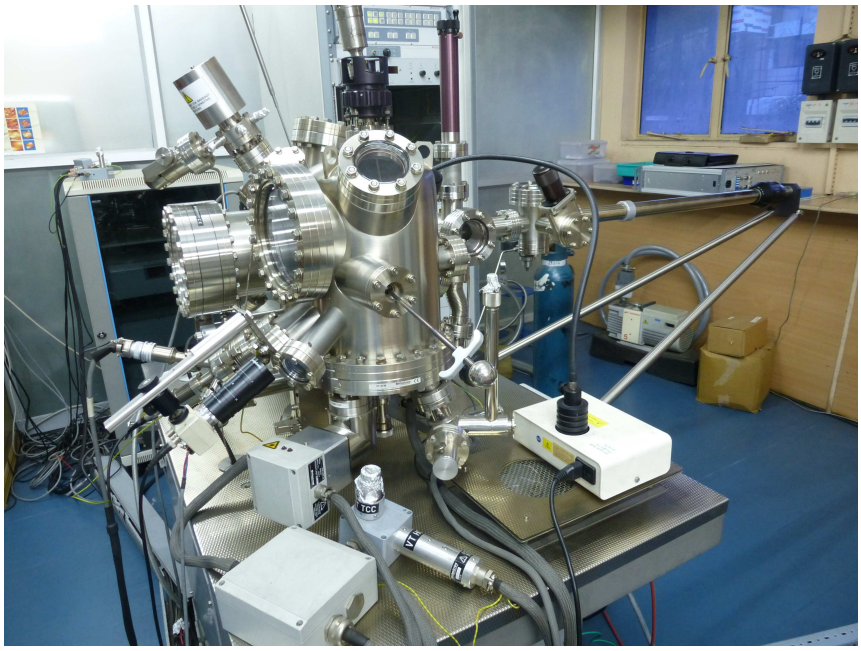

Figure 3.14: The Variable Temperature Ultra High Vacuum Scanning Probe Microscope from Omicron.

a maximum scan range of 10 μm $\times$ 10 μm and a z-travel of about 1.5 μm. A z-resolution of better than 0.01 nm is achievable. The scanner is positioned with a 3-axes linear piezomotor. It uses slip/stick effects related to inertia forces when a piezo is driven in a fast/slow sequence. The sliders are magnetically coupled to three shear piezos that are driven with a sawtooth voltage input. The sliders are transported during the slow movement of the piezo and slip during the fast piezo motion. A high quality vibration decoupling system, essential for successful high-resolution SPM, is provided by the spring suspension system, whose resonance frequency is about 2 Hz. The sample stage is suspended by four soft springs protected by surrounding columns. Vibrations of the spring suspension system are interpreted using a nearly non-periodic eddy current damping mechanism. For this reason the sample stage is surrounded by a ring of copper plates which come down between permanent magnets. The spring suspension system can be locked to allow for tip or sample changes by

Figure 3.15: The ambient AFM 5500SPM from Agilent Technologies.

means of a wobblestick. This locking is achieved through a push-pull motion feedthrough.

AFM imaging in ambient conditions were done using the 5500SPM from Agilent Technologies. It has a probe attached to a cantilever which is mounted on a scanner made from a piezo ceramic material. There are four scanners for scanning in different scan ranges. A photodiode detector is used to receive the reflection of the laser spot off the back of the cantilever. The top and bottom halves of the detector monitor the cantilever deflection (the Deflection signal) for AFM imaging, while the two side halves record the cantilever twisting (the Friction signal) for lateral force imaging. The sample stage is positioned below the tip using three magnetic posts and is attached with micrometer screws for manual movement in the x-y plane with total travel of $\pm$5 mm. Two laser alignment knobs located on top of the scanner are used for positioning the laser spot on the cantilever. A video system allows one to locate regions of interest and align the laser on the probe tip. It includes

a camera and optics on an adjustable stand along with a separate illumination source. A USB cable connects the camera to the computer. The entire arrangement is enclosed in a vibration isolation chamber, as shown in Fig. 3.15, in order to isolate it from vibration, air turbulence and acoustic noise which can have adverse effects on imaging. To an extent, it also helps control temperature variability.

3.2.3 Optical spectroscopy

Several methods of spectroscopy, in different regions of the electromagnetic spectra, have emerged in the past decades and have provided efficient means of structure characterization. These include electronic (optical, i.e, ultra-violet and visible) spectroscopy, infra-red and Raman spectroscopy, microwave spectroscopy and nuclear magnetic resonance spectroscopy. The choice of spectroscopic method to be applied in a particular situation depends on the structure and properties of the sample in question and the type of information sought. Optical spectroscopy provides information about the group character of the molecules of a sample, and does not furnish much detail about the individual structural aspects. Nevertheless, by studying the spectra of a number of different molecules, it has been possible to correlate the spectral signatures with the structure of a molecule. For these reasons, ultra-violet and visible (UV-vis) absorption spectroscopy has become a routine procedure for characterizing organic compounds [130]. In our experiments we have used UV-vis spectroscopy to characterize both solutions and solid films.

3.2.3.1 Basic principles

The electronic spectra of molecules appear in the wavelength range from 100 to 800 nm of the electromagnetic spactrum. The visible region extends from 400 to 800 nm and the

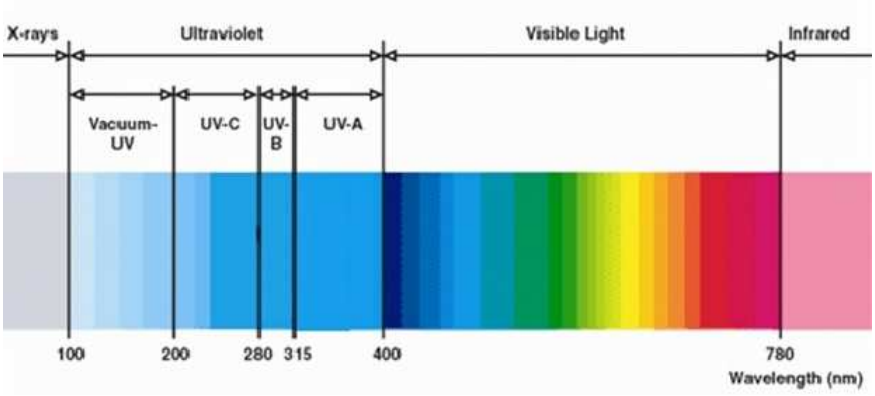

Figure 3.16: The electromagnetic spectrum showing the ultra-violet and visible regions.

ultra-violet region from 100 to 400 nm (Fig. 3.16). The ultra-violet region is further divided into two spectral regions. The range between 200 and 400 nm is called the near ultra-violet region and that below 200 nm is called the far or vacuum ultra-violet region. The colour of a material as detected by the human eye is due the particular wavelength of light reflected by the material, and is the complement of colour of incident light absorbed by it [131].

Electronic spectra can be classified into two categories, emission spectra and absorption spectra. Emission spectra are obtained by analyzing the light emitted by a luminous source. On the other hand, absorption spectra are obtained by analyzing the light transmitted through an absorbing medium kept between the light source and the spectroscope. We are mainly interested in absorption spectroscopy whose principles are discussed below.

When a molecule absorbs radiation, its energy increases and this increase is equal to the energy of the incident photon,

$$E = h\nu = \frac{hc}{\lambda}, \tag{3.52}$$

where h is the Planck's constant, ν and λ are the frequency and wavelength, respectively, of the incident radiation, and c is the velocity of light. The increase may occur in the

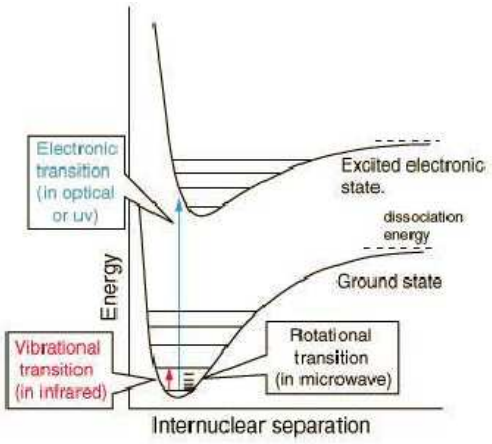

Figure 3.17: Schematic diagram showing molecular energy levels and related transitions.

vibrational, rotational or electronic energy of the molecule. Electronic transitions require comparatively larger quanta of energy than vibrational transitions. Transitions between rotational levels require even smaller quanta of energy (Fig. 3.17). Since each electronic level is associated with a number of vibrational levels, and each vibrational level with a number of rotational levels, the electronic spectra of a molecule is far more complicated than rotational or rotation-vibration spectra. Thus, an electronic spectrum appears as a band spectrum or a band envelope, due to a large number of closely spaced sub-levels.

Absorption intensity—Lambert-Beer law: The Lambert-Beer law of light absorption states that the fraction of incident light absorbed is proportional to the number of molecules in the path. So, if a substance is dissolved in a solvent, the absorption will depend on the molecular concentration of the solution, provided the solvent itself does not absorb in that range of wavelength. The law can be expressed as

$$\text{Absorbance or extinction or optical density} = \log \frac{I_0}{I} = \epsilon c l, \tag{3.53}$$

where ϵ is the absorption coefficient, c is the concentration and l is the path length. The

absorption intensity is usually expressed in terms of ϵ. The absorption spectrum is obtained by scanning the entire wavelength range of the incident beam and measuring the transmitted signal.

In case of aggregates of conjugated polymers, as in our experiments, there exist two types of fundamental electronic interactions—intrachain and interchain interactions. For example, in π-conjugated lamellar stacks, electronic excitations are delocalized in two directions, along the polymer chains as well as between the chains. Such interactions can be explained in terms of the H and J aggregate model, originally proposed by Kasha to treat aggregates of small molecules [132]. In conjugated polymer assemblies intrachain through-bond interactions give rise to J-aggregate behaviour, while interchain Coulombic interactions give rise to H-aggregate behaviour. The optical properties of such conjugated polymer assemblies are regulated by a competition between these two types of interactions [19].

3.2.3.2 Instrument

A spectrometer generally consists of a radiation source, a sample container, a monochromator, a detector and a detector output measuring instrument. Incandescent lamps or discharge tubes are used as sources in the ultra-violet and visible regions. Prisms or gratings serve as monochromators, while photographic plates or photoelectric cells serve as detectors (Fig. 3.18).

The spectrometer used in our experiments is Lambda 750 UV/Vis/NIR spectrometer, Perkin Elmer, USA. It uses a tungsten halogen filament lamp and a deuterium discharge lamp as radiation sources in the visible and ultra-violet regions, respectively. It is suitable for measurements in the scanning wavelength range between 190 and 3300 nm with a resolution of 0.17 - 5.00 nm. The lamp is enclosed in a quartz envelope which exhibits excellent

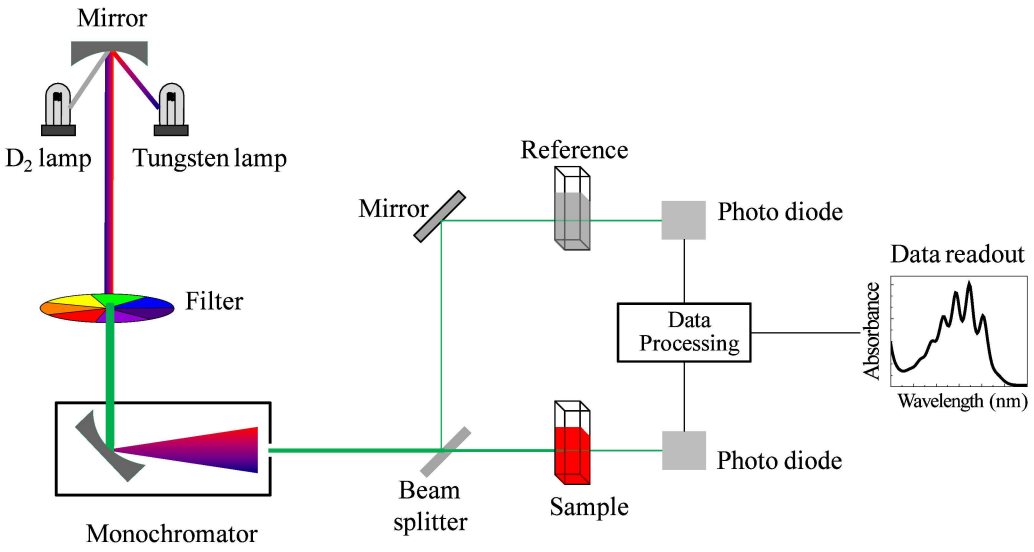

Figure 3.18: Schematic of a UV-visible spectrometer

ultra-violet transmission. A double holographic grating monochromator is used, which is a combination of two single monochromators where the exit slit of the first monochromator is the entrance slit of the second. In order to optimize the system performance holographic grating grooves with either parallel or of unequal distribution are used. Holographic gratings are generated on planar, spherical, toroidal and many other surfaces. The monochromator selects a narrow band of wavelengths from the radiation source and this beam of light then passes through a beam chopper which is a rotating mirror that rotates around its own axis several times per second and during each rotation it chops the incident beam. In other words, it alternately splits the beam into two parts—one part passes through the sample and is called the 'sample beam' and the other passes through the reference and is called the reference beam. The detector also measures the signal from the sample and the reference alternately, in synchronization with the chopper. When light passes through the sample the

detector measures the sample signal I and when the light passes through the reference it measures I_0. Finally the electronic circuit compares I and I_0 to compute the absorbance and transmittance. The sample compartment is provided with a lid to protect the detector from strong external light. Samples can be liquids contained in cuvettes or solid films on substrates. The cuvettes and substrates must be of materials that are transparent to ultra-violet and visible light. Usually quartz is used for the purpose as it is transparent to a wide range of wavelengths from ultra-violet to infra-red regions. The cuvettes used have a 10 mm square cross-section, which means that the path length is 10 mm. It holds about 3 ml of solution. In order to convert the radiation falling upon it into an electrical signal, two types of detectors are used in this spectrometer—high sensitive photomultiplier tube and Peltier cooled PbS detector, for detection in the UV/Vis and IR ranges, respectively.

3.2.4 Dynamic light scattering

Dynamic light scattering (DLS) or *photon correlation spectroscopy* is a technique widely used for measuring the size distribution of particles in solution. The size of the particles is related to the change in the wavelength of the incident light due to Doppler shift when a monochromatic light is shone on a solution containing the particles, which are in Brownian motion. This method is highly suited for measuring the size distribution of spherical particles in solution and can also be extended to non-spherical particles like nano-rods, etc. With the advent of laser sources, highly monochromatic light has become easily available, and performing DLS measurements has become a routine procedure for size characterization, with the advantage that it is not time-consuming. The first DLS measurements were done by Pecora in 1964 and soon afterwards, laser light was used as the incident radiation by Cummins *et al.*(1964) and the next decade was devoted to testing theoretical predictions

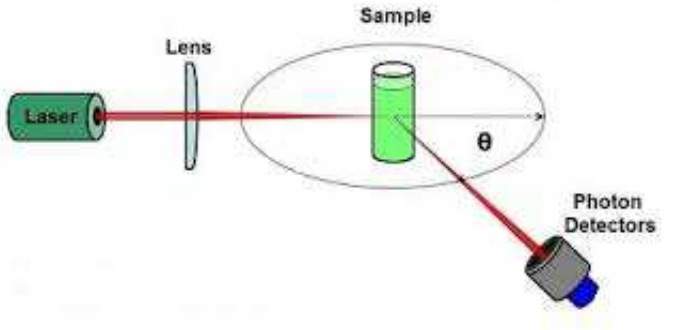

Figure 3.19: Schematic diagram showing the DLS measurement setup.

for simplified systems like translational and relaxational modes for spheres, rod-like and coil-like particles [133].

3.2.4.1 Basic principles

In a typical light scattering experiment a beam of light is focused on a region of a fluid in a cuvette and the scattered light is detected. The polarizations of the incident and scattered beams are defined by using polarizers and analyzers, respectively. The instantaneous scattered signal is, in fact, the superposition of waves scattered by different scatterers, and therefore, fluctuates in response to the molecular motion of the scatterers.

When light impinges on matter, the electric field of the incident light induces an oscillating polarization of the electrons in the molecules, which then act as secondary sources of light and subsequently scatter light. The size, shape and molecular interactions in the scattering medium decide the frequency shifts, angular distribution, intensity and polarization of the scattered light [134]. Rayleigh scattering occurs as long as the size of the particles is small compared to the wavelength of incident radiation. If the source is a laser, i.e, a monochromatic and coherent source, the intensity of the scattered light fluctuates over time, as the scatterers undergo Brownian motion and the distances between them change

continuously with time. So the scattered light undergoes constructive or destructive interference due to light scattered from different scatterers and this intensity fluctuation actually contains information about the time scale of movement of the scatterers.

Information about the dynamics of the system can be obtained from the auto-correlation of the intensity trace recorded during an experiment. The second order auto-correlation curve is derived from the intensity plot as

$$g^2(K;\tau) = \frac{\langle I(t)I(t+\tau)\rangle}{\langle I(t)\rangle^2}, \tag{3.54}$$

where $g^2(K;\tau)$ is the auto-correlation function at a particular wave vector K and delay time τ and I is the intensity. When τ is small, the auto-correlation is high as the particles do not have sufficient time to change their positions from the initial states. As the delay time increases the correlation decreases exponentially and at very large τ, there is no correlation between the scattered intensities in the initial and final states. For a monodisperse sample the decay is a single exponential. The relation between the first order and second order auto-correlation functions is as follows.

$$g^2(K;\tau) = 1 + \beta[g^1(K;\tau)]^2, \tag{3.55}$$

where $g^1(K;\tau)$ is the first order auto-correlation function, β is a correction factor which depends on the geometry and alignment of the laser beam in the scattering setup. The auto-correlation function is used to estimate the size of the scatterers.

Since, for a monodisperse population the first order auto-correlation function can be

approximated by a single exponential decay, we can write

$$g^1(K;\tau) = \exp(-\Gamma\tau), \tag{3.56}$$

where Γ is the decay rate. The decay rate is related to the translational diffusion coefficient D_t as

$$\Gamma = D_t K^2, \tag{3.57}$$

where K is the scattering vector and is related to the refractive index of the solvent ($\tilde{n}_0$), wavelength of incident light (λ_0) and scattering angle (θ) by the relation

$$K = \frac{4\pi\tilde{n}_0}{\lambda_0}\sin\frac{\theta}{2}. \tag{3.58}$$

A plot of Γ/K^2 vs. K^2 may or may not show an angular dependence. Small spherical particles do not show any angular dependence due to the absence of any anisotropy and hence the plot is a horizontal straight line . For particles of any other shape, there is an anisotropy and hence, an angular dependence in the plot of Γ/K^2 vs. K^2. The intercept gives the value of D_t, from which the *hydrodynamic radius* (r_h) can be calculated using Stokes-Einstein equation as

$$r_h = \frac{k_B T}{6\pi\eta D_t}, \tag{3.59}$$

where k_B is the Boltzmann constant, T is the absolute temperature and η is the viscosity of the solvent. The hydrodynamic radius thus obtained is the radius of a sphere that moves in the same manner as the scatterer and hence, is not the actual size of the scatterer in case of non-spherical particles. Thus, for a polymer in coil-like conformation, the hydrodynamic radius is not the same as the radius of gyration.

3.2.4.2 Instrument

DLS experiments have been performed on Zetasizer Nano-S, Malvern Instruments Ltd., Malvern, UK. The main components of the instrument are—a light source (4 mW HeNe laser of wavelength 633 nm) to illuminate the scatterer, an avalanche photodiode detector, a Peltier temperature controller which can change the temperature form 2 to 92°C and a 5 ml glass cell serving as the sample container. The light source irradiates the sample in the glass container and the light is scattered in all directions. The detector measures the scattered light at a fixed scattering angle (173° backscatter).

CHAPTER 4

P3DDT FILMS FROM SOLUTIONS IN PURE GOOD SOLVENTS

4.1 Introduction

The importance of the casting solvent in the formation of ordered films of crystalline polymers has been discussed by several authors. A proper choice of solvent is crucial for obtaining high field-effect mobility and high luminescence from polymers like P3DDT and also for their use in solar cells. In the spin-coating process the crystallization kinetics of P3AT films is controlled by the kinetics of evaporation of the solvent. Thus, the film is formed in a far-from-equilibrium condition when a fast-evaporating solvent is used [27]. Generally, chloroform is used as the solvent for depositing films of poly(3-alkylthiophenes) (P3ATs) in the active layer of field-effect transistors. But the low boiling point and high evaporation rate of this solvent restricts the time needed for the formation of well ordered crystallites in spin-coated films and results in low mobilities, ~ 0.01 cm^2/(V s). Chang *et al.* have

shown that a good solvent with a higher boiling point, like 1,2,4-trichlorobenzene, can significantly increase the field-effect mobility of P3HT-based devices to 0.12 $cm^2/(V\ s)$ with a high on-off ratio of 10^6 [48]. The reason behind this improvement is that a slower evaporation rate of the solvent effects in the formation of a highly crystalline film with stronger interchain interactions which results in a marked increase in conductivity. On the other hand, the electroluminescence (EL) and photoluminescence (PL) properties of P3ATs are found to depend on the solubility of the polymer in a solvent. Lee *et al.* have demonstrated that a poorer solvent increases the luminescence intensity of P3AT films [135]. They have argued that in a good solvent the polymer adopts a more expanded structure with longer π-conjugation lengths so that the excitons can migrate to quenching sites easily, thereby lowering the luminescence intensity. In a poor solvent, the polymer adopts a more compact structure which restricts the excitons to shorter segments of the chains, thus increasing their probability of relaxing via emissive routes. Shin *et al.* have shown that the PL intensity of P3AT films cast from tetrahydrofuran (THF) is an order of magnitude higher than that obtained from films cast from chloroform, toluene or *p*-xylene [136]. They also showed that the wavelength corresponding to the maximum of the EL spectra can be shifted from blue to orange by simply changing the casting solvent. The solvent and solute concentration is also seen to play a crucial role in the performance of solar cells with composites of P3ATs in the active layer [137–139].

It is known that in addition to the solvent, the surface free energy or the varying potential energy landscape of the substrate surface can also control the substrate-polymer interactions and thus the orientation, ordering and packing of the molecules near the interface [140]. Kline *et al.* have shown that the orientation of polymer crystallites near the substrate is different from that in the bulk of the film and that treating the substrate with a self-assembled monolayer can influence the concentration of the crystallites near

the substrate to a considerable extent [49]. Apart from these factors, the spin-coating speed is also expected to play an important part in controlling the microstructure of the polymer films. This is because the structure depends on the rate of solvent evaporation from the solution during spinning, which, in turn, depends on the spinning speed [141]. Since the rate of solvent removal from the film, and hence the rate of solidification of the film, is directly related to the spinning speed, slower speeds are likely to result in the formation of near-equilibrium structures.

In this work we have explored some of the issues that are of considerable importance in controlling the morphology, and hence the properties, of spin-coated P3DDT films. The influence of the solvent and solution concentration on the microstructure of the films is discussed. Also, the variations in the microstructure of the films with distance from the substrate, and their connection to the substrate surface modification as well as the spinning speed, are investigated in detail. We have utilized the XR technique to investigate the effect of concentration of polymer, solvent, substrate surface nature and spinning speed on the out-of-plane structure or morphology of the spin-coated P3DDT thin films on silicon, with special emphasis on the structure near the film-substrate interface. Formation of π-stacked aggregates in the spin-coated P3DDT thin films are confirmed from the optical absorption spectra. Strong influence of solvent has been observed in the ordering of the films. The possible parameters of the solvent, which may influence such ordering in the films, both near the substrate and away from it, are discussed. The dependence of film thickness on the concentration of the casting solution is also discussed.

4.2 Experiments

Regioregular poly(3-dodecylthiophene) (P3DDT) was purchased from Sigma-Aldrich (average molecular weight: 60,000, regioregularity $\geq$ 98.5 %) and used as received. Chloroform (CF, $CHCl_3$) and toluene (TL, C_7H_8) were obtained from Merck and chlorobenzene (CB, C_6H_5Cl) was obtained from Sigma-Aldrich. Polymer solutions were prepared by dissolving different amounts of P3DDT in CF, CB and TL solvents. The concentration of polymer in CF and CB solutions varies from 1 to 4 mg/ml, while that in TL solution varies from 1 to 3 mg/ml. H-terminated Si (H-Si) substrates were prepared through standard pre-treatment method as described in Chapter 3. Films were then prepared from different polymer solutions on the H-Si substrates using a spin-coater (SCS 6800 Spin Coater Series) at a speed of 3500 rpm for 60 s and were labeled as c-SV, where c represents the concentration of polymer and SV represents the solvent (i.e. CF, TL or CB). To check the effect of substrate surface nature on the film structure, films were also prepared from some of the solutions on the clean native oxide coated Si (O-Si) substrates at the same speed (3500 rpm). For optical study films of nearly similar thickness were prepared on the clean quartz glass substrates at the same speed (3500 rpm). A set of films was prepared from a P3DDT-TL solution on O-Si substrates by changing the spinning speed (ω) from 500 to 4000 rpm. However, continuous films could not be prepared from P3DDT-CF and P3DDT-CB solutions on O-Si substrates for low ($\leq$ 1000 rpm) spinning speed. Thickness and EDP of films on Si were analyzed using XR technique and optical properties of films on quartz glass were measured using UV-vis spectroscopy as described in Chapter 3.

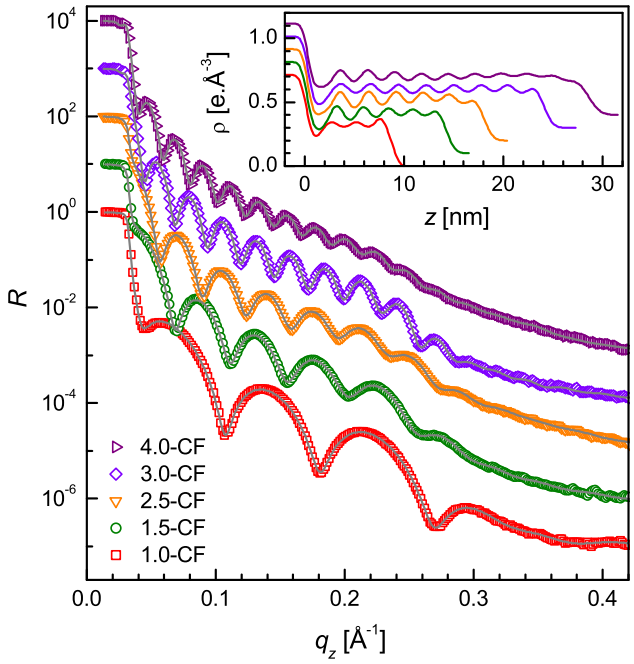

Figure 4.1: XR data (different symbols) and analyzed curves (solid line) of the spin-coated P3DDT thin films deposited from solutions of different concentrations of polymer in chloroform (CF) solvent. Inset: corresponding analyzed EDPs. Curves and profiles are shifted vertically for clarity.

4.3 Results and discussion

4.3.1 Effect of solvent

XR data of the spin-coated P3DDT thin films on H-Si substrates for different concentrations of polymer dissolved in CF, TL and CB solvents are shown in Figs. 4.1, 4.3 and 4.5, respectively. Oscillations or Kiessig fringes, which are the measure of the total film thickness, are very clearly evident in all the XR profiles. A broad hump (around $q_z \approx 0.24$ Å^{-1}) or modulation in the Kiessig fringes with prominent fall in the fringes' intensity after $q_z \approx 0.26$ Å^{-1} is also observed in all the XR profiles. Such modulation provides the ex-

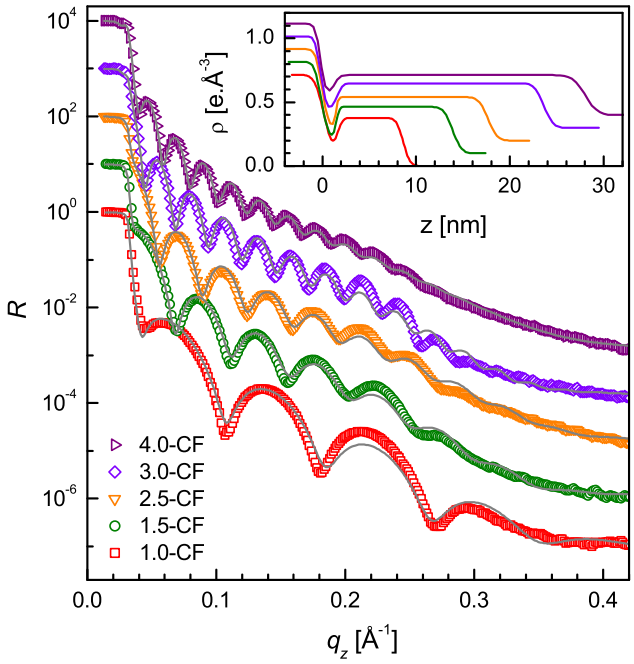

Figure 4.2: XR data (different symbols) and analyzed curves (solid line) of the spin-coated P3DDT thin films deposited from solutions of different concentrations of polymer in chloroform (CF) solvent. Analysis has been carried out considering substrate and two layers. Inset: corresponding analyzed EDPs. Curves and profiles are shifted vertically for clarity.

istence of some layering or ordering in the system. The value of d-spacing obtained from the position of the hump is about 2.6 nm, which is suggestive of an edge-on orientation of the polymer chains. The number of Kiessig fringes, hence the film-thickness, increases with concentration, as expected. The Kiessig fringes and the modulation also depend on the solvent, apart from the concentration, which are clearly evident in Figs. 4.7 and 4.8, where the XR profiles for films prepared from three different solvents are plotted for comparison. The number of fringes is minimum for the films prepared from CB solvent, while maximum for the films prepared from CF solvent (see Fig. 4.7). That means more polymer is required for TL solvent compared to CF solvent and even more for CB solvent to get similar number of fringes (see Fig. 4.8). On the other hand, the amplitude of modulation

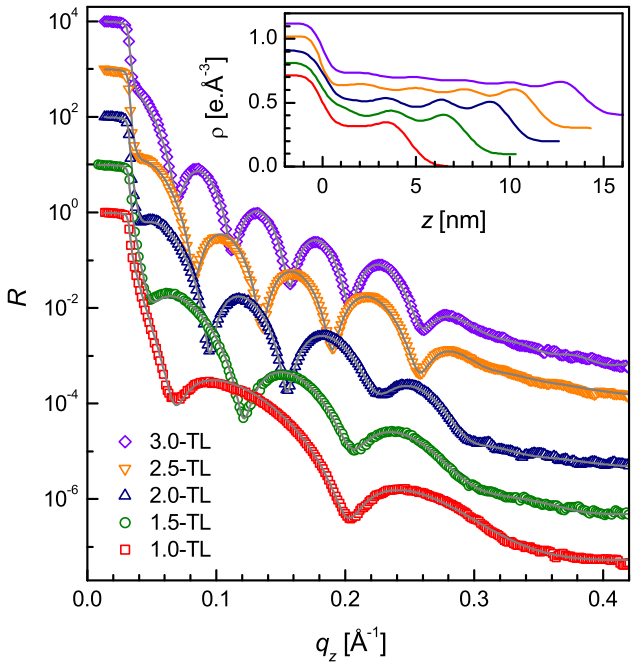

Figure 4.3: XR data (different symbols) and analyzed curves (solid line) of the spin-coated P3DDT thin films deposited from solutions of different concentrations of polymer in toluene (TL) solvent. Inset: corresponding analyzed EDPs. Curves and profiles are shifted vertically for clarity.

is minimum for the films prepared from TL solvent, while nearly same for the films prepared from CF and CB solvents. To get the quantitative information about the films, all XR profiles have been analyzed using Parratt's formalism [95] after incorporating roughness at each interface. It is necessary to mention that a single layer above the substrate can not fit the data. Similarly, two layers above the substrate, one for the interfacial layer and another for the remaining portion, can create some modulation but cannot fit the data completely (as shown in Figs. 4.2, 4.4 and 4.6). Especially it cannot reproduce the sudden decrease in the intensity of Kiessig fringes after $q_z \approx 0.26$ Å^{-1}. Thus for the analysis, each film has been divided into a number of bilayers after the interfacial layer. Each bilayer of thickness about 2.6 nm is constituted of two parts: alkyl side chains (low electron density) and

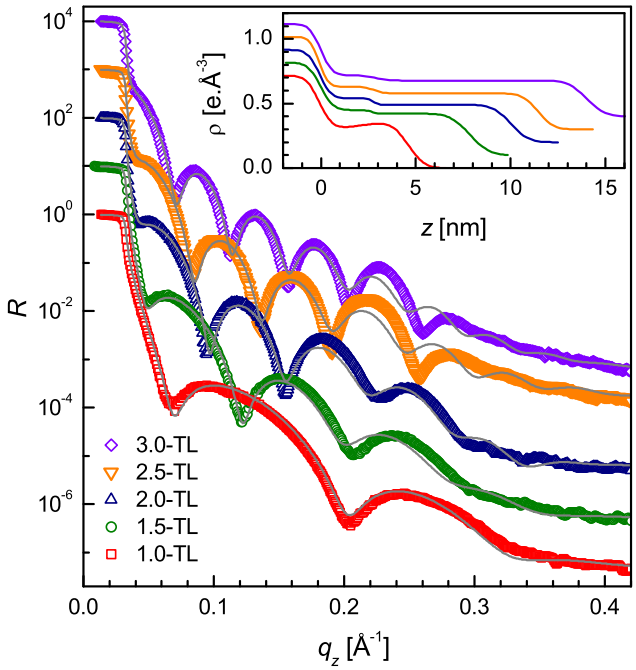

Figure 4.4: XR data (different symbols) and analyzed curves (solid line) of the spin-coated P3DDT thin films deposited from solutions of different concentrations of polymer in toluene (TL) solvent. Analysis has been carried out considering substrate and two layers. Inset: corresponding analyzed EDPs. Curves and profiles are shifted vertically for clarity.

polythiophene backbones (high electron density). The best fit XR profiles along with the corresponding EDPs are shown in Figs. 4.1, 4.3, 4.5, 4.7 and 4.8. The ordering in the film above the interfacial region is found to vary with solvent and concentration. Also the EDPs for the films prepared from TL solvent show a broad hump, while for the films prepared from CF and CB solvents show a dip near film-substrate interface. This indicates that the attachment and orientation of the polymer with the substrates for the TL solvent is different from that for the CF and CB solvents.

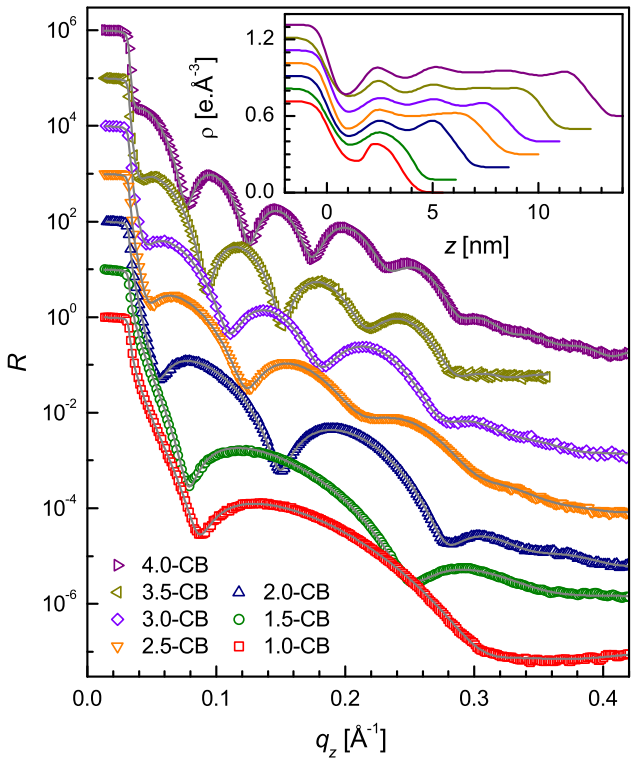

Figure 4.5: XR data (different symbols) and analyzed curves (solid line) of the spin-coated P3DDT thin films deposited from solutions of different concentrations of polymer in chlorobenzene (CB) solvent. Inset: corresponding analyzed EDPs. Curves and profiles are shifted vertically for clarity.

4.3.2 Effect of substrate and spinning speed

In order to understand the role of substrate nature on the structure of the film, XR data of P3DDT thin films on H-Si and O-Si substrates for polymer dissolved in CF, TL and CB solvents are shown in Fig. 4.9. There is almost no substrate effect in the XR profiles for the films prepared using CF and CB solvents. While in the XR profiles for the films prepared using TL solvent, the hump near $q_z \approx 0.24$ Å^{-1} is found prominent for the film on O-Si substrate compared to that on H-Si substrate. To get the quantitative information about the films, all XR data are analyzed as before and the best fit XR profiles along with the

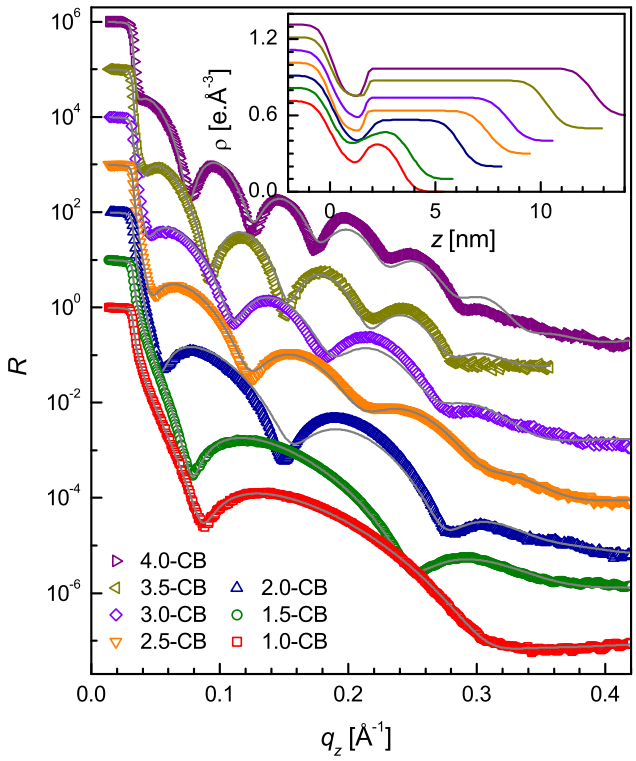

Figure 4.6: XR data (different symbols) and analyzed curves (solid line) of the spin-coated P3DDT thin films deposited from solutions of different concentrations of polymer in chlorobenzene (CB) solvent. Analysis has been carried out considering substrate and two layers. Inset: corresponding analyzed EDPs. Curves and profiles are shifted vertically for clarity.

corresponding EDPs are shown in Fig. 4.9. It is clear from the EDPs that the structures of the films on H-Si and O-Si substrates are almost same for films prepared from either CF or CB solvent, while those are on H-Si and O-Si substrates are different for films prepared from TL solvents. For the latter a broad hump near film-substrate interface is observed on H-Si substrate (as observed before and shown in Fig. 4.3), while a dip near film-substrate interface is observed on O-Si substrate. This indicates that the attachment and orientation of the polymer with the O-Si substrates prepared using TL solvent is similar to that prepared using CF or CB solvent on any kind of (H-Si or O-Si) substrate.

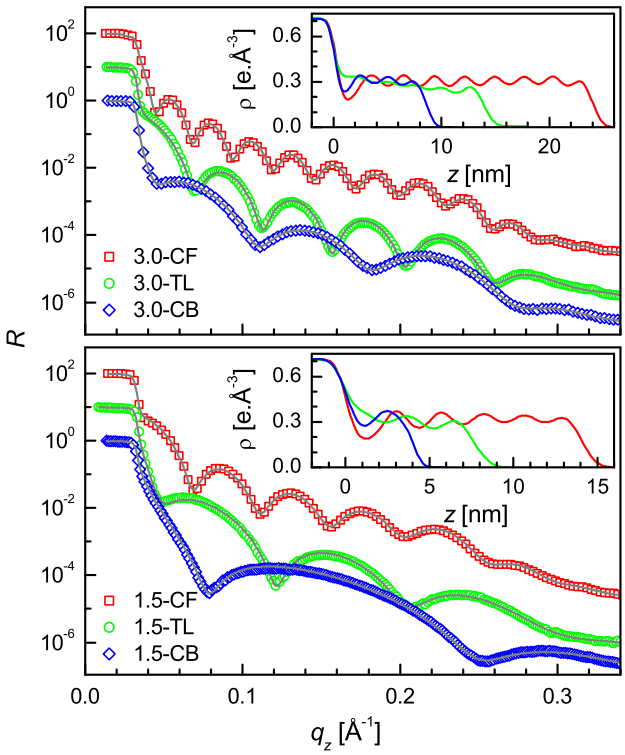

Figure 4.7: XR data (different symbols) and analyzed curves (solid line) of the spin-coated P3DDT thin films deposited from solutions of two concentrations (3.0 and 1.5 mg/ml) of polymer in different solvents (curves are shifted vertically for clarity). Insets: corresponding analyzed EDPs.

The XR data of P3DDT thin films on O-Si substrates prepared at different spinning speeds, for polymer dissolved in TL solvent, are shown in Fig. 4.10. The number of Kiessig fringes decreases with the increase of spinning speed. The number of Kiessig fringes, hence the film-thickness, decreases with the increase of spinning speed, as expected. A broad hump near $q_z \approx 0.24$ Å^{-1} is also observed for all the films, which is particularly prominent for the high thickness (slow speed) films. To get the quantitative information about the films, all XR data are again analyzed as before and the best fit XR profiles along with the corresponding EDPs are shown in Fig. 4.10. A dip near film-substrate interface is found for all the films. Also ordering is found in the film which varies with the film-thickness.

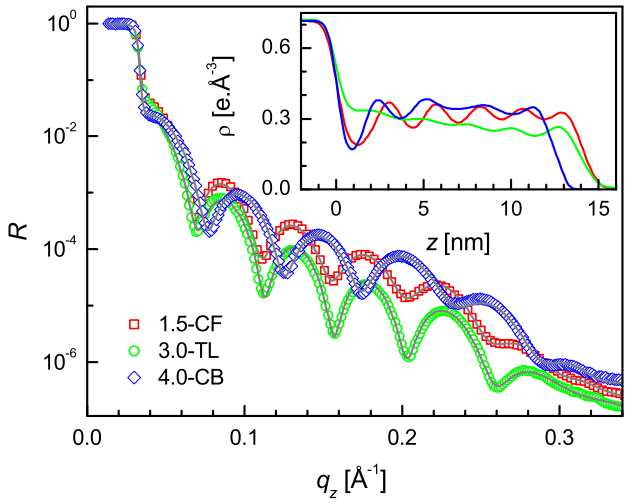

Figure 4.8: XR data (different symbols) and analyzed curves (solid line) of the spin-coated P3DDT thin films of nearly same thickness deposited from solutions containing different concentration of polymer in different solvents. Inset: corresponding analyzed EDPs.

4.3.3 Optical absorption and π-stacking

The UV-vis absorption spectra of three spin-coated P3DDT thin films of similar thickness on quartz glass substrates prepared using CF, TL and CB solvents are shown in Fig. 4.11. Considering information of Fig. 4.8, 1.5-CF, 3.0-TL and 4.0-CB solutions were used to get similar film-thickness from different solvents. Four shoulders/peaks are visible in all the spectra. The peaks near 490 and 610 nm are well resolved, while the peaks near 530 and 560 nm are not, especially for the 1.5-CF and 4.0-CB films. The appearance of peaks may originate from π-stacking of the P3DDT chains [142], where the peak at 610 nm is due to the interchain π-π transition, while the peaks at 560, 530 and 490 nm are due to the 0-0, 0-1 and 0-2 transitions of the intrachain exciton [143]. The observed spectral signatures can also appear due to weakly interacting H-aggregates [144]. Thus the presence of H-aggregates or lamellae structures due to π-stacking are clearly evident in all the spin-

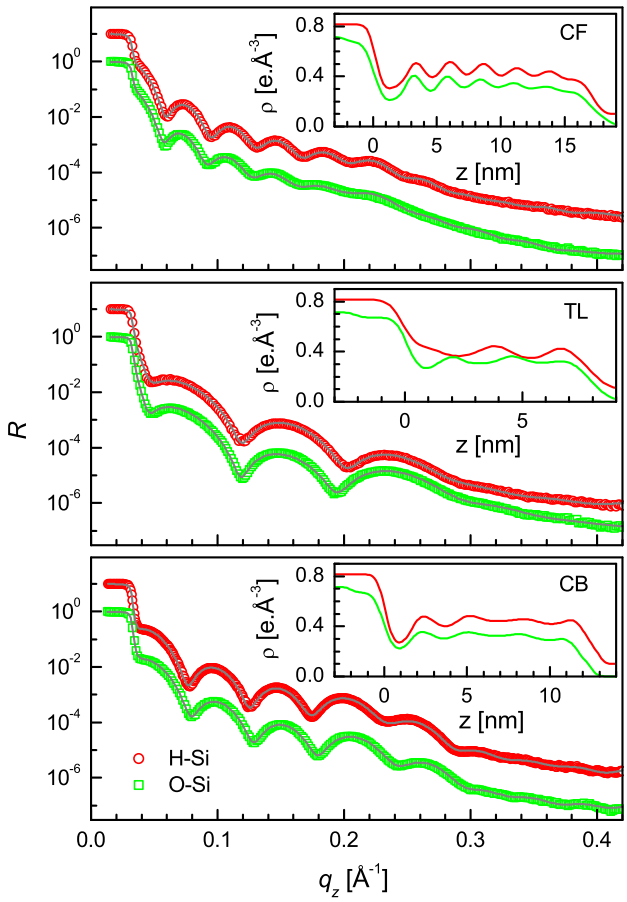

Figure 4.9: XR data (different symbols) and analyzed curves (solid line) of the spin-coated P3DDT thin films on H-Si and O-Si substrates deposited from solutions containing polymer in different solvent. Inset: corresponding analyzed EDPs. Curves and profiles are shifted vertically for clarity.

coated films. The absence of a peak near 450 nm (which appears due to coil-like P3AT chains comprising twisting and bending of the thiophene rings) indicates absence of any appreciable amount of coil-like P3DDT chains in the films. The peak at 490 nm can also result from the intrachain π-π transition of the planar rod-like conformation of the P3DDT chains. Thus the slightly intense peak at 490 nm for the 1.5-CF and 4.0-CB films compared to the 3.0-TL film indicates the presence of a larger number of free rod-like chains in the

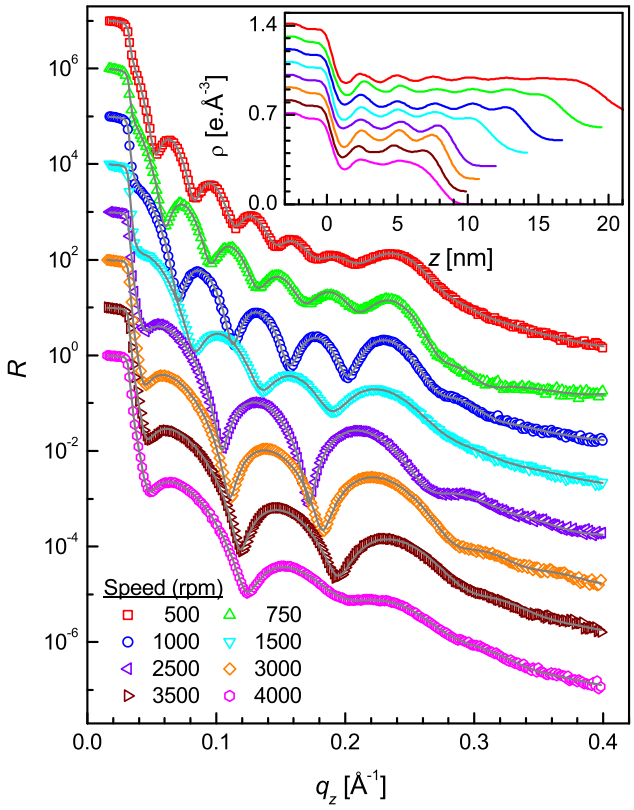

Figure 4.10: XR data (different symbols) and analyzed curves (solid line) of the spin-coated P3DDT thin films deposited on O-Si substrates at different spinning speed from a solution of polymer dissolved in TL solvent. Inset: corresponding analyzed EDPs. Curves and profiles are shifted vertically for clarity.

former two. Less intense 490 nm peak and better resolved 530 and 560 nm peaks for the 3.0-TL film compared to the others suggest that in the 3.0-TL film greater number of rod-like chains have organized themselves into ordered aggregates or lamellae. This, in general, suggests that the structures of the films prepared using TL solvent are slightly different from those prepared using CF and CB solvents. In particular, the lamellae structures of the films on glass substrates seem to be more uniform for films prepared using TL solvent compared to those prepared using CF and CB solvents.

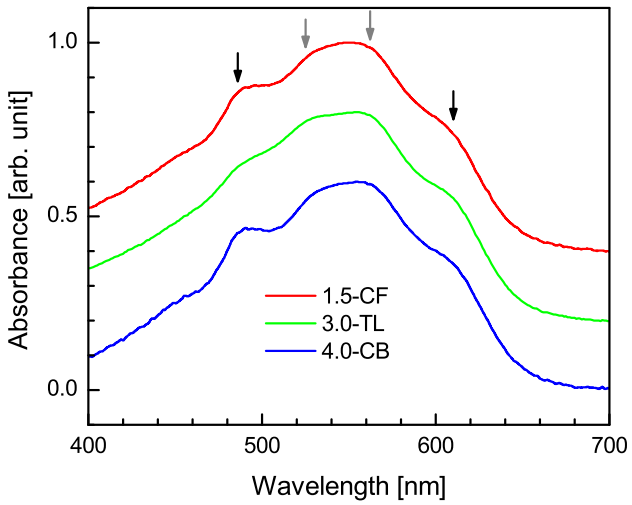

Figure 4.11: UV-vis spectra of the spin-coated P3DDT thin films of similar thickness on glass substrates prepared using CF, TL and CB solvents. Peak positions are indicated by arrows.

4.3.4 Effect of concentration on film thickness

The dependence of the thickness of spin-coated polymer films on the concentration of the casting solutionis well-known for standard polymers like polystyrene and has been divided into three regimes. Very low concentrations, i.e. very dilute solutions lead to low coverage and inhomogeneous films. Low concentration or semi-dilute solutions lead to homogeneous films, the thickness of which varies linearly with concentration. Above a critical concentration, the viscosity of the solution comes into play due to entanglement of the polymer chains. In this case the relation between the thickness and the concentration still remains linear but with an increasing slope [36]. The film thickness has a well-known empirical relationship with different internal physical parameters (such as viscosity of solution and evaporation-rate, etc. of solvent) and external parameters (such as spinning speed) as stated in Eq. 3.1. However, investigating the dependence of thickness on concentration

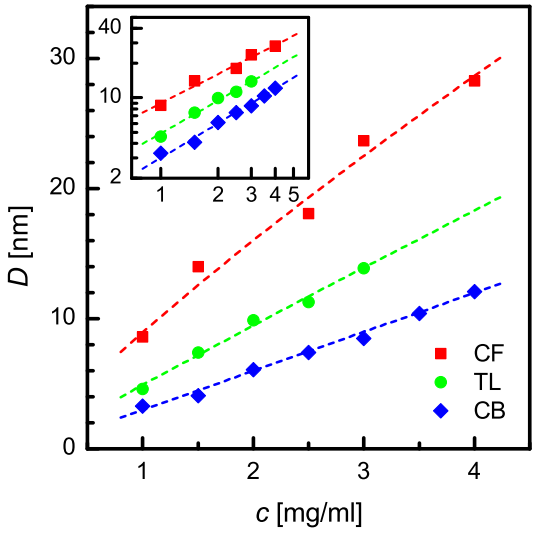

Figure 4.12: Variation of film-thickness as a function of polymer-concentration for different solvents. Dashed lines through the data are the analyzed curves. Inset: corresponding variation in log-log scale.

can still be of considerable interest in case of semicrystalline polymers like P3DDT where layering occurs.

The variation of the film thickness (D) with the polymer concentration (c) for different solvents are plotted in Fig. 4.12. From Eq. 3.1 it is clear that the effect of concentration (c) of the polymer in the above expression comes only through η. To take into account the fact that $D \to 0$ when $c \to 0$, the η in Eq. 3.1 needs to be replaced with η_d, which is a viscosity change ($\eta - \eta_0$) related term and can be expressed as

$$\eta_d \approx \eta_0 (c/\rho_m)^{\alpha/0.36}, \tag{4.1}$$

where η_0 is the viscosity of the solvent, ρ_m is the mass density of the solvent, which converts c from mg/ml to weight % and α is an exponent. Using Eq. 4.1 in Eq. 3.1, D can be

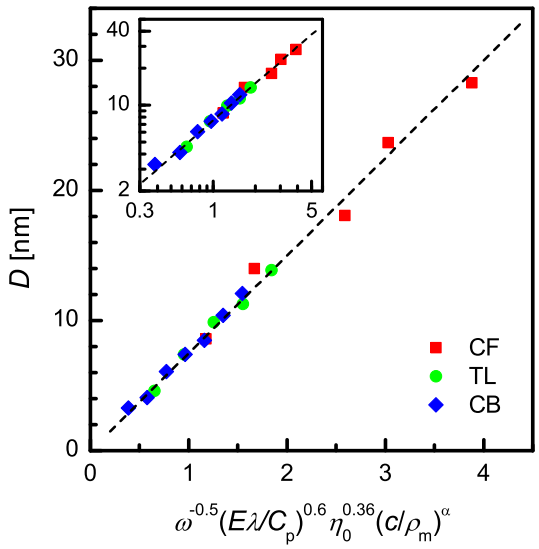

Figure 4.13: Variation of film thickness (D) as a function of polymer concentration (c) and solvent parameters dependent modified variable. Inset: corresponding variation in log-log scale. Dashed lines through the data are the analyzed straight lines.

expressed as

$$D \approx K_0'\omega^{-0.50}(E\lambda/C_p)^{0.60}\eta_0^{0.36}(c/\rho_m)^{\alpha} \quad (4.2)$$

$$\approx Ac^{\alpha}, \quad (4.3)$$

where $A = K_0'\omega^{-0.50}(E\lambda/C_p)^{0.60}\eta_0^{0.36}\rho_m^{-\alpha}$ and K_0' is a modified constant for the volatile organic solvents.

Eq. 4.3 has been used to analyze the variations of D with c for different solvents and are shown in Fig. 4.12. The values of α obtained from the analysis are 0.84, 0.95 and 1 for CF, TL and CB solvents, respectively. To check the validity of Eq. 4.2, the term other than K_0' of the right hand side of that equation is first calculated for all the films considering the values of different parameters as listed in Table 4.2 and the values of c and α as mentioned before and then D is plotted as a function of that term in Fig. 4.13. The data can be well

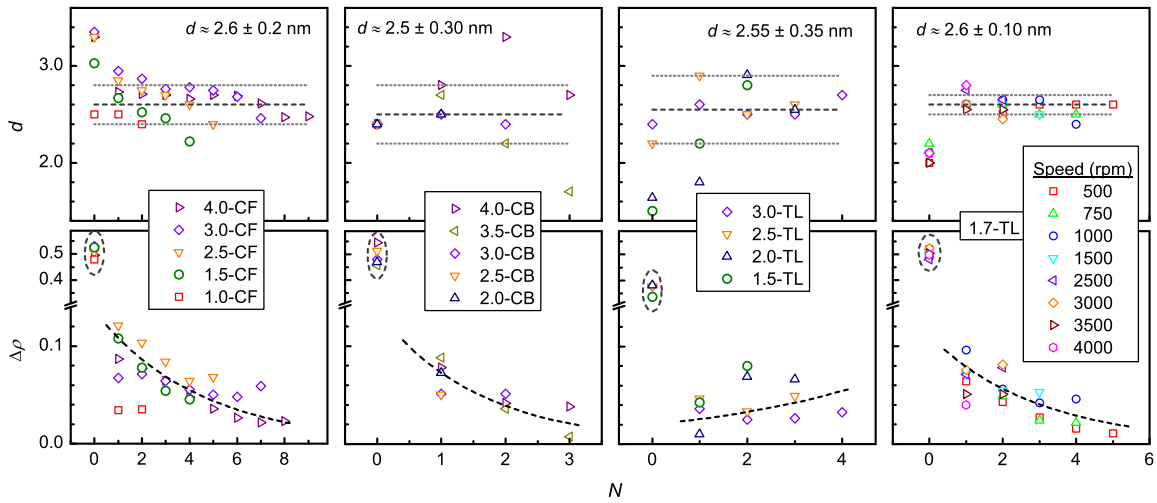

Figure 4.14: Variation of the bilayer thickness (d) and the bilayer electron density contrast ($\Delta\rho$) with number of layer (N) for different films.

represented through a straight line as shown in Fig. 4.13. This confirms not only the validity of the Eq. 4.2 but also the different values of α for different solvents as obtained before.

4.3.5 Structural analysis

The ordering of polymer in a film can be understood considering the variation of the bilayer thickness in it and the density contrast between two parts of a bilayer. Small variation and large contrast indicate better ordering, while large variation and small contrast indicate the reverse. Thus information of both the parameters is important. In addition the information about the attachment of the film with the substrate is also important. In this view, the thickness (d) and the electron density contrast ($\Delta\rho$) for different bilayers starting from the substrate for all the films are plotted in Fig. 4.14. The value of $\Delta\rho$ for $N = 0$ indicates the electron density difference between substrate and film at the film-substrate interface. The value of this $\Delta\rho$ for the films deposited from CF and CB solvents is greater than 0.4 e.Å^{-3}, while that for the films deposited from TL solvent on H-Si substrates is less than

Table 4.1: Parameters, such as the average electron density (ρ_a) of film, its deviation ($\Delta\rho_{in}$) near film-substrate interface to form dip/hump ($-/+$) of thickness (d_{in}), the average bi-layer thickness (d) with its standard deviation (σ_d), the maximum electron density contrast ($\Delta\rho_m$) and the exponential decay length (ζ) for the P3DDT thin films prepared from solutions containing either chloroform (CF), chlorobenzene (CB) or toluene (TL) solvents on H-Si or O-Si substrates by varying the polymer concentration (c) or the spinning speed (ω).

Solvent	Substrate	Variation	ρ_a (e.Å^{-3})	$\Delta\rho_{in}$ (e.Å^{-3})	d_{in} (nm)	$d \pm \sigma_d$ (nm)	$\Delta\rho_m$ (e.Å^{-3})	ζ* (nm)
CF	H-Si	c	0.30±0.02	−0.08±0.03	3.0±0.4	2.60±0.20	0.14	11.4
CB	H-Si	c	0.30±0.02	−0.08±0.05	2.4±0.1	2.50±0.30	0.14	4.0
TL	H-Si	c	0.30±0.02	+0.04±0.02	2.0±0.5	2.55±0.35	0.05	−5.0
TL	O-Si	ω	0.30±0.02	−0.08±0.02	2.1±0.1	2.60±0.10	0.11	7.8

*normally decay from film-substrate interface toward top surface, while '−' means reverse.

0.4 e.Å^{-3} but on O-Si substrates is again greater than 0.4 e.Å^{-3}. It can be noted that the difference between substrate electron density and average film electron density is about 0.4 e.Å^{-3}. The deviation of electron density near interface ($\Delta\rho_{in}$) from the average film electron density (ρ_a) for the four sets of films are tabulated in Table 4.1. The positive and negative signs indicate hump and dip, respectively. The value of the interfacial thickness (d_{in}), i.e. the value of d for $N = 0$, which represents the width of the first hump or dip are indicated in Table 4.1. A dip followed by a peak indicates that the attachment of the film with the substrate is through alkyl side chains of the predominantly edge-on oriented polymer. The absence of a dip indicates no preferential attachment and/or orientation of the polymer. The value of the width of the dip is found to vary, which is maximum for the films prepared using CF solvent and minimum for the films on the O-Si substrates prepared using TL solvent.

The value of $\Delta\rho$ after the interfacial region is found to be maximum, which then decreases gradually towards the top surface for the film where dip is present at the interface. The situation is however reverse for the film where hump is present at the interface. Such

Table 4.2: The mass density (ρ_m), the viscosity (η_0), the evaporation rate (E) and the dipolarity (SdP) for different solvents, as obtained from online sites.

Solvent	ρ_m (g/ml)	η_0 (cP)	E	SdP
Chloroform	1.48	0.54	11.6	0.614
Toluene	0.87	0.55	2.4	0.284
Chlorobenzene	1.11	0.75	1.1	0.537

a variation of $\Delta\rho$ can be expressed using the standard exponential decay function [145]

$$\Delta\rho(N) = \Delta\rho_m \exp(-Nd_a/\zeta), \tag{4.4}$$

where $\Delta\rho_m$ is the maximum value of $\Delta\rho$, d_a is the average d value and ζ is the critical decay length. The values of these parameters are tabulated in Table 4.1. The negative value of ζ essentially indicates exponentially increasing nature of $\Delta\rho$, where $\Delta\rho_m$ is the minimum value. The value of d is found to vary with film-thickness, the standard deviation (σ_d) of which is included in Table 4.1 along with the average value d_a. In general, the electron density profile of the film from the first peak (after dip or hump near interface) can be expressed as

$$\rho(z) = \rho_a + \frac{1}{2}\Delta\rho_m e^{-z/\zeta} \cos\left(\frac{2\pi z}{d_a \pm \sigma_d}\right). \tag{4.5}$$

Small $\Delta\rho_m$-value, large negative ζ-value and large σ_d-value for the films prepared using TL on H-Si substrate are indicative of the poor ordering in the film due to the absence of any preferential attachment and/or orientation of the polymer near substrate. The value of $\Delta\rho_m$ for the films prepared using CF and CB solvents are relatively high. For the films prepared using CF solvent, the value of ζ is comparatively large and that of σ_d is small, suggesting that the ordering in this film is better. On the other hand, although the value

of $\Delta\rho_m$ and ζ for the films prepared using TL solvent on the O-Si substrates are small compared to those for the films prepared using CF solvent, the small value of σ_d for the former provides quite good ordering.

The structure of the films can be better understood by combining the information on ordering, obtained from EDP, with the information on aggregate formation from optical absorption, which are schematically shown in Fig. 4.15. The attachment and the orientation of the polymer with the substrate strongly depend on the solvent and/or the nature of substrate. Such differences are generally related to diffusion, adsorption and pinning effects [146]. The different properties of the solvents, which can give rise to the different polymer-solvent interaction, are tabulated in Table 4.2. Our results suggest that the diffusion of polymers in the TL solvent is less (may be due to low mass density and dipolarity values [147, 148]) compared to those in the CF and CB solvents, at least near the substrate, while the tendency of adsorption on the H-Si substrate seems to be slightly more compared to that on the O-Si substrate (due to the difference in the hydrophobic/hydrophilic nature). The effect of adsorption is noticeable only when the diffusion is small, accordingly we see a pinning effect and poor ordering on the H-Si substrate, and less pinning and better ordering on the O-Si substrate for films cast from TL solvent. On the other hand, when the diffusion is relatively large, the pinning is less and the ordering is better on the substrate, independent of its nature (H-Si or O-Si), as observed for the films prepared using CF and CB solvents. The d-value in the polymer aggregates prepared using CF and CB solvents has large variation (i.e., less uniform) compared to that prepared using TL solvent on O-Si substrate. However, the variation is systematic for the P3DDT-CF/H-Si films, i.e., large d-value (corresponding to the more relaxed or Form-I-like structure) towards the film-substrate interface, probably due to low viscosity (η_0), while smaller d-value (corresponding to the more interpenetrating or Form-II-like structure) towards the top surface,

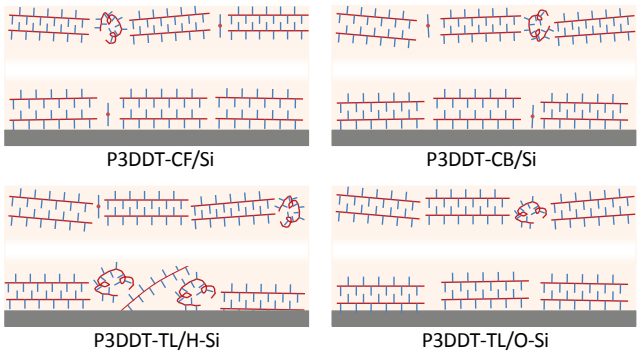

Figure 4.15: Model structures and electron density profiles for the P3DDT films. (a) and (b) represents the $c-$CF and $c-$CB films, where the ordering of polymer near the substrate is good and that deteriorates with the height; (c) and (d) represents the $c-$CL film, where the ordering of polymer near the substrate is poor and that improves with the height.

probably due to high evaporation rate (E) of CF solvent. On the other hand, although the evaporation rate is low, the high viscosity of CB hinders the ordering and the formation of a relaxed structure in the P3DDT-CB/Si films. The moderate values of both the parameters for the TL solvent help to enhance the ordering near the film-air interface overcoming the pinning effect in the P3DDT-TL/H-Si films. Although the variation of d-value in the P3DDT-TL/O-Si films is small, the relative fluctuation between lamellae along z-axis is more (as $\Delta\rho_m$-value is less) compared to that in the P3DDT-CB/Si films.

4.4 Conclusions

Structures of spin-coated P3DDT thin films, prepared using different polymer concentrations and solvents were investigated using XR and UV-vis spectroscopy techniques. Strong dependence of solvent and substrate surface nature on the ordering or layering of the edge-on orientated P3DDT in the films, near the substrate and away from it, are observed from EDP. The ordering of P3DDT, if present near the film-substrate interface, is maximum there

and decays exponentially along the film-thickness. The maximum value, the exponential decay length and the d-value and its deviation vary with the solvent. For instance, better ordered Form-I-like relaxed structure of higher d-value near the film-substrate interface and less ordered interpenetrating Form-II-like structure of lower d-value toward the film-air interface are found in the films prepared from CF, which are related to the low viscosity and high evaporation rate, respectively, of the solvent. Similarly, less ordered mixed d-value structures are found throughout the films prepared from CB, which are related to the high viscosity of the solvent, even though its evaporation rate is low. In the films prepared from TL on weakly hydrophobic H-Si substrates, no ordering is seen near the substrate due to less diffusion of P3DDT in TL and appreciable pinning on the substrate, while appreciable ordering near the film-air interface is seen, overcoming the pinning effect, due to the moderate values of both viscosity and evaporation rate of the solvent. In the films prepared from TL on weakly hydrophilic O-Si substrate, ordering is found near the substrate due to less pinning on the substrate even though the diffusion of P3DDT in TL is less. The hindrance in the formation of continuous film on the O-Si substrate at low speed from CF and CB is related to the high evaporation rate of CF and high viscosity of CB, while the continuous film from TL is related to the moderate values of both the parameters for TL. Such moderate values also help to form films with less variable d-values, resulting in better ordering of P3DDT in the film prepared from TL on O-Si. However, the relative fluctuation between aggregates along the film-thickness is slightly more in the film prepared from TL compared to that prepared from CF. Thus the ordering of edge-on orientated P3DDT due to π-stacked aggregates (responsible for charge delocalization) and absence of any appreciable amount of coil-like P3DDT chains (responsible for charge localization) in spin-coated thin films, especially near the film-substrate interface, can be regulated by varying the solvent, substrate surface nature and spinning speed.

CHAPTER 5

P3DDT FILMS FROM SOLUTIONS IN MIXED GOOD AND POOR SOLVENTS

5.1 Introduction

Different approaches have been made to increase the cystallinity and control the morphology and microstructure of P3AT films like optimizing the processing parameters, thermal annealing, solvent vapour treatment, etc. [149] A relatively simple method of preparing 1D aggregates of P3ATs had been proposed by Kiriy et al. [150]. This method suggests that by adding a poor solvent one can induce ordered main chain collapse of the P3AT molecules resulting in the formation of 1D aggregates driven by solvophobic interactions. A poor solvent having lower volatility than the main solvent resides within the evolving film for a longer time during solvent evaporation, thus aiding in the growth of ordered aggregates [151]. 2D single crystalline nanosheets of P3HT were prepared by Yu et al. using slow evaporation of a diluted mixture of solvents [152]. It was shown that the ratio

of the good-to-poor solvents can control the size of the nanostructures. Later on, Chang et al. showed that a high volatility solvent can also lead to enhanced supramolecular assembly if it interacts with the main solvent through hydrogen bonding [153]. However, not much has been studied about poly(3-dodecylthiphene) (P3DDT) which has the longest alkyl side chain among the P3ATs. The longer side chain is responsible for its better solubility, but hinders its crystallizability due to side chain interactions. Because of this reason P3DDT tends to crystallize into spherulites and not nanowhiskers. Xu et al. reported on the successful formation of P3DDT nanowhiskers by the addition of anisole, a poor solvent for P3DDT, to a solution of P3DDT in chlorobenzene or carbon disulfide which are good solvents for the polymer [75]. In this case the crystallites or aggregates were prepared by heating the mixed solution and subsequent cooling and aging the solution, like others. However, no attempt had been made to study P3DDT films prepared from solutions of different good-to-poor solvent ratio, without heating the solutions, and subsequently annealing such films at different temperatures. Such a treatment helps us to understand the definite role of solvent mixing and annealing temperature on the structures of the P3DDT films and hence enables us to prepare P3DDT films with structures that have possibility to show better device properties.

In this work, we have tried to understand the exact role of the poor solvent and annealing temperature on the structures of the P3DDT films, using complementary techniques. For that, P3DDT films, which were first prepared from solutions containing different chlorobenzene-to-anisole ratio without heating and then subsequently annealed at different temperatures, were studied using X-ray diffraction (XRD), grazing incidence X-ray scattering (GISAXS), atomic force microscopy (AFM) and ultraviolet-visible (UV-vis) spectroscopy. Enhancement of rod-like conformation of chains in the films with poor solvent, due to coil-to-rod transition, was clearly evident. Such rod-like chains, which are

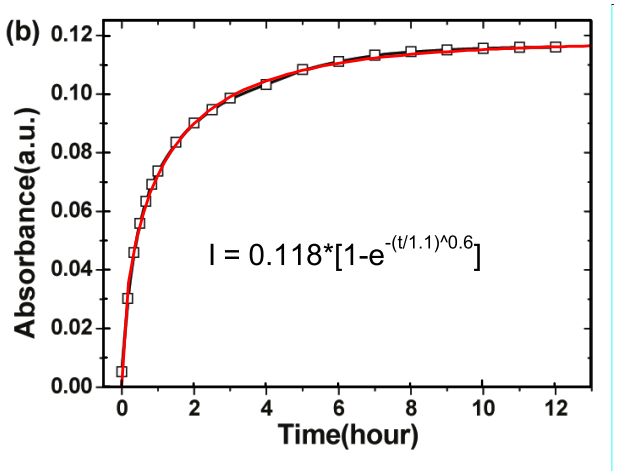

Figure 5.1: Evolution of absorption intensity at 620 nm for P3DDT/CS_2-anisole (1:14, 0.25 mg/mL) aged at room temperature for different times (data reproduced from *J. Phys. Chem. B* **2011**, *115*, 6412). Red curve through the data is simulated considering stretched exponential growth function (as shown inside), with critical growth time $\tau \approx 1.1$ h and stretched exponent $\beta \approx 0.6$. Although there is a large distribution of growth time (as $\beta < 1$), majority of the growth took place within 4 h.

mostly free or random in the as-cast films, are found to organize to form lamellae or crystallites with thermal annealing. Simple XRD mapping helps us to determine the optimum annealing temperature where highly edge-on oriented lamellae of maximum amount and/or size are formed.

5.2 Experiments

Regioregular poly(3-dodecylthiophene) (P3DDT) was purchased from Sigma-Aldrich (average molecular weight: 60,000; regioregularity ≥ 98.5 %) and used as received. Chlorobenzene (CB) and anisole (AN) were obtained from Sigma-Aldrich. P3DDT was first dissolved in CB and then AN was added to that solution such that the concentration of the final solution was 0.25 mg/ml. CB and AN were mixed in the volume ratio 1:4, 1:7 and 1:11. Films were prepared by drop-casting such solutions after about 4 h (as major con-

version took place within that time according to the literature, see Fig. 5.1 [75]) onto solid substrates and through slow evaporation (by keeping inside petri-dishes). Films deposited on Si substrates from three solutions are referred to as 1:4 CB-AN, 1:7 CB-AN and 1:11 CB-AN. To check the effect of the nature of the Si surface on the film-structure, films were deposited on differently passivated [OH- and H-] and oriented [(001) and (111)] Si substrates. OH- and H-passivated Si substrates were prepared through pretreatment as mentioned in Chapter 3. To compare the effect of mixed solvent with respect to single CB solvent, films were also prepared on Si substrates from solution of P3DDT in CB solvent. For optical studies, 1:11 CB-AN films were deposited on clean quartz glass substrates. Annealing of the films at different temperatures were done by placing the samples covered in glass petri-dishes in a box furnace. Annealing at different temperatures was done mostly on different films. For comparison, a single 1:11 CB-AN film deposited on a glass substrate was also annealed at different temperatures.

XRD measurements of the films were performed on the Versatile X-ray Diffractometer (VXRD) setup described in Chapter 3. Initially, conventional XRD measurements (θ-2θ) were carried out for the as-cast, 60°C and 165°C annealed 1:4 CB-AN, 1:7 CB-AN and 1:11 CB-AN films and also for the films deposited on glass substrates and annealed at different temperatures. Later, rocking (θ) scans around the intense Bragg peak ($2\theta_B$) were carried out for one set of mixed solvent (1:11 CB-AN) films and one set of single solvent (CB) films, annealed at different temperatures. Subsequently, XRD measurements for different offset angles $\Delta\theta$ with respect to the peak position (θ_P) of the rocking curve, were also carried out for those samples.

GISAXS measurements of the as-cast, 60°C and 165°C annealed 1:4 CB-AN, 1:7 CB-AN and 1:11 CB-AN films were carried out using the synchrotron source at P03 beam line, PETRA III, the details of which are given in Chapter 3. The sample-to-detector distances

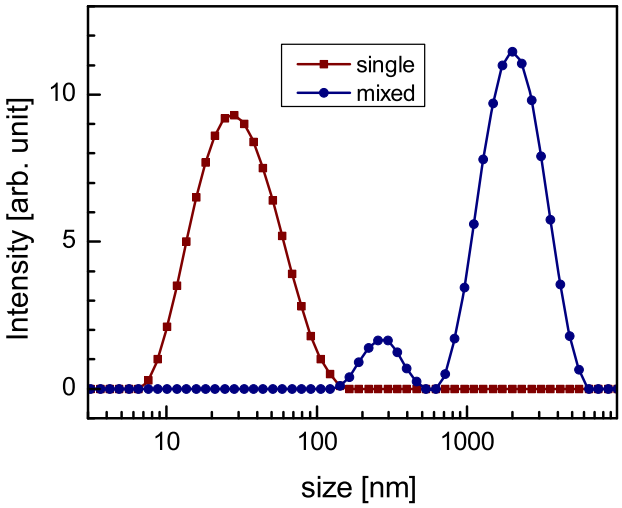

Figure 5.2: Intensity particle size distribution curves, obtained from the DLS measurements, for the solutions of P3DDT in single (CB) and mixed (CB-AN) solvents, collected after 4 h of mixing.

for the as-cast and annealed samples were 1005 and 1721 mm, respectively. For data collection, the incident angle α was kept at 0.4° and 0.25° for the as-cast and annealed samples, respectively. The direct beam was stopped and the specular reflected beam was attenuated by two separate point-like beam stops to avoid the saturation of the detector.

The top surface morphology of the as-cast, 130°C and 165°C annealed 1:11 CB-AN P3DDT films on Si substrates were mapped through AFM (beam deflection AFM, Omicron NanoTechnology) in different length scales ($0.2-7$ μm). AFM images were collected in noncontact mode and in UHV ($\sim 10^{-10}$ mbar) conditions. Optical absorption spectra of the 1:11 CB-AN P3DDT films on quartz substrates, after annealing at different temperatures, were collected using an UV-vis spectrophotometer (Perkin Elmer, Lambda 750). For comparison, UV-vis spectra of P3DDT solutions, prepared using single (CB) and mixed (CB-AN) solvents, were also collected. For the estimation of the size and/or conformation/structure of P3DDT molecules/aggregates, dynamic light scattering (DLS) measure-

ments (Zetasizer Nano-S, Malvern Instrument) were performed for such solutions.

Intensity particle size distribution curves, obtained from the DLS measurements, for the solutions of P3DDT in single (CB) and mixed (CB-AN) solvents, collected after 4 h of mixing, are shown in Fig. 5.2. Single peak is observed in the curve for the single solution, while two peaks are observed in the curve for the mixed solution. The size obtained from the single solution is about 27 nm, which can be attributed to the average hydrodynamic diameter of the P3DDT chains when they are in coil-like configuration. The sizes obtained for the mixed solution are about 270 and 2000 nm. The first one can be attributed to the average hydrodynamic diameter of the P3DDT molecules, when chains are in rod-like configuration, while the second one probably corresponds to the size of the aggregates.

5.3 Results and discussion

5.3.1 Optimizing the ratio of solvents

In this section, we discuss the influence of poor solvent on the structures (i.e., amount, size and orientation of the crystallites) of P3DDT films without and with thermal annealing, as observed from the conventional XRD and GISAXS measurements, in order to find out the optimum good-to-poor solvent ratio. Thermal annealing were carried out at 60 and 165°C, which are above the two endothermic peaks, observed from DSC thermogram of P3DDT powder (shown in Figure 5.3), corresponding to the melting of the alkyl side chains and polythiophene backbones, respectively [76, 154].

XRD data of the 1:4, 1:7 and 1:11 CB-AN samples are shown in Figure 5.4. Peak around 3.3°, corresponding to the separation (d) between alternate layers of polythiophene backbones along alkyl side chains is observed in all the curves, indicating the presence

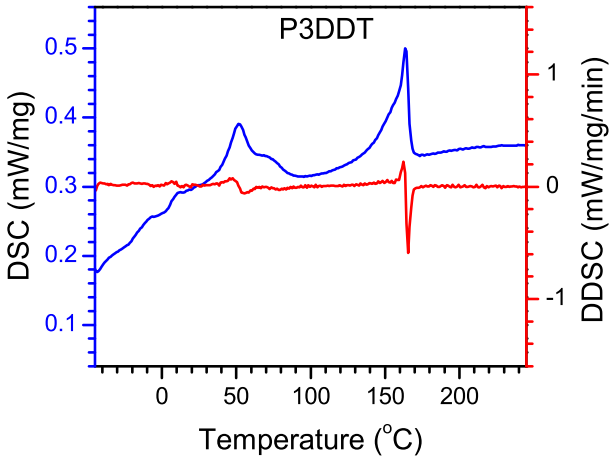

Figure 5.3: Differential-scanning calorimetry (DSC) thermogram (and its derivative) of the powder P3DDT showing two sharp endothermic peaks around 53 and 163°C.

of small crystallites of P3DDT molecules with predominantly edge-on orientations. The position, width and intensity of the peak, however, varies, indicating changes in the d-spacing, size and amount of crystallites. For the as-cast films the position is almost same but the intensity increases slightly with the increase in the proportion of the poor solvent. On annealing the films at 60°C there is almost no change (apart from very slight shift in the position of the peak towards lower 2θ) in the XRD curves (not shown here). Annealing the films at 165°C results in a huge increase in the peak-intensity and a slight shift in the peak-position towards lower 2θ. For the 1:11 CB-AN sample, the change in the intensity is maximum, while that in the position is minimum. Similar nature of XRD patterns (Fig. 5.5) is observed for the films deposited on the Si substrates with different passivations and orientations [such as OH-Si(111), H-Si(111) or H-Si(001)] and thus needs no separate discussion.

To get the quantitative information about the crystallinity of the films, each XRD data around the peak is fitted with a single or double Gaussian peak(s) along with an exponentially decreasing background. Bragg peaks for the as-cast films and the 165°C annealed

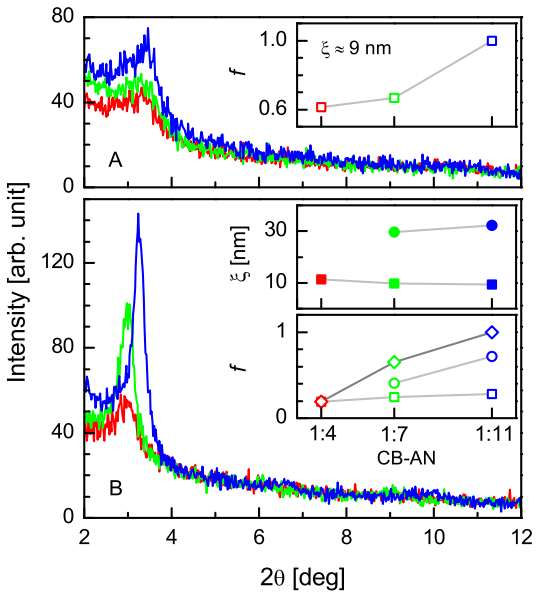

Figure 5.4: XRD data (red, green and blue) of the as-cast (A) and 165°C annealed (B) 1:4, 1:7 and 1:11 CB-AN P3DDT films, showing Bragg peak due to the alternate layers of polythiophene backbones and alkyl side chains. Insets: corresponding variation of crystallite size (ξ) and their relative amount (f) with solvent ratio.

1:4 CB-AN film are well fitted with a single Gaussian peak, while those for the 165°C annealed 1:7 and 1:11 CB-AN films are fitted with two Gaussian peaks. The width of the Gaussian peak is used to estimate the crystallite size (ξ) using standard Scherrer's formula,

$$\xi = \frac{C\lambda}{\beta \cos\theta_B},$$

Table 5.1: Parameters such as d-value, size (ξ) and normalized amount (f) of the P3DDT crystallites in the as-cast and annealed films prepared from different ratio of good to poor solvents.

Sample	As-cast			165°C annealed					
	d-value (nm)	ξ (nm)	f	d-value (nm)	ξ_1 (nm)	ξ_2 (nm)	f_1	f_2	f
1:4 CB-AN	2.66	9	0.6	2.98	11	-	0.2	-	0.2
1:7 CB-AN	2.66	9	0.7	2.96	10	30	0.2	0.4	0.6
1:11 CB-AN	2.65	9	1.0	2.72	9	32	0.3	0.7	1.0

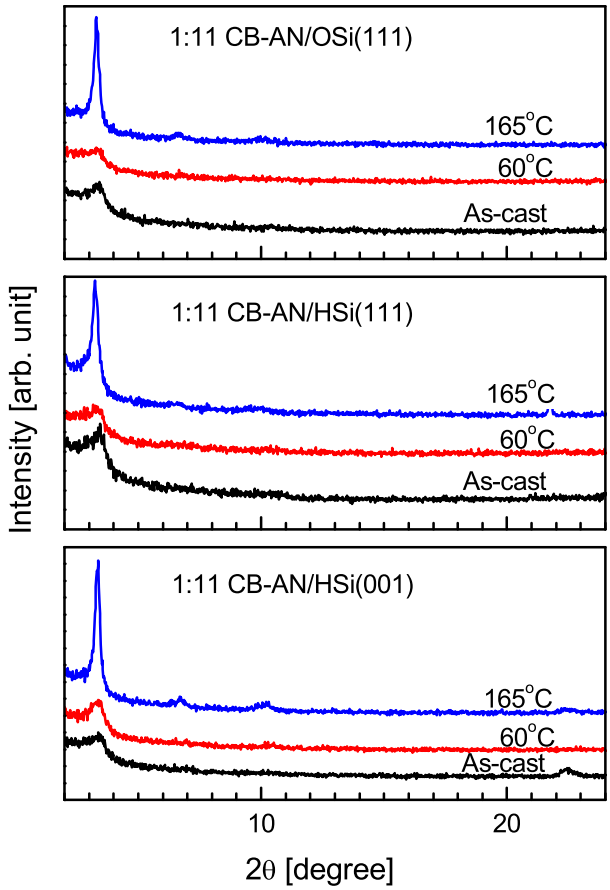

Figure 5.5: XRD data of the as-cast and thermal annealed 1:11 CB-AN P3DDT films deposited on the differently passivated and orientated Si substrates.

where C is a dimensionless Scherrer constant which depends on the shape of the crystallites, the (hkl) index of the diffraction peak and the instrumental factor and whose value is taken to be 0.9, λ is the wavelength of the X-ray, β is the full width at half maxima (FWHM in radian) and θ_B is the Bragg angle. The d-values estimated from the XRD peak positions are tabulated in Table 5.1. The crystallite size and their normalized amount, estimated from the width and intensity of Gaussian peak(s), are plotted in the insets of Figure 5.4 and also tabulated in Table 5.1. It is clear from the figure and the table that for the as-cast films, very small (about 9 nm) crystallites having d-value of 2.66 nm, are formed. The normalized

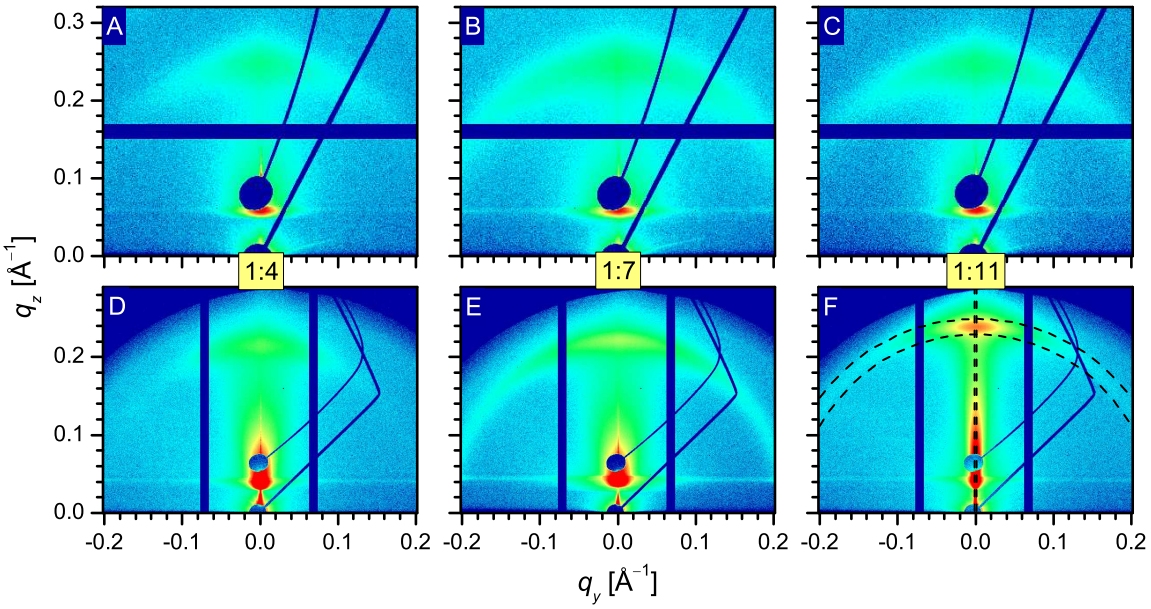

Figure 5.6: GISAXS patterns of the as-cast (A, B and C) and 165°C annealed (D, E and F) 1:4, 1:7 and 1:11 CB-AN P3DDT films, showing Bragg arc corresponding to the alternate layers of polythiophene backbones and alkyl side chains.

amount of crystallites increases with the proportion of poor solvent from 0.6 to 1.0. For the 165°C annealed films the crystallites' size and/or amount increases appreciably with the proportion of poor solvent. Relatively large (about 30 nm) crystallites are also formed for the 1:7 and 1:11 CB-AN films, the amount of which is found to be maximum for the latter. The d-value is also found to increase with thermal annealing, the change being minimum for the 1:11 CB-AN films.

GISAXS patterns of the as-cast and 165°C annealed films are shown in Figure 5.6. Presence of Bragg arc corresponding to the separation between alternate layers of polythiophene backbones along alkyl side chains is clearly visible in all the patterns. The arc nature suggests that the predominantly edge-on oriented lamellae have some deviations as well, because otherwise the GISAXS pattern should have shown a Bragg spot instead of an arc. There is very little variation in the GISAXS patterns of the as-cast films. The nature

remains almost same for the 60°C annealed films (not shown here), while for the 165°C annealed films the Bragg arc intensity increases, which is small for 1:4 CB-AN film but large for 1:11 CB-AN film. To have a better idea about the film structure, GISAXS line profiles along q_z and q_y directions are generated from vertical cut and horizontal arc, respectively, through the Bragg spot (as shown in Figure 5.6) and are plotted in Figure 5.7. The GISAXS line profiles along q_z direction (Figure 5.7 A and C) exactly follow the XRD data (Figure 5.4), and hence, provide the same information about the crystallites. The GISAXS line profiles along q_y direction provide additional information about the orientation of the crystallites. Considering Gaussian distribution, the angular spread in the orientation of the crystallites with respect to the perfect edge-on orientation is estimated from the FWHM. For the as-cast films, the crystallites are found within the angular spread of $\pm 20^{\circ}$, with slightly enhanced probability within $\pm 5^{\circ}$. For the 165°C annealed films, the angular spread decreases, which is minimum for the 1:11 CB-AN film. For this film, the crystallites are found within the angular spread of $\pm 12^{\circ}$, with strongly enhanced probability within $\pm 5^{\circ}$.

It is clear from both XRD and GISAXS results that there is a huge difference in the crystallinity between films cast from different solutions for the 165°C annealed films, although very little difference is observed for the as-cast films. This apparently anomalous behavior can be explained considering the well known two step process, namely coil-to-rod transformation of the polymers and subsequent organization of the rods to form crystallites. The coil-to-rod transformation is enhanced with the increase in the proportion of poor solvent, while the subsequent organization of the rods to form nearly edge-on oriented lamellae are enhanced with the increase in the temperature. At room temperature, very few rods probably organize to form some small (about 9 nm) sized crystallites, which we can detect. At higher temperatures, the organization is enhanced, thereby increasing the amount and size of the crystallites. However, the initial number of rods, which act as nuclei, restrict

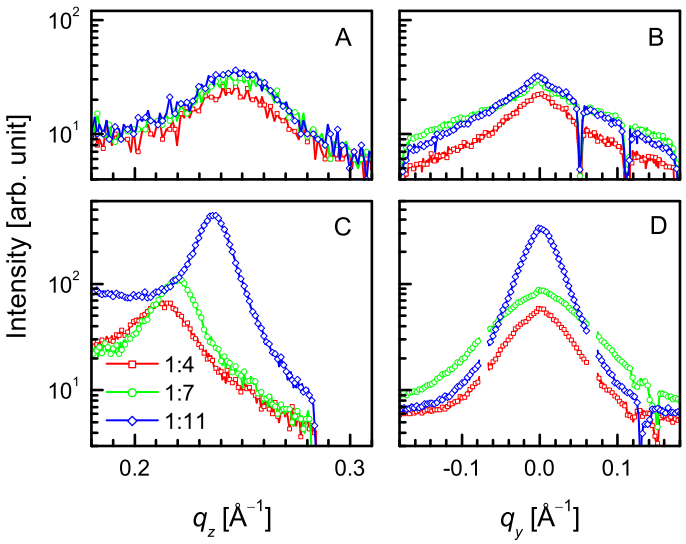

Figure 5.7: GISAXS line profiles along q_z (i.e., vertical cut through Bragg spot) and q_y (i.e., horizontal arc through Bragg spot) of the as-cast (A and B) and 165°C annealed (C and D) 1:4, 1:7 and 1:11 CB-AN P3DDT films.

the amount and size of the crystallites. Accordingly, few small (about 11 nm) crystallites are found in the 1:4 CB-AN annealed film, while many large (about 32 nm) crystallites are found in the 1:11 CB-AN annealed film.

5.3.2 Optimizing the annealing temperature

In this section the influence of annealing temperature on the structure (i.e., amount, size and orientation of the crystallites) of the 1:11 CB-AN (optimum mixing ratio) film, as observed from detailed XRD study, is elaborated, and compared with the single solvent (CB) film, to find out the optimum annealing temperature.

XRD maps of the 1:11 CB-AN samples, collected after annealing at different temperatures, are shown in Figure 5.8. Strong evolution of the Bragg peak, corresponding to alternate layers of polythiophene backbones and alkyl side chains, is observed with increase in the annealing temperature. The peak-intensity increases with temperature upto

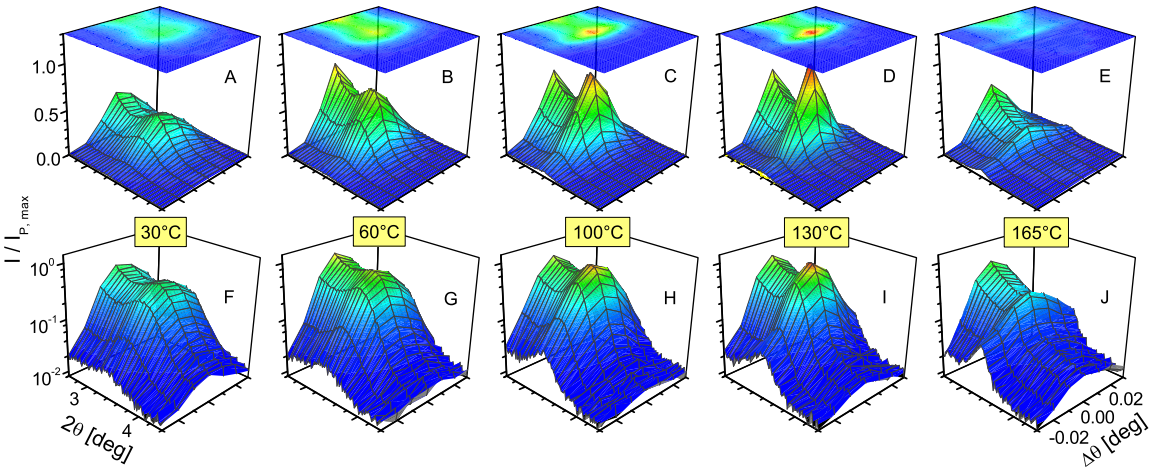

Figure 5.8: XRD maps of the 1:11 CB-AN P3DDT films, after annealing at different temperatures, showing evolution of Bragg peak, corresponding to the alternate layers of polythiophene backbones and alkyl side chains, in three modes of presentation.

130°C and then decreases. However, the peak-intensity in directions other than the perfect edge-on direction (clearly visible from 3D log scale presentation) increases gradually.

To have a better idea about the film structure, XRD profiles along specular ($\Delta\theta \approx 0$) and off-specular ($\Delta\theta \approx 0.03°$) directions and rocking curves (around $2\theta \approx 3.4°$) for the as-cast, 130°C and 165°C annealed mixed solvent samples are plotted in Figure 5.9. XRD profiles and rocking curves for the as-cast, 130°C and 165°C annealed single solvent samples are also plotted in Figure 5.9 for comparison. Strong difference is observed between mixed and single solvent as-cast films. The peaks that are present in the XRD curves for the mixed solvent film, both along specular and off-specular directions are almost absent or broad for the single solvent film. The nature of change in the structure of the film with annealing is similar for both films. However, the amount of change is different. Also, the broad hump is still present around the peak in the single solvent film after annealing.

To get detailed quantitative information about the crystallinity of the films, each XRD curve around the peak is fitted with a single or double Gaussian peak(s) along with an ex-

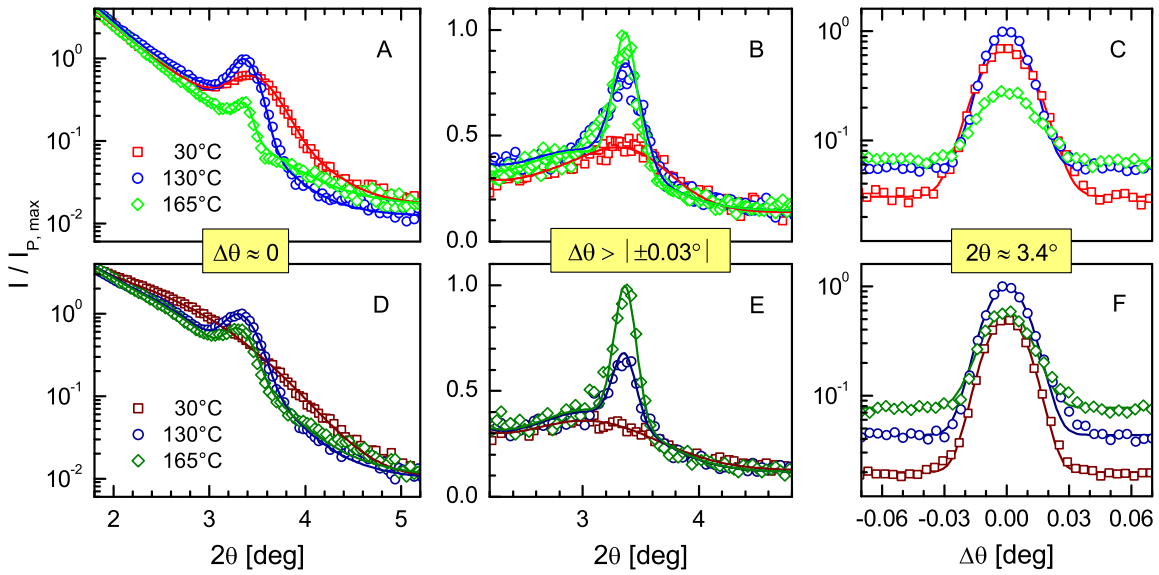

Figure 5.9: XRD profiles (along specular, $\Delta\theta \approx 0$ and off-specular, $\Delta\theta \approx 0.03^{\circ}$ directions) and rocking curves (around $2\theta \approx 3.4^{\circ}$) for the as-cast, 130°C and 165°C annealed P3DDT films. A, B and C for mixed solvent (1:11 CB-AN) films; D, E and F for single solvent (CB) films.

ponentially decreasing background, as before. The variation in the size of the crystallites and its amount with annealing temperature along specular and off-specular directions for the mixed and single solvent films are shown in Figure 5.10. The increase in the size of the crystallites with the annealing temperature is clearly visible. For the mixed solvent film, crystallites of two different sizes are observed. Along specular direction, 6 nm and 15 nm

Table 5.2: Parameters such as relatively large size of crystallites (ξ) and its normalized amount (f) along specular (s) and off-specular (os) directions for the as-cast (30°C), 130°C and 165°C annealed mixed solvent (1:11 CB-AN) and single solvent (CB) P3DDT films.

Annealing temperature	Mixed solvent film				Single solvent film			
	ξ_s (nm)	f_s	ξ_{os} (nm)	f_{os}	ξ_s (nm)	f_s	ξ_{os} (nm)	f_{os}
30°C	15	0.4	10	0.2	-	-	-	-
130°C	28	0.9	26	0.5	21	1.0	34	0.3
165°C	44	0.2	34	0.7	26	0.6	36	0.7

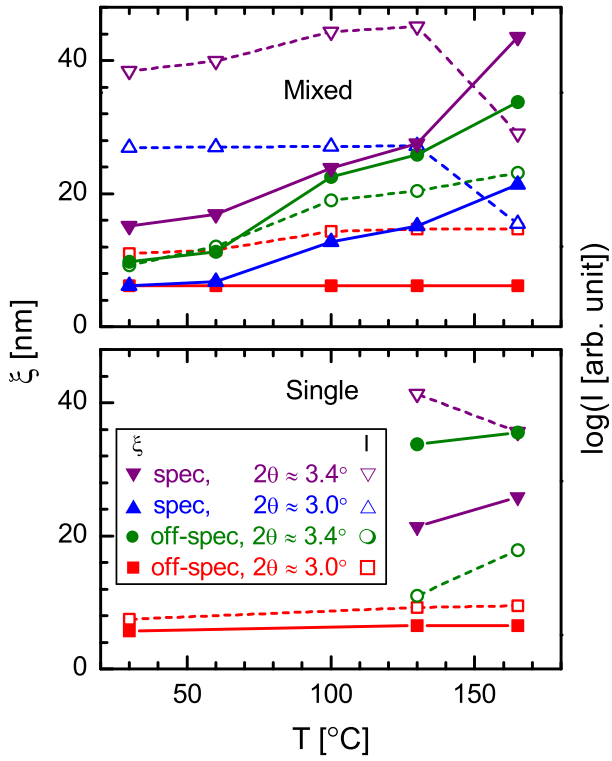

Figure 5.10: Variation of the crystallite-size (ξ) and its intensity (I) with annealing temperature along specular and off-specular directions for the mixed and single solvent films.

sized crystallites for the as-cast film increase gradually in size to 20 nm and 44 nm, respectively, on annealing, while along off-specular direction, 6 nm sized crystallites for the as-cast film remain almost same in size and 10 nm sized crystallites increase gradually to 34 nm on annealing. The intensity or amount of such nanocrystallites along specular direction, which is quite high initially, further increases (or remains almost same) up to 130°C annealing temperature and then decreases considerably, while that along off-specular direction, which is quite low initially, increases gradually with annealing temperature. It can be noted that the XRD and GISAXS results for the different mixed solvent films presented before is somewhat an average of the results along specular and off-specular directions, as expected. As for the XRD measurements of the different mixed solvent films, no special alignments

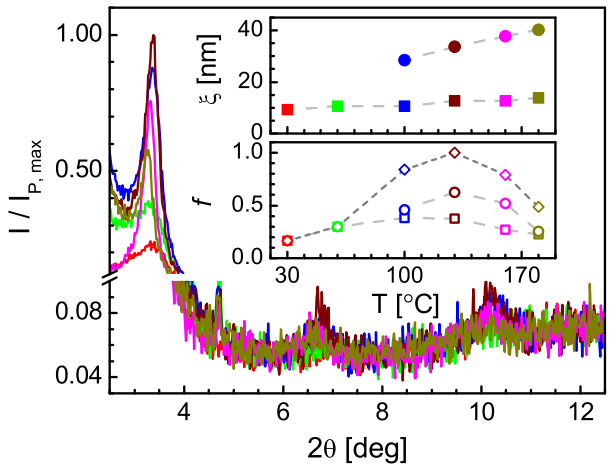

Figure 5.11: XRD curves of a 1:11 CB-AN P3DDT film on quartz glass, after annealing it at different temperatures, showing evolution of Bragg peak, corresponding to the alternate layers of polythiophene backbones and alkyl side chains. Insets: corresponding variation of crystallite size (ξ) and their relative amount (f) with annealing temperature.

have been made, which is required for the estimation along specular direction. Also for the GISAXS measurements, the Bragg peak at $q_y = 0$ has some non-zero q_x component (as the incident angle is $\leq 0.4^\circ$ and the exit angle is $\geq 1.6^\circ$ for $2\theta_B \approx 2^\circ$). For the as-cast single solvent film, no crystallite is observed initially along specular direction, while very low intensity, very small (about 6 nm) crystallites are observed along off-specular direction. On annealing the film, about 20-25 nm sized crystallites are formed along specular direction, while about 35 nm sized crystallites are formed additionally along off-specular direction. The intensity along specular direction is quite high compared to the off-specular direction. Also the intensity along specular direction is maximum around 130°C, while that along off-specular direction increases gradually, similar to the mixed solvent film. Relatively large size of crystallites and their normalized amounts along specular and off-specular directions for the as-cast, 130°C and 165°C annealed mixed and single solvent P3DDT films are also tabulated in Table 5.2.

So far we have used different films for annealing at different temperatures to understand

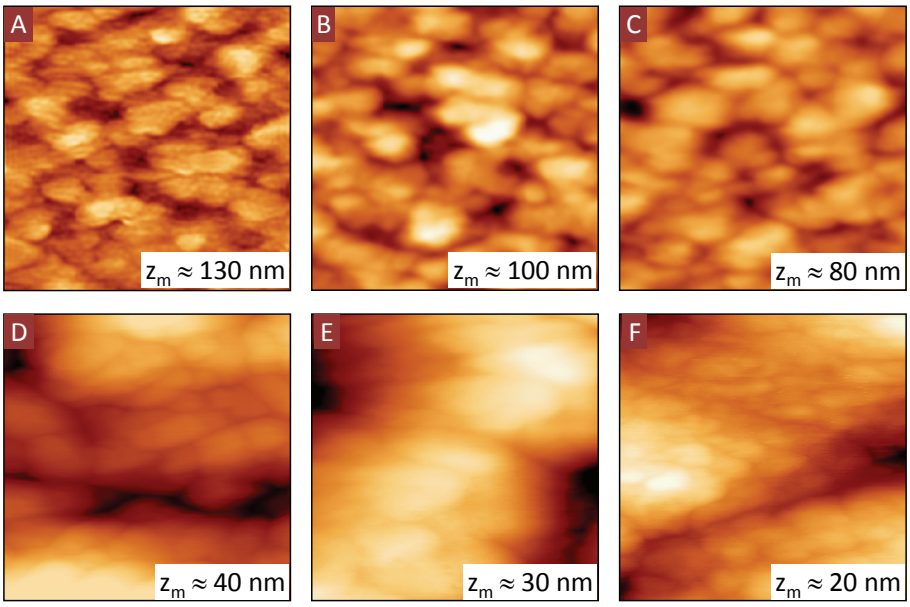

Figure 5.12: Typical AFM images in two length scales (A, B and C for scan size: 5 μm $\times$ 5 μm and D, E and F for scan size: 0.5 μm $\times$ 0.5 μm) showing topography of the as-cast (A and D), 130°C (B and E) and 165°C (C and F) annealed 1:11 CB-AN P3DDT films. z_m indicates maximum height variation.

the structure. We further cross check the results by annealing a single film at different temperatures. For that, XRD data of a 1:11 CB-AN film on quartz glass, collected after annealing it at different temperatures, are plotted in Figure 5.11. The crystallites' size (ξ) and their normalized amount (f), obtained from the peak of each XRD data (as before), are plotted as a function of annealing temperature in the insets of Figure 5.11. Considerable increase in the size of the crystallites is observed for annealing above 100°C, the amount of which increases significantly upto 130°C and then decreases, as before. So, XRD analysis of all P3DDT films clearly suggests that the optimum annealing temperature is around 130°C.

Typical AFM images of the as-cast, 130°C and 165°C annealed 1:11 CB-AN P3DDT films, in two length scales, are shown in Figure 5.12. Island-like structures of the P3DDT

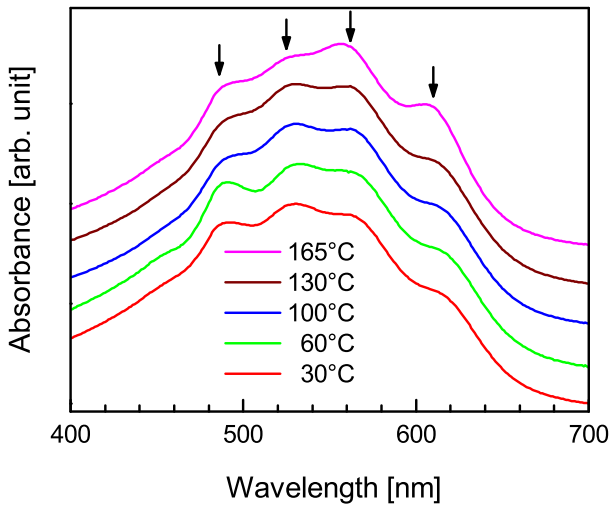

Figure 5.13: UV-vis spectra of the as-cast (30°C) and annealed 1:11 CB-AN P3DDT films deposited on glass substrates. Peak positions are indicated by arrows.

films are evident from large scale (5 μm $\times$ 5 μm) topographic images. The size of islands is found in the range of 0.6-0.8 μm, which remains almost unaffected on annealing. The height of the islands, which is about 130 nm for the as cast film, decreases gradually to about 100 nm for 130°C and to about 80 nm for 165°C annealed films. The island-like structure is, however, composed of small domain-like structures, which are clearly evident from small scale (0.5 μm $\times$ 0.5 μm) topographic images. The size of the domains is about 50 ± 10 nm for the as-cast film, which increase slightly to about 60 ± 10 nm for the 130°C annealed film and then decreases slightly to about about 45 ± 10 nm for the 165°C annealed film. The height of the compact domains can not be resolved from the images, although the maximum height variation (z_m) within the scan size, is found to decrease with annealing temperature.

UV-vis absorption spectra of the 1:11 CB-AN films on quartz glasses, collected after annealing at different temperatures, are shown in Figure 5.13. Four shoulders/peaks at about 490 nm, 530 nm, 560 nm and 610 nm are visible in all the curves. The appearance of

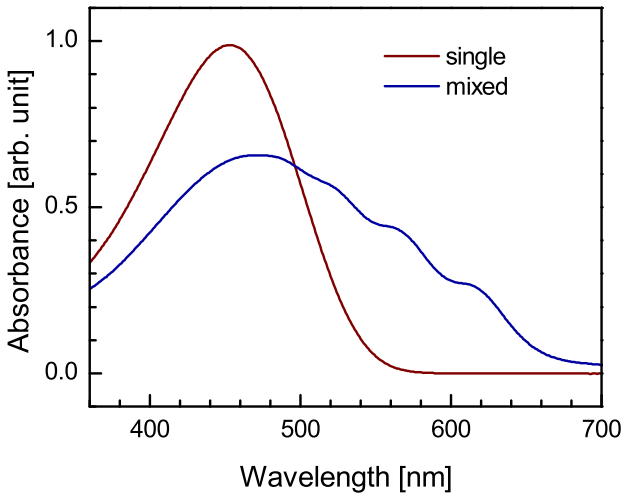

Figure 5.14: UV-vis spectra for the solutions of P3DDT in single (good) and mixed (good-to-poor) solvents, collected after 4 h of mixing.

well-resolved peaks are mainly due to π-π stacking. The absorption peak around 610 nm originates from the interchain π-π transition, while the absorption peaks at 560, 530 and 490 nm are attributed to 0-0, 0-1 and 0-2 transitions of the intrachain exciton. [143] The peak at about 490 nm can also appear due to intrachain π-π transition from planar rod-like conformation of P3AT chains, which is at about 450 nm for the coil-like conformation of P3AT chains comprising twisting and bending of thiophene rings. The observed spectral signatures can also be described using weakly interacting H-aggregates, where the intensity ratio (A_1/A_2) of the peaks at 610 and 560 nm can be used to extract the free exciton bandwidth of the aggregates, which is related to the coupling strength and conjugation length. [144]

The intense peak at round 490 nm for the as-cast film indicates the presence of non-interacting chains in rod-like conformation in large amount. Further increase of that peak for the 60°C annealed film indicates presence of enhanced rod-like chains. The intensity of that peak, however, decreases gradually after annealing above 100°C, suggesting decrease

in the amount of free rod-like chains, due to the ordering of the rod-like chains to form lamellae or H-aggregates, which is evident from the gradual increase in the peak-intensity at around 560 and 610 nm. For the as-cast film and the films annealed upto 130°C, there is very little change in the ratio A_1/A_2, suggesting very little change in the conjugation length. This indicates that the enhancement of lamellae size is predominantly along the alkyl side chain direction. For the film annealed at 165°C, there is a little increase in the ratio and a slight blue shift of the corresponding peaks. Combination of both is probably indicative of some kind of change in the structure or orientation of the lamellae.

To have a better idea about the effect of poor solvent on the structure of P3DDT molecules, UV-vis spectra of the solutions of P3DDT in single (CB) and mixed (CB-AN) solvents, collected after 4 h of mixing, are shown in Fig. 5.14. A single peak near 450 nm is observed in the spectrum of the single solvent solution, indicating the presence of molecules in coil-like conformation. The peak shifted towards higher wavelength suggesting the presence of molecules in predominantly rod-like conformation. Peaks near 530, 560 and 610 nm are also visible in the spectrum of the mixed solution, similar to that of the 1:11 CB-AN films, suggesting formation of some P3DDT aggregates in the solution within 4 h.

5.3.3 Structural analysis

The structures of the P3DDT films deposited from different good-to-poor solvent ratio without heating and subsequent annealing at different temperatures, obtained from the analysis of the complementary data, are shown schematically in Figure 5.15. In general, the P3DDT films are composed of coil-like chains, rod-like chains and lamellar crystallites. For the as-cast 1:4 CB-AN film, coil-like chains are more compared to rod-like chains,

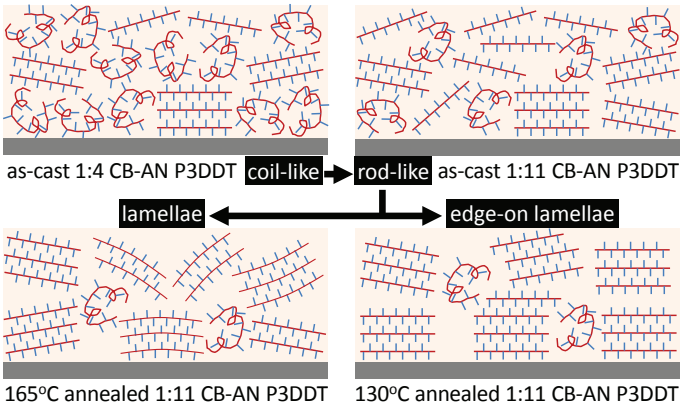

Figure 5.15: Schematic illustration of the structures of the P3DDT films showing enhancement of rod-like conformations with poor solvent (for as-cast films), enhancement of lamellae structures (due to subsequent ordering of such rods) with annealing temperature (for 1:11 CB-AN films) and particular enhancement of edge-on oriented lamellae near 130°C.

while for the as-cast 1:11 CB-AN film, rod-like chains are more compared to coil-like chains. Also, few small sized lamellar crystallites are present in both the films. For the 60°C annealed film, the amount of rod-like chains increases, while that of coil-like chains decreases. For the films annealed above 100°C, the amount of free rod-like chains also decreases, while the amount and size of the crystallites increases. For the 130°C annealed 1:11 CB-AN film, the amount and/or size of the highly edge-on oriented lamellar crystallites are found to be maximum, while for the 165°C annealed film the orientation of the crystallites becomes random.

It is known that P3AT crystallization evolves in two steps, namely, coil-to-rod conformational transition, followed by organization of rod-like chains through strong anisotropic π-π interactions between planar rigid backbones and weak van der Waals interactions between their pendent alkyl side chains [155–157]. In a good solvent, P3DDT dissolves well to form a near equilibrium homogeneous system [75]. Such a solution mostly consists of coil-like polymer chains, which are energetically favorable. Addition of a poor solvent makes the solution inhomogeneous and disturbs the equilibrium. Polymers, which are in

contact with the poor solvent, experience a different polymer-solvent interaction, resulting in a coil-to-rod conformational transition. Consequently, rod conformation increases with the increase in the amount of poor solvent. However, a small number of rods organize to form crystallites in the as-cast films, prepared after aging and normal drying. This indicates that poor solvent mainly induces the unfavorable coil-to-rod conformational transition (negative entropy change) and acts very little on the further unfavorable π-π stacking (which also requires negative entropy change). Thermal annealing seems to be responsible for the π-π stacking. For the present P3DDT polymer, melting of the alkyl side chains takes place in the temperature range 50-80°C, while that of the polythiophene backbones takes place in the temperature range 150-170°C (see Fig. 5.3). Thus annealing above the first temperature range sets the rod-like polymer chains free and helps in the diffusion. Also the thermal energy essentially helps to overcome the unfavorable π-π stacking condition. Increase in the annealing temperature increases the π-π stacking. Organization of the π-π stacked layers through alkyl side chains then initiates to lower the energy. Subsequent cooling predominantly forms edge-on oriented crystallites. Room temperature, on the other hand can only induce limited π-π stacking, hence only small crystallites are observed in the as-cast films. Alkyl side chains in such crystallites are slightly interpenetrating and strained (more like Form-II), which on annealing becomes more relaxed (more like Form-I). Annealing the film near the second temperature range twists and deforms the rod-like polymer chains. Such effect increases with the annealing temperature. Accordingly, more deformed and less edge-on oriented crystallites are formed on subsequent cooling. It is necessary to mention that the thermal energy not only helps to overcome the unfavorable π-π stacking condition but also to overcome the unfavorable coil-to-rod conformational transition. This is clearly evident for the P3DDT films prepared from single solvent, crystallites of which increases with thermal annealing. However, the thermal annealing along with the initial

poor solvent in the mixed solvent films enhances the overall coil-to-rod conformational transition and the amount of crystallites. Such enhancement with thermal annealing is essentially restricted within small-size domains that are formed in the as-cast film (since not much change in the domain size is observed from AFM).

5.4 Conclusions

We have prepared P3DDT films with predominantly edge-on oriented lamellae by a simple drop-casting method from its solutions in mixtures of a good and a poor solvent, namely, chlorobenzene and anisole. The degree of crystallinity can be enhanced by increasing the proportion of poor solvent in the solution. Annealing beyond the melting temperature of the alkyl side chains and below that of the P3DDT backbone brings about an increase in directionality of the lamellae, whereas annealing above the melting temperature of the backbone results in increased crystallinity at the cost of decreased directionality. The XRD data of films cast on H-passivated hydrophobic silicon and oxide covered hydrophilic silicon show similar nature for both as-cast and annealed films. Similar nature is also observed for films cast on H-passivated Si(001) and Si(111). This means that the P3DDT molecules adopt an edge-on orientation irrespective of the nature of the substrate and their behaviour with annealing is also unaffected by the substrate. A combination of XRD and UV-vis measurements clearly shows that the addition of poor solvent in the solution is primarily responsible for the coil-to-rod conformational transition, while organization of the rod-like chains occurs due to subsequent thermal annealing of the film. Annealing beyond the melting temperature of the alkyl side chains helps to form well ordered edge-on oriented P3DDT lamellae structures, which degrades when the melting temperature of polythophene backbone is reached. The optimal annealing temperature for producing well ordered edge-

on oriented P3DDT lamellae turns out to be around 130°C. So the degree of crystallinity and directionality of P3DDT films, which is of immense importance in its performance as a semiconductor, can be regulated by varying the good-to-poor solvent ratio and by choosing the proper temperature for post-deposition annealing.

CHAPTER 6

STRUCTURAL MODIFICATION OF P3DDT FILMS UNDER SOLVENT VAPOR AND THERMAL ANNEALING

6.1 Introduction

The most common method for preparing smooth and uniform polymer films is spin-coating. However, this process suffers from a serious drawback as it involves rapid evaporation of the solvent and does not usually result in an equilibrium structure. The resulting films may have some residual strain and may contain defects. Thermal annealing is well established as an effective way to establish equilibrium and increase the structural order in polymer films, thereby enhancing their device performance. It increases the mobility of the polymer chains, thus enabling them to rearrange into a more ordered structure on slow cooling [158]. However, solvent vapor annealing (SVA) has also emerged as an attractive

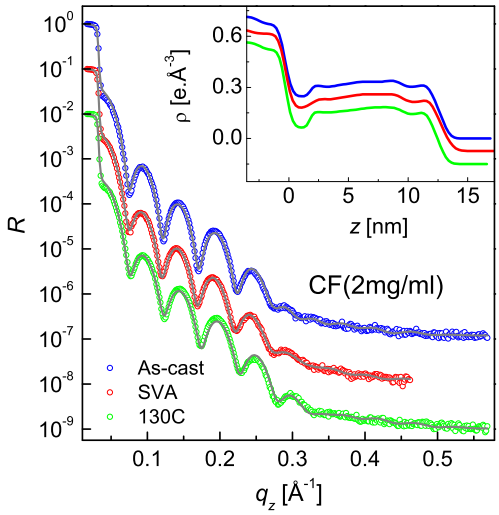

Figure 6.1: XR data showing evolution of a P3DDT-CF/OH-Si film cast from 2 mg/ml CF solution on annealing in CF vapor and subsequent annealing at 130°C. Inset shows analyzed EDPs.

post-deposition technique to form well ordered structures. This method consists in placing the polymer film in an environment saturated with a solvent vapor, resulting in partial re-solubilization of the deposited polymer molecules and their reorganization into structures of higher degree of order than the as-cast film on drying [159]. It has been shown that by swelling a P3HT film to a solution-like state in the vapour of a good solvent and by subsequent controlled deswelling, the nucleation density can be controlled [160]. This results in a considerable improvement in device performance [161]. Interestingly, the orientation of P3AT lamellae on a substrate can also be changed by solvent vapour annealing as shown by Lu and co-workers [162]. Thus we see that the effects of SVA on spin-coated polymer films can be very interesting. With this in view, we have performed SVA of spin-coated P3DDT films in chloroform and toluene environments and investigated the evolution of the films on subsequent annealing and drying. Studies on the time evolution of the thickness

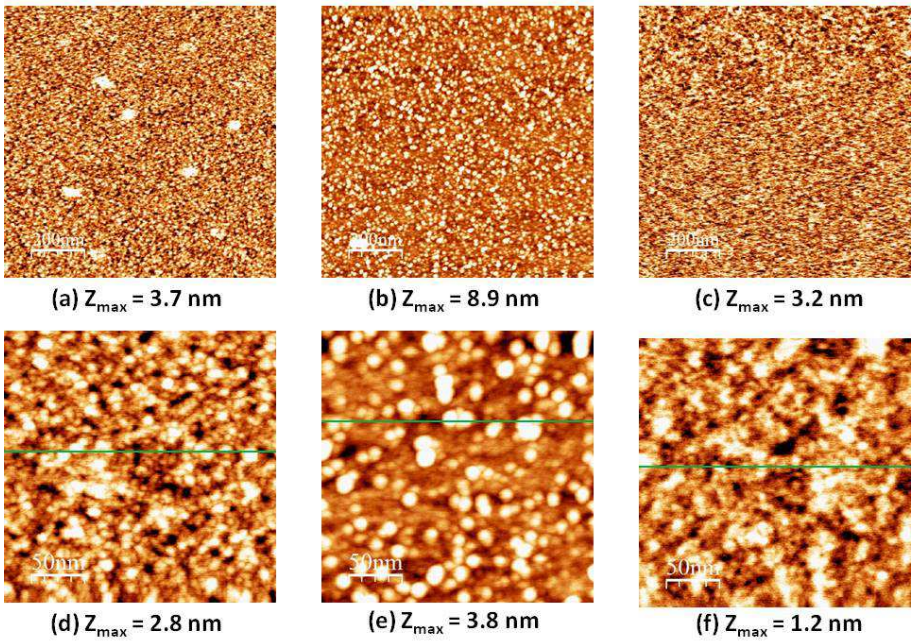

Figure 6.2: Typical AFM images in two length scales (a, b and c for scan size: 1 μm $\times$ 1 μm and d, e and f for scan size: 0.25 μm $\times$ 0.25 μm) showing topography of the as-cast (a and d), solvent vapor annealed (b and e) and 130°C annealed (c and f) P3DDT-CF/OH-Si films cast from 2 mg/ml CF solution. z_{max} indicates maximum height variation.

and roughness of the films during SVA has been carried out at Photon Factory, Japan. Additionally, thermal annealing in presence of a solvent has been observed to produce films with highly enhanced crystalline order.

6.2 Experiments

Regioregular poly(3-dodecylthiophene) (P3DDT) was purchased from Sigma-Aldrich (average molecular weight: 60,000, regioregularity $\geq$ 98.5 %) and used as received. Chloroform (CF, $CHCl_3$) and toluene (TL, C_7H_8) were obtained from Merck. As described in Chapter 4, solutions of P3DDT were prepared by dissolving the polymer in CF and TL sol-

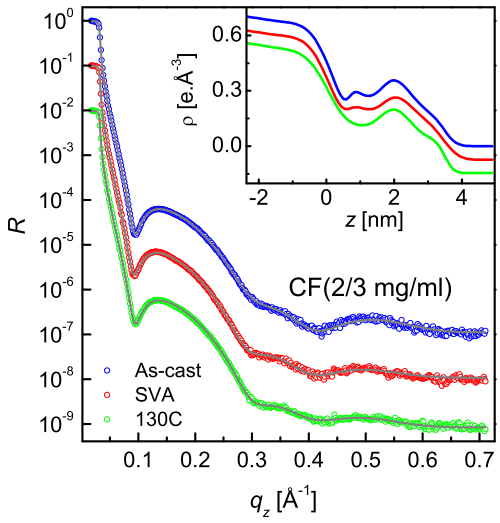

Figure 6.3: XR data showing evolution of a P3DDT-CF/OH-Si film cast from $\frac{2}{3}$ mg/ml CF solution on annealing in CF vapor and subsequent annealing at 130°C. Inset shows analyzed EDPs.

vents with concentrations of 2 mg/ml and $\frac{2}{3}$ mg/ml for CF, and 3 mg/ml and 1 mg/ml for TL. H-Si and OH-Si substrates were prepared by methods described in Chapter 3. Films were then spin-coated on the substrates for 60 s at 3500 rpm for thin films and at 500 rpm for thicker films. For performing solvent vapor annealing, the films were placed inside a covered container and a small beaker containing the solvent was kept beside the film in the same container. Thermal annealing was done in a vacuum oven. Films were characterized using XR and ambient AFM techniques. Power Spectral Densities (PSD) have been calculated from the AFM images to find out the *in-plane* correlation lengths of the samples. For *in-situ* SVA, the film along with a small vessel containing the solvent was kept in a closed cell with kapton windows to allow entry and exit of the X-ray beams.

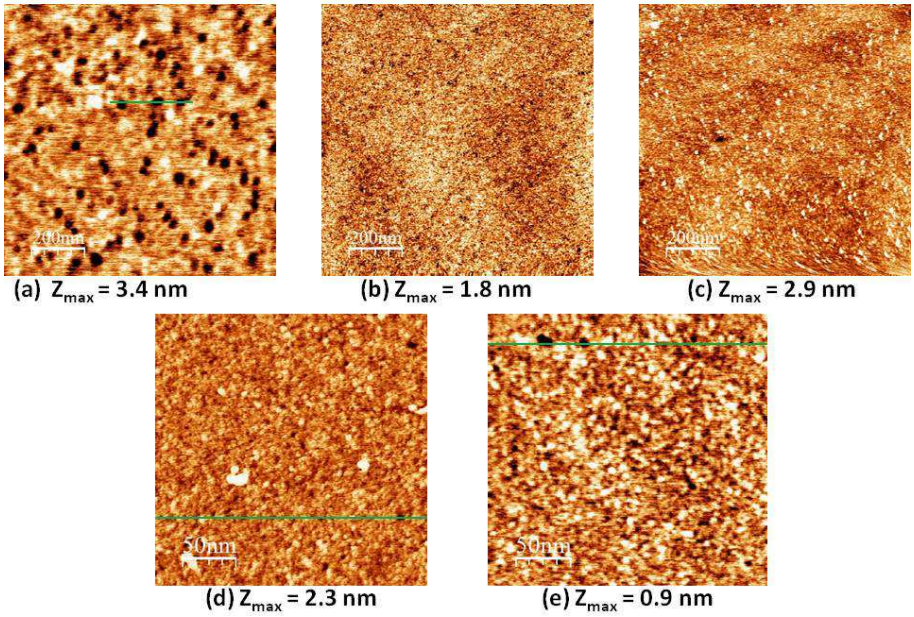

Figure 6.4: Typical AFM images in two length scales (a, b and c for scan size: 1 μm $\times$ 1 μm and d and e for scan size: 0.25 μm $\times$ 0.25 μm) showing topography of the as-cast (a), solvent vapor annealed (b and d) and 130°C annealed (c and e) P3DDT-CF/OH-Si films cast from $\frac{2}{3}$ mg/ml CF solution. z_{max} indicates maximum height variation.

6.3 Results and discussion

6.3.1 Modifications in top and bottom interfaces due to SVA

Fig. 6.1 shows the XR data depicting the evolution of a P3DDT film spin-coated from a 2 mg/ml CF solution on OH-Si due to SVA in CF vapor for 2 hours and subsequent annealing in vacuum for 1 hour. Annealing was performed at 130°C as it is the optimum temperature for producing edge-on oriented lamellae as stated in Chapter 5. It is seen that SVA produces a slight increase in the roughness of the film which is evident from the slightly decreased contrast of the Kiessig fringes. The increase in roughness takes

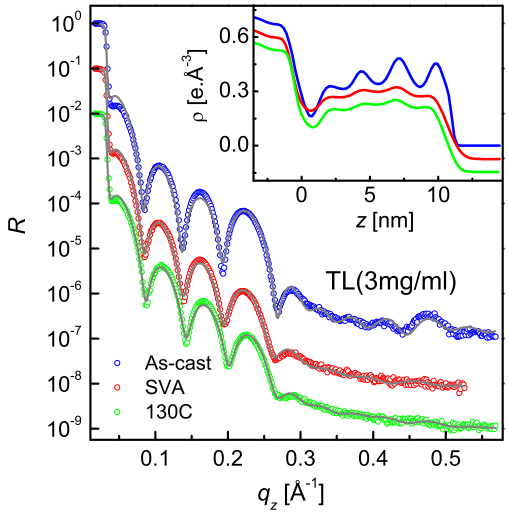

Figure 6.5: XR data showing evolution of a P3DDT-TL/OH-Si film cast from 3 mg/ml TL solution on annealing in TL vapor and subsequent annealing at 130°C. Inset shows analyzed EDPs.

place at both the top and the bottom interfaces, as reflected in the EDP. This increase in roughness is caused by the partial dissolution of the film in the solvent vapor. The change in the top surface morphology is better understood from the AFM images of the as-cast and SVA films as shown in Fig. 6.2. It is seen that the grains present in the as-cast film increase in size due to the uptake of CF molecules, resulting in the increased roughness. On drying the film by annealing at 130°C in vacuum the excess solvent molecules are released from the film, causing a decrease in the thickness and roughness as seen from the XR data and the analyzed EDP. Once again, the decrease in roughness occurs at both the top and the bottom interfaces. The modification of the bottom interface implies better polymer-substrate attachment, whereas the modification of the top interface implies better uniformity of the film. The top surface morphology is shown in the AFM image where it is seen that the height fluctuation of the top surface of the 130°C annealed film is much less

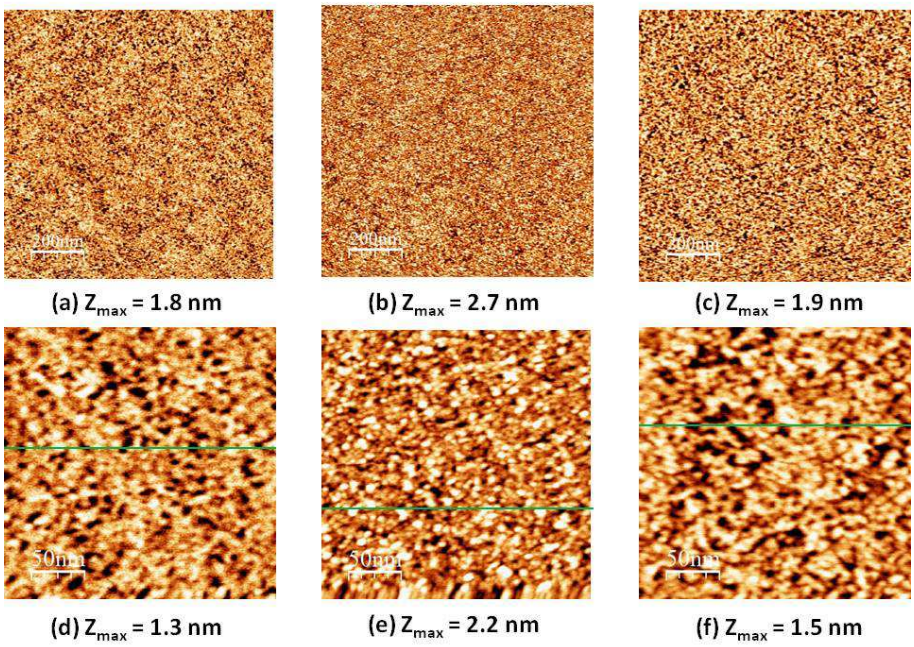

Figure 6.6: Typical AFM images in two length scales (a, b and c for scan size: 1 μm $\times$ 1 μm and d, e and f for scan size: 0.25 μm $\times$ 0.25 μm) showing topography of the as-cast (a and d), solvent vapor annealed (b and e) and 130°C annealed (c and f) P3DDT-TL/OH-Si films cast from 3 mg/ml TL solution. z_{max} indicates maximum height variation.

than that of the as-cast and SVA films, which corroborates the findings from the XR data.

However, thinner films of P3DDT-CF/OH-Si (single layer of P3DDT on the substrate) show a somewhat different behavior on solvent vapor annealing. The XR data and analyzed EDPs for a film cast from $\frac{2}{3}$ mg/ml CF solution (Fig. 6.3) suggest a modification of the film-substrate interface, whereby the irregularity in the electron density near the substrate is smoothed out a little on performing SVA. The EDPs, however, do not suggest much change in the top surface. Nevertheless, AFM images (Fig. 6.4) show that the defects present in the top surface of the as-cast film are greatly reduced on treating the film with solvent vapor. The reason for this change not being reflected by the EDP is probably that the XR data is a statistical average of information obtained from a large area of the sample,

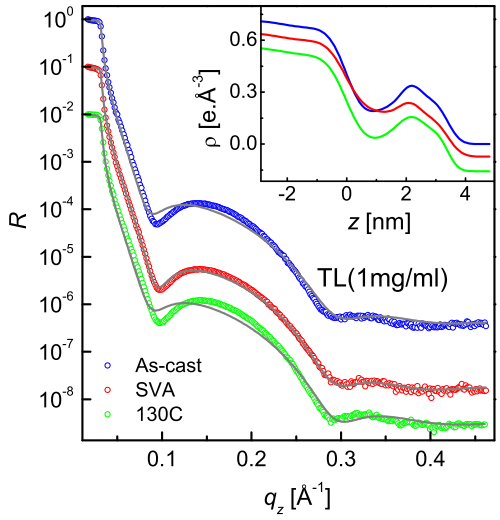

Figure 6.7: XR data showing evolution of a P3DDT-TL/OH-Si film cast from 1 mg/ml TL solution on annealing in TL vapor and subsequent annealing at 130°C. Inset shows analyzed EDPs.

whereas the AFM image gives us information about a microscopic area. Drying the film by annealing causes further smoothing out of the electron density fluctuation at the film-substrate interface as seen from the EDP. On the other hand, the AFM images show the appearance of small clusters on an otherwise smooth surface after drying.

Fig. 6.5 presents the XR data showing the evolution of structure of a P3DDT-TL/O-Si film cast from a 3 mg/ml TL solution. Fig. 6.6 shows the corresponding AFM images. From the XR data and analyzed EDPs it is clear that the crystalline order present in the as-cast film is destroyed due to SVA in TL vapor. The roughness of the two interfaces also increase due to SVA. The increase in roughness of the top surface is also evident from the AFM images which show an increased height fluctuation after SVA is performed. Drying the film results in reduction of thickness due to release of excess solvent molecules from the film. It is interesting to note that the crystalline order is not recovered even after drying

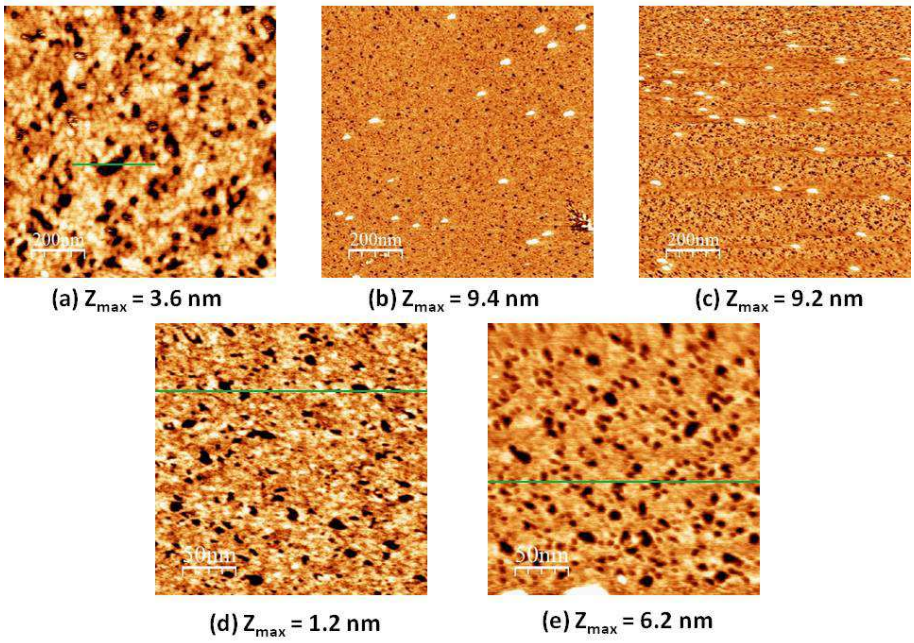

Figure 6.8: Typical AFM images in two length scales (a, b and c for scan size: 1 μm $\times$ 1 μm and d and e for scan size: 0.25 μm $\times$ 0.25 μm) showing topography of the as-cast (a), solvent vapor annealed (b and d) and 130°C annealed (c and e) P3DDT-TL/OH-Si films cast from 1 mg/ml TL solution. z_{max} indicates maximum height variation.

the film. AFM images of the dried film tell us that the top surface morphology of the dried film is similar to that of the as-cast film. So the SVA in TL vapor only induces an *order-to-disorder* transition and not much modification of the interfaces.

In contrast, the XR data and AFM images of the thinner P3DDT film cast from 1mg/ml TL solution (Figs. 6.7 and 6.8) indicate that in this case the solvent vapor is primarily responsible for removing the defects present in the as-cast film, similar to the case of the thin P3DDT-CF/OH-Si film. The EDPs suggest that there occurs an increase in roughness of the film-substrate interface due to SVA, which must have been caused by the partial dissolution of the polymer in TL vapor. AFM images show that the size of the defects in the film is much smaller after treating it with TL vapor. However, a few small islands are

seen to appear after treating the film with TL vapor. In the dried film the roughness of the film-substrate interface is reduced again as seen from the EDP, while the top surface morphology remains almost as it was after SVA.

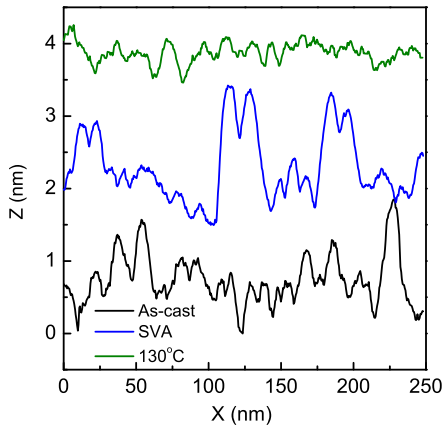

(a) CF (2 mg/ml)

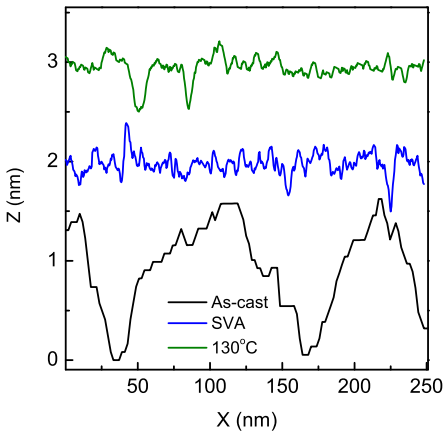

(b) CF ($\frac{2}{3}$ mg/ml)

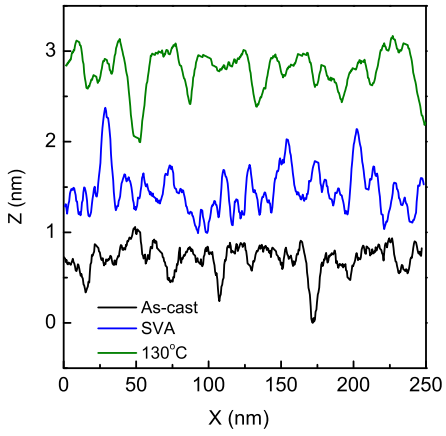

(c) TL(3 mg/ml)

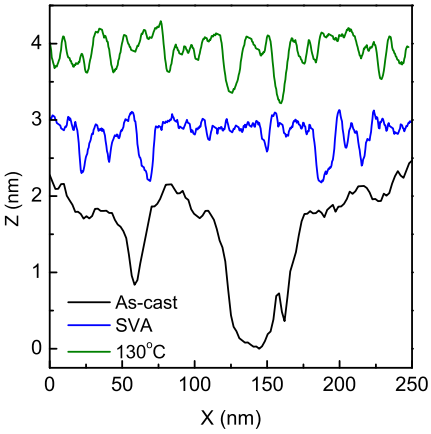

(d) TL(1 mg/ml)

Figure 6.9: Line profiles obtained from AFM images (along the lines shown in the AFM images in Figs. 6.2, 6.4, 6.6 and 6.8) of as-cast, SVA and 130°C annealed films. Graphs have been vertically shifted for clarity.

The information gathered from the AFM images can be better understood by considering the line profiles plotted in Fig. 6.9. It is clearly seen that the height fluctuations in 2 mg/ml CF and 3 mg/ml TL samples increase on annealing in the respective solvent vapors and decrease again on drying the films. On the other hand, the height variations in $\frac{2}{3}$ mg/ml CF and 1 mg/ml TL samples decrease on performing SVA and remain almost intact after drying. Thus, we find that the solvent vapor and thermal annealing process can be effectively used to form films with better uniformity.

In order to quantify the observations from the AFM images, power spectral density (PSD) analysis has been performed. The PSD profiles, obtained from the AFM images, plotted against the spatial frequency k, have been shown in Fig. 6.12. It is seen that in P3DDT films cast from 2 mg/ml CF solution and 3 mg/ml TL solution the PSD does not vary much in the lower frequency region and decreases roughly linearly with frequency in the higher frequency region. The values of k which denote the points of transition from the low frequency to the high frequency behaviour are marked in the figures 6.10a and 6.10c and mentioned in Table 6.1. The value of k at this *shoulder* gives us a correlation length ξ which reflects the average grain size of the film. It is to be noted that this size is not the same as the crystallite size calculated in Chapter 5 because here the grains are composed of both crystalline and amorphous regions which cannot be distinguished by the AFM. The position of the shoulder shifts to lower frequencies with post-deposition treatments in case of the 2 mg/ml CF sample, and hence the correlation length increases. In case of the 3 mg/ml TL sample, however, the position, and hence the correlation length, remains almost unaltered with post-deposition treatments. On the other hand, thinner P3DDT films, cast from $\frac{2}{3}$ mg/ml CF solution and 1 mg/ml TL solution, show striking differences in their PSD profiles after SVA and thermal annealing treatments. All the profiles display a hump-like nature whose central positions have been marked in the figures 6.10b and 6.10d, and

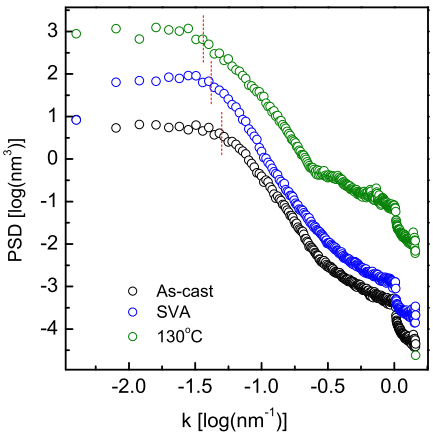

(a) CF (2 mg/ml)

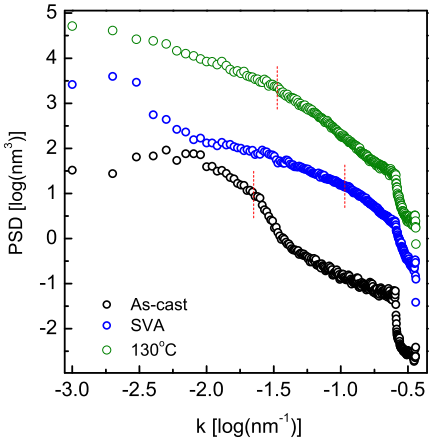

(b) CF ($\frac{2}{3}$ mg/ml)

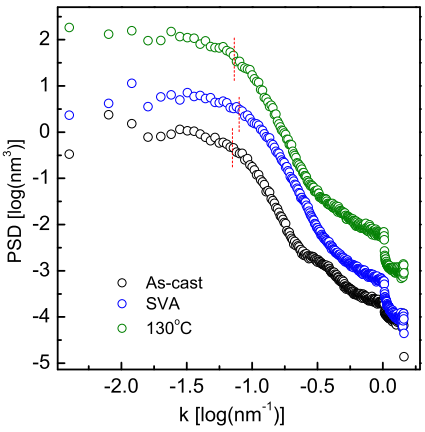

(c) TL(3 mg/ml)

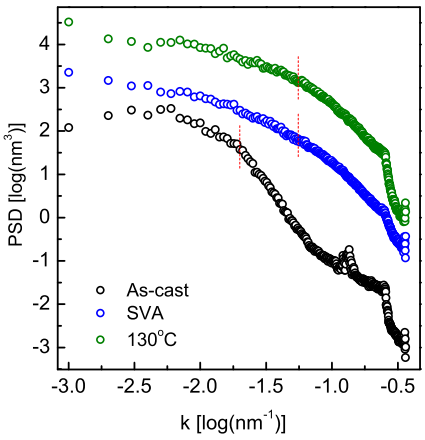

(d) TL(1 mg/ml)

Figure 6.10: PSD profiles calculated from AFM images of as-cast, SVA and 130°C annealed films. Graphs have been vertically shifted for clarity.

also mentioned in Table 6.1. The correlation lengths obtained from the values of k at these positions are also tabulated in Table 6.1. From figures 6.4 and 6.8 it is clear that the decrease in correlation length is related to a decrease in size, and hence an increase in number, of

Table 6.1: Correlation lengths calculated from PSD profiles.

Sample	Concentration [mg/ml]		log(k) [log(nm^{-1})]	ξ [nm]
CF	2	As-cast	-1.30	20
		SVA	-1.38	24
		130°C	-1.44	28
CF	$\frac{2}{3}$	As-cast	-1.65	45
		SVA	-0.94	9
		130°C	-1.46	29
TL	3	As-cast	-1.15	14
		SVA	-1.10	13
		130°C	-1.15	14
TL	1	As-cast	-1.70	50
		SVA	-1.25	18
		130°C	-1.25	18

the defects. For the $\frac{2}{3}$ mg/ml CF sample this correlation length decreases considerably on performing SVA and increases again a little on subsequent thermal annealing. It is to be noted that after thermal annealing the surface morphology consists of both defects and grains. For the 1 mg/ml TL sample too, the correlation length decreases on performing SVA, but remains unchanged even after thermal annealing. The surface of this film mostly contains defects and the grains that appear on SVA and thermal annealing are quite far apart from each other.

6.3.2 Thermal annealing in presence of solvent vapor

Since we have found that 130°C is the optimum annealing temperature for producing highly edge-on oriented P3DDT lamellae, and that exposing a P3DDT film to a solvent vapor helps in reducing the defects present in the as-cast film, we anticipate that introducing a solvent vapor while keeping the film at 130°C might result in a considerable increase in the

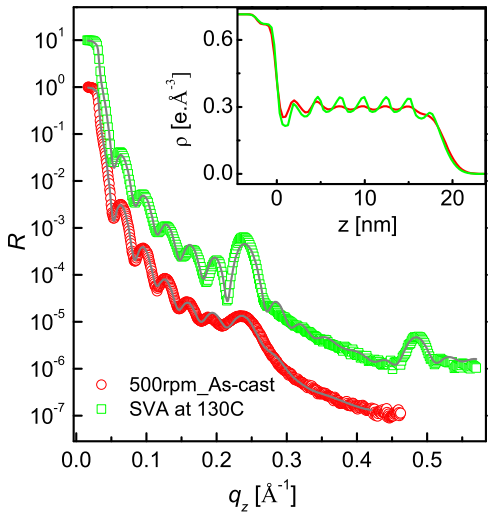

Figure 6.11: XR data showing enhancement of edge-on orientation on SVA at 130°C. Inset shows analyzed EDPs.

edge-on orientation of the molecules, and remove the defects in the film at the same time. In order to study the effect of thermal annealing in presence of a solvent vapor on a P3DDT film prepared from TL solution, we have performed the annealing in a closed chamber in which we kept a vessel containing TL. After initial evacuation the film was allowed to swell in the solvent vapor and heating was carried out simultaneously. Later, the chamber was evacuated again, thus drying the film. XR plots clearly show that this method results in a huge increase in the edge-on orientation in relatively thicker films of P3DDT prepared by spin-coating at 500 rpm (Fig. 6.11). This is evident both from the highly enhanced Bragg peak at ~ 0.22 Å^{-1} and the analyzed EDPs which show an increased contrast in electron density between the thiophene containing layers and the alkyl chain layers after the process.

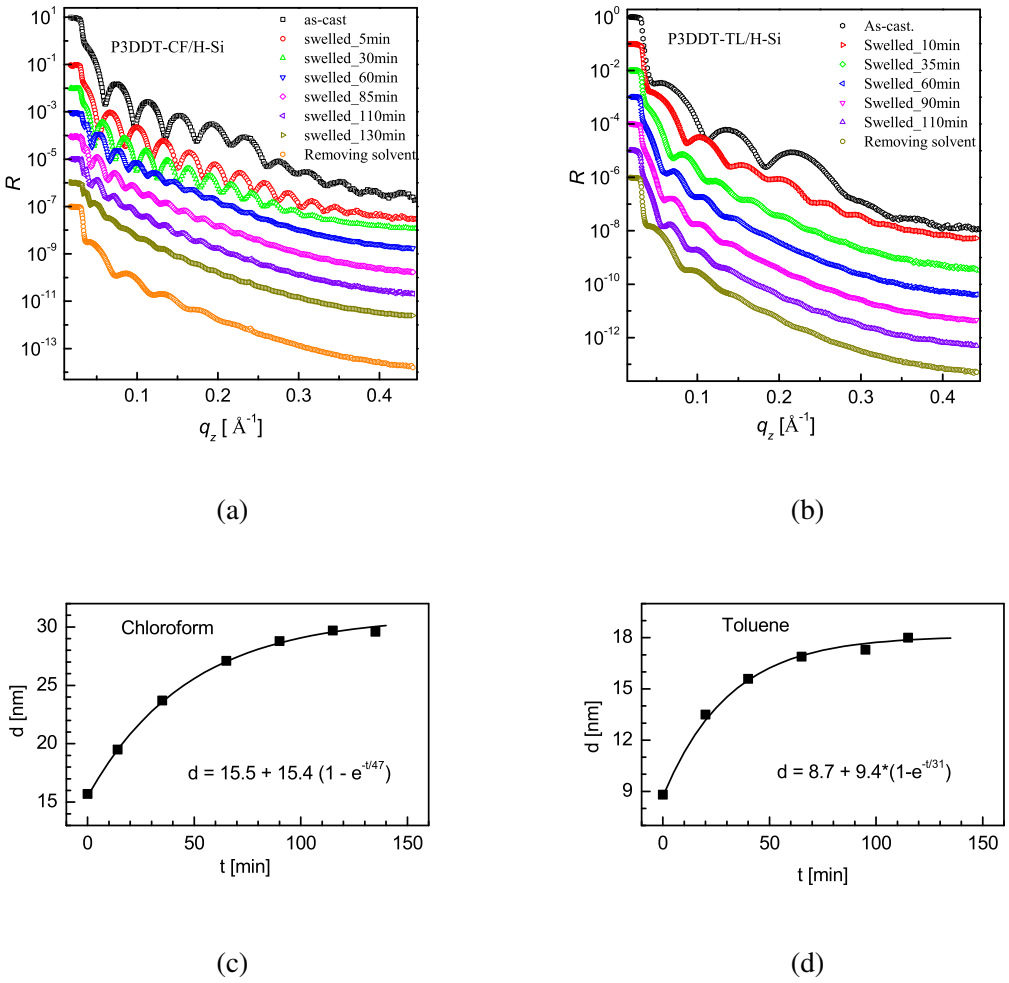

Figure 6.12: Swelling dynamics of P3DDT films: *In-situ* XR data showing time evolution of a (a) P3DDT-CF/H-Si and (b) P3DDT-TL/H-Si film on annealing in CF and TL vapors, respectively, and subsequent removal of the solvent. (c) and (d) show the time evolution of the thickness during SVA in CF and TL vapors, respectively.

6.3.3 *In-situ* study of the evolution of P3DDT films during SVA

Investigations about the time evolution of the thickness and roughness of the P3DDT films during SVA in CF and TL vapors have been carried out with the help of *in-situ* XR. Fig. 6.12a shows the time evolution of the XR profile of a P3DDT-CF/H-Si film due to

SVA in CF vapor. It is seen that in about 2 hours the film becomes mostly dissolved which is clear from the huge increase in thickness and roughness. SVA results not only in swelling of the film, but also in an *order-to-disorder* transition as is evident from the disappearance of the hump near 0.22 $Å^{-1}$ due to layering. Similar studies on a P3DDT-TL/H-Si film using TL vapor show that the *order to disorder* transition takes place in this case too (Fig. 6.12b). It is also observed that the films start drying up as soon as the solvent is removed, which is clear from the decrease in thickness and roughness evident from XR patterns, but complete drying is not possible without vacuum annealing. This explains the absence of any remarkable change in the XR patterns of the films described in Section 6.3.1 after SVA. However, the amount of change in thickness and roughness observed after SVA during *in-situ* XR studies is much more than that observed in Section 6.3.1. This difference is possibly due to the fact that the cell used for *in-situ* studies was smaller than the closed container used in the previous experiments, and hence the vapor pressure was higher in the cell, causing greater amount of change in the same time interval. The change of thickness with time for SVA in CF is plotted in Fig. 6.12c and that for SVA in TL in Fig. 6.12d. It is seen that the thickness varies exponentially with time with a characteristic time of 47 minutes in case of CF and 31 minutes in case of TL. In both the cases the final thickness is about twice the initial thickness of the films. The difference in the swelling dynamics of the films can either be due to the difference in the initial thickness or due to the different casting solvents used.

6.4 Conclusions

In this chapter we have tried to understand the response of spin-cast P3DDT films of different thicknesses to solvent vapor and thermal annealing by using XR and AFM techniques.

It is seen that treating a thin P3DDT film spin-cast from CF solution with CF vapor and subsequently annealing it in vacuum improves the uniformity of the film-air and film-substrate interfaces. On the other hand, SVA in TL vapor and subsequent drying of a P3DDT film cast from TL having well ordered edge-on oriented lamellae result in reduction of the crystalline order of the film. Annealing very thin P3DDT films having a single layer of polymer on the substrate in both CF and TL vapors and subsequent thermal annealing in vacuum result in reduction in the size of the defects in the film-air interface and smoothing out of the electron density fluctuation in the film-substrate interface. Thermal annealing in the presence of a solvent vapor amounts to a huge increase in the edge-on orientation of the film. Thus, it can be concluded that annealing in solvent vapor alone does not improve the edge-on orientation of the polymer and that thermal annealing along with it is essential for this purpose. *In-situ* XR studies of SVA in CF and TL vapors show an exponential increase in thickness with time whereby the film attains a final thickness about twice the initial thickness.

CHAPTER 7

EPILOGUE

7.1 General conclusions

In this section we briefly state the main findings from our studies and mention the inferences that can be drawn from them. The studies on the semicrystalline polymer P3DDT can be classified into the following categories—(i) structural aspects of P3DDT films due to deposition conditions and (ii) evolution of structure due to post-deposition treatments. In what follows we discuss these two points in short.

7.1.1 Structural aspects of P3DDT films due to deposition conditions

P3DDT films have been prepared by two different methods, namely, spin-coating and drop-casting. Spin-coating produces more uniform films, while drop-casting produces films with greater crystalline order, but at the cost of lower uniformity. Using XR technique we have shown that the out-of-plane morphology of spin-cast P3DDT films depend strongly on the properties of the solvent used, the nature of the substrate surface and the spin-coating

speed. In short, lower viscosity and lower evaporation rate of the casting solvent result in better crystalline order of the edge-on oriented lamellae, while higher viscosity and higher evaporation rate lead to depressed crystalline order. The interplay between these two parameters decides the morphology of the film near the substrate and away from it. If the evaporation rate is high the lamellae near the film-air interface have more interpenetrating and less ordered chains. The solubility of the polymer in a given solvent and the substrate surface also play crucial roles in determining the structure of the film. A solvent in which the diffusion of the polymer is low does not offer much freedom to the polymer chains and hence, the pinning effect of the substrate comes into play. For such a combination of solvent and substrate the ordering is weak near the substrate, as in case of toluene and H-Si substrate. The same solvent is capable of producing well ordered lamellae near the substrate if the pinning effect of the substrate is negligible, as we have seen in case of toluene and O-Si substrate.

P3DDT films from solutions in mixed good and poor solvents were formed by drop-casting and slow evaporation of the solvents. XRD, X-ray rocking curves and GISAXS measurements lead us to the conclusion that the addition of a poor solvent is primarily responsible for a *coil-to-rod* transition and that a greater proportion of poor solvent induces the formation of a greater amount of free rod-like chains in the solution. The solutions also contain a few π-stacked aggregates of these rod-like chains. The amount of these aggregates does not depend much on the proportion of the poor solvent. Thermal annealing brings about further π-stacking and as films cast from solutions with higher proportion of poor solvent contain greater amount of free rods, these films contain greater amount of aggregates on annealing. It is also seen that the amount and size of the aggregates do not depend on the nature of the substrate used.

7.1.2 Evolution of structure due to post-deposition treatments

Two types of post-deposition treatments have been performed, namely, thermal annealing and solvent vapor annealing (SVA). It is observed that for spin-coated P3DDT films SVA followed by thermal annealing in vacuum can be used effectively for removing the defects present in the as-cast films and improving the uniformity of the film-air and film-substrate interfaces. However, SVA might lead to a partial loss of crystalline order of the edge-on oriented lamellae. On the other hand, thermal annealing in the presence of a solvent vapor is seen to result in a substantial increase in the crystalline order. During SVA the final thickness achieved by a film due to the uptake of solvent molecules, i.e., when the film becomes mostly dissolved, is about twice the thickness of the as-cast film.

Thermal annealing of drop-cast films formed from mixed solvents leads to the formation of π-stacked aggregates from the free rod-like chains. Annealing above the melting temperature of the alkyl chains and below that of the polymer backbone sets the polymer chains free and thus, on slow cooling these chains can arrange themselves into well ordered edge-on oriented lamellae. In contrast, annealing above the melting temperature of the backbone leads to twisting and bending of the rod-like chains and, on cooling, produces less edge-on oriented lamellae, although the total amount of crystallites increases. It can be inferred that the optimum annealing temperature for producing considerable amount of crystallites with edge-on oriented lamellae is around 130°C.

7.2 Scope for future studies

Although we have encountered several interesting features of semiconducting polymer films in this thesis, a lot more can be done using such polymers. In fact, we have stressed

only on the structural aspects of the films. Obtaining a correlation between the structure and properties of these films will be an interesting option for future research. Using these films in the active layer of field-effect transistors should give us an insight into the dependence of charge carrier mobility on the deposition conditions like solvent, solution concentration and spin-speed, as well as on post-deposition treatments like thermal and solvent vapor annealing.

Attempting to align the polymer nanofibers along a particular direction can be another possible line of progress. A probable way to achieve that can be to deposit P3AT nanofibers, prepared by the mixed solvents method, under the influence of an electric field. The orientation of the nanofibers can be observed using AFM imaging. A large number of fibers oriented in the same direction is expected to give rise to a large mobility in that direction by providing uninterrupted pathways for the charge carriers.

Yet another possibility is to explore the effect of addition of metal nanoparticles on these polymers. Addition of Au nanoparticles have been shown to have considerable influence on the conductivity and photoluminescence properties of P3AT films [163, 164]. It will be interesting to study the influence of Au nanoparticles when they are incorporated into nanofibers of P3ATs. We anticipate that if the Au nanoparticles can be made to attach to the P3AT nanofibers, the fibers may exhibit an increased charge carrier mobility.

We hope that following these lines of investigations will help us exploit the potential of semiconducting polymers to a greater extent and lead to the development of more efficient devices using such polymers.

BIBLIOGRAPHY

[1] C. Reese, M. Roberts, M. mang Ling, and Z. Bao, *Organic thin film transistors*, *Materials Today* **7** (2004) 20–27.

[2] R. L. Carroll and C. B. Gorman, *The genesis of molecular electronics*, *Angewandte Chemie International Edition* **41** (2002) 4378–4400.

[3] L. Qiu, W. H. Lee, X. Wang, J. S. Kim, J. A. Lim, D. Kwak, S. Lee, and K. Cho, *Organic thin-film transistors based on polythiophene nanowires embedded in insulating polymer*, *Adv. Mater.* **21** (2009) 1349–1353.

[4] H. Yan, Z. Chen, Y. Zheng, C. Newman, J. R. Quinn, F. Dotz, M. Kastler, and A. Facchetti, *A high-mobility electron-transporting polymer for printed transistors*, *Nature* **457** (2009) 679–686.

[5] J. H. Burroughes, D. D. C. Bradley, A. R. Brown, R. N. Marks, K. Mackay, R. H. Friend, P. L. Burns, and A. B. Holmes, *Light-emitting diodes based on conjugated polymers*, *Nature* **347** (1990) 539–541.

[6] M. Berggren, O. Inganas, G. Gustafsson, J. Rasmusson, M. R. Andersson, T. Hjertberg, and O. Wennerstrom, *Light-emitting diodes with variable colours from polymer blends*, *Nature* **372** (1994) 444–446.

[7] G. Yu, J. Gao, J. C. Hummelen, F. Wudi, and A. J. Heeger, *Polymer photovoltaic cells: Enhanced efficiencies via a network of internal donor-acceptor heterojunctions*, *Science* **270** (1995) 1789–1791.

[8] Y. Liang, Z. Xu, J. Xia, S.-T. Tsai, Y. Wu, G. Li, C. Ray, and L. Yu, *For the bright future— Bulk heterojunction polymer solar cells with power conversion efficiency of 7.4%*, *Adv. Mater.* **21** (2009) 1349–1353.

[9] P. Leclere, M. Surin, P. Brocorens, M. Cavallini, F. Biscarini, and R. Lazzaroni, *Supramolecular assembly of conjugated polymers: From molecular engineering to solid-state properties*, *Materials Science and Engineering: R: Reports* **55** (2006) 1–56.

[10] F. So, ed., *Organic Electronics: Materials, Processing, Devices and Applications*. CRC: Boca Raton, FL, 2009.

[11] A. Salleo, R. J. Kline, D. M. DeLongchamp, and M. L. Chabinyc, *Microstructural characterization and charge transport in thin films of conjugated polymers*, *Adv. Mater.* **22** (2010) 3812–3838.

[12] X. Guo, M. Baumgarten, and K. Múllen, *Designing π-conjugated polymers for organic electronics*, *Prog. Polym. Sci.* **38** (2013) 1832.

[13] F. Liu, Y. Gu, X. Shen, S. Ferdous, H.-W. Wang, and T. P. Russell, *Characterization of the morphology of solution-processed bulk heterojunction organic photovoltaics*, *Prog. Polym. Sci.* **38** (2013) 1990–2052.

[14] L. Dubois and R. Nuzzo, *Synthesis, structure, and properties of model organic surfaces*, *Annu. Rev. Phys. Chem.* **43** (1992) 437–463.

[15] Y. Wen, Y. Liu, Y. Guo, G. Yu, and W. Hu, *Experimental techniques for the fabrication and characterization of organic thin films for field-effect transistors*, *Chemical Reviews* **111** (2011) 3358–3406.

[16] A. J. Heeger, *Semiconducting and metallic polymers: The fourth generation of polymeric materials*, *J. Phys. Chem. B* **105** (2001) 8475–8491.

[17] G. Strobl, *The Physics of Polymers*. Springer, Berlin, 3 ed., 2006.

[18] H. Wang, Y. Xu, X. Yu, R. Xing, J. Liu, and Y. Han, *Structure and morphology control in thin films of conjugated polymers for an improved charge transport*, *Polymers* **5** (2013) 1272–1324.

[19] F. C. Spano and C. Silva, *H- and J-aggregate behaviour in polymeric semiconductors*, *Annu. Rev. Phys. Chem.* **65** (2014) 477–500.

[20] H. Yamagata and F. C. Spano, *Interplay between intrachain and interchain interactions in semiconducting polymer assemblies: the HJ-aggregate model*, *J. Phys. Chem.* **136** (2012) 184901–1–14.

[21] L. H. Jimison, M. F. Toney, I. McCulloch, M. Heeney, and A. Salleo, *Charge-transport anisotropy due to grain boundaries in directionally crystallized*

thin films of regioregular poly(3-hexylthiophene), *Advanced Materials* **21** (2009) 1568–1572.

[22] Y.-K. Lan and C.-I. Huang, *Charge mobility and transport behavior in the ordered and disordered states of the regioregular poly(3-hexylthiophene)*, *The Journal of Physical Chemistry B* **113** (2009) 14555–14564.

[23] H. Sirringhaus, P. J. Brown, R. H. Friend, M. M. Nielsen, K. Bechgaard, B. M. W. Langeveld-Voss, A. J. H. Spiering, R. A. J. Janssen, E. W. Meijer, P. Herwig, and D. M. de Leeuw, *Two-dimensional charge transport in self-organized, high-mobility conjugated polymers*, *Nature* **401** (1999) 685–688.

[24] G. Schopf and G. Koβmehl, *Polythiophenes–Electrically Conductive Polymers*. Springer, Berlin, 1997.

[25] T. J. Prosa, M. J. Winokur, and R. D. McCullough, *Evidence of a novel side chain structure in regioregular poly(3-alkylthiophenes)*, *Macromolecules* **29** (1996) 3654–3656.

[26] T. Yamamoto, D. Komarudin, M. Arai, B.-L. Lee, H. Suganuma, N. Asakawa, Y. Inoue, K. Kubota, S. Sasaki, T. Fukuda, and H. Matsuda, *Extensive studies on π-Stacking of poly(3-alkylthiophene-2,5-diyl)s and poly(4-alkylthiazole-2,5-diyl)s by optical spectroscopy, NMR analysis, light scattering analysis, and X-ray crystallography*, *Journal of the American Chemical Society* **120** (1998) 2047–2058.

[27] M. Brinkmann, *Structure and morphology control in thin films of regioregular poly(3-hexylthiophene)*, *Journal of Polymer Science Part B: Polymer Physics* **49** (2011) 1218–1233.

[28] S. T. Salammal, E. Mikayelyan, S. Grigorian, U. Pietsch, N. Koenen, U. Scherf, N. Kayunkid, and M. Brinkmann, *Impact of thermal annealing on the semicrystalline nanomorphology of spin-coated thin films of regioregular poly(3-alkylthiophene)s as observed by high-resolution transmission electron microscopy and grazing incidence X-ray diffraction*, *Macromolecules* **45** (2012) 5575–5585.

[29] T. J. Prosa, M. J. Winokur, J. Moulton, P. Smith, and A. J. Heeger, *X-ray structural studies of poly(3-alkylthiophenes): an example of an inverse comb*, *Macromolecules* **25** (1992) 4364–4372.

[30] V. Causin, C. Marega, A. Marigo, L. Valentini, and J. M. Kenny, *Crystallization and melting behavior of poly(3-butylthiophene), poly(3-octylthiophene), and poly(3-dodecylthiophene)*, *Macromolecules* **38** (2005) 409–415.

[31] T. Kawai, M. Nakazono, and K. Yoshino, *Effects of doping on the crystal structure of poly(3-alkylthiophene)*, *J. Mater. Chem.* **2** (1992) 903–906.

[32] K. Tashiro, M. Kobayashi, T. Kawai, and K. Yoshino, *Crystal structural change in poly(3-alkyl thiophene)s induced by iodine doping as studied by an organized combination of X-ray diffraction, infrared/Raman spectroscopy and computer simulation techniques*, *Polymer* **38** (1997) 2867–2879.

[33] M. Leclerc, F. M. Diaz, and G. Wegner, *Structural analysis of poly(3-alkylthiophene)s*, *Macromol. Chem. Phys.* **190** (1989) 3105–3116.

[34] S. Liu and T. Chung, *Crystallization and melting behavior of regioregular poly(3-dodecylthiophene)*, *Polymer* **41** (2000) 2781–2793.

[35] M. C. Gurau, D. M. Delongchamp, B. M. Vogel, E. K. Lin, D. A. Fischer, S. Sambasivan, and L. J. Richter, *Measuring molecular order in poly(3-alkylthiophene) thin films with polarizing spectroscopies*, *Langmuir* **23** (2007) 834–842.

[36] M. A. Ruderer, S. M. Prams, M. Rawolle, Q. Zhong, J. Perlich, S. V. Roth, and P. Müller-Buschbaum, *Influence of annealing and blending of photoactive polymers on their crystalline structure*, *J. Phys. Chem. B* **114** (2010) 15451–15458.

[37] Z. Wu, A. Petzold, T. Henze, T. Thurn-Albrecht, R. H. Lohwasser, M. Sommer, and M. Thelakkat, *Temperature and molecular weight dependent hierarchical equilibrium structures in semiconducting poly(3-hexylthiophene)*, *Macromolecules* **3** (2010) 4646–4653.

[38] R. J. Kline and M. D. McGehee, *Morphology and charge transport in conjugated polymers*, *Journal of Macromolecular Science, Part C: Polymer Reviews* **46** (2006) 27–45.

[39] M. Brinkmann, L. Hartmann, L. Biniek, K. Tremel, and N. Kayunkid, *Orienting semi-conducting π-conjugated polymers*, *Macromol. Rapid Commun.* **35** (2014) 9–26.

[40] W. Porzio, G. Scavia, L. Barba, G. Arrighetti, and S. Milita, *Depth-resolved molecular structure and orientation of polymer thin films by synchrotron X-ray diffraction*, *European Polymer Journal* **47** (2011) 273–283.

[41] D. H. Kim, Y. Jang, Y. D. Park, and K. Cho, *Surface-induced conformational changes in poly(3-hexylthiophene) monolayer films*, *Langmuir* **21** (2005) 3203–3206.

[42] E. Mena-Osteritz, *Superstructures of self-organizing thiophenes*, *Advanced Materials* **14** (2002) 609–616.

[43] K.-Y. Jen, G. G. Miller, and R. L. Elsenbaumer, *Highly conducting, soluble, and environmentally-stable poly(3-alkylthiophenes)*, *J. Chem. Soc., Chem. Commun.* **17** (1986) 1346–1347.

[44] R. Elsenbaumer, K. Jen, and R. Oboodi, *Processible and environmentally stable conducting polymers*, *Synth. Met.* **15** (1986) 169–174.

[45] S. Hotta, S. D. D. V. Rughooputh, A. J. Heeger, and F. Wudl, *Spectroscopic studies of soluble poly(3-alkylthienylenes)*, *Macromolecules* **20** (1987) 212–215.

[46] R. J. Kline, M. D. McGehee, E. N. Kadnikova, J. Liu, and J. M. J. Frechet, *Controlling the field-effect mobility of regioregular polythiophene by changing the molecular weight*, *Adv. Mater.* **15** (2003) 1519–1522.

[47] A. Babel and S. A. Jenekhe, *Alkyl chain length dependence of the field-effect carrier mobility in regioregular poly(3-alkylthiophene)s*, *Synth. Metals* **148** (2005) 169–173.

[48] J.-F. Chang, B. Sun, D. W. Breiby, M. M. Nielsen, T. I. Solling, M. Giles, I. McCulloch, and H. Sirringhaus, *Enhanced mobility of poly(3-hexylthiophene) transistors by spin-coating from high-boiling-point solvents*, *Chem. Mater.* **16** (2004) 4772–4776.

[49] R. J. Kline, M. D. McGehee, and M. F. Toney, *Highly oriented crystals at the buried interface in polythiophene thin-film transistors*, *Nat. Mater.* **5** (2006) 222–228.

[50] S. T. Shabi, S. Grigorian, M. Brinkmann, U. Pietsch, N. Koenen, N. Kayunkid, and U. Scherf, *Enhancement in crystallinity of poly(3-hexylthiophene) thin films prepared by low-temperature drop casting*, *J. Appl. Polym. Sci.* **125** (2012) 2335–2341.

[51] H. Yang, S. W. LeFevre, C. Y. Ryu, and Z. Bao, *Solubility-driven thin film structures of regioregular poly(3-hexyl thiophene) using volatile solvents*, *Appl. Phys. Lett.* **90** (2007) 172116–1–3.

[52] M. Brinkmann and J.-C. Wittmann, *Orientation of regioregular poly(3-hexylthiophene) by directional solidification: A simple method to reveal the semicrystalline structure of a conjugated polymer*, *Adv. Mater.* **18** (2006) 860–863.

[53] D. Beljonne, J. Cornil, H. Sirringhaus, P. J. Brown, M. Shkunov, R. H. Friend, and J. L. Bredas, *Optical signature of delocalized polarons in conjugated polymers*, *Adv. Func. Mater.* **11** (2001) 229–234.

[54] X. M. Jiang, R. Osterbacka, O. Korovyanko, C. An, B. Horovitz, R. A. J. Janssen, and Z. V. Vardeny, *Spectroscopic studies of photoexcitations in regioregular and regiorandom polythiophene films*, *Adv. Func. Mater.* **12** (2002) 587–597.

[55] Y. Guo, X. Ma, and Z. Su, *Interfacial interactions between poly(3-hexylthiophene) and substrates*, *Macromolecules* **46** (2013) 2733–2739.

[56] D. H. Kim, Y. Jang, Y. D. Park, and K. Cho, *Layered molecular ordering of self-organized poly(3-hexylthiophene) thin films on hydrophobized surfaces*, *Macromolecules* **39** (2006) 5843–5847.

[57] J. Ficker, A. Ullmann, W. Fix, H. Rost, and W. Clemens, *Stability of polythiophene-based transistors and circuits*, *J. Appl. Phys.* **94** (2003) 2638–2641.

[58] J. Jaczewska, I. Raptis, A. Budkowski, D. Goustouridis, J. Raczkowska, M. Sanopoulou, E. Pamula, A. Bernasik, and J. Rysz, *Swelling of poly(3-alkylthiophene) films exposed to solvent vapors and humidity: Evaluation of solubility parameters*, *Synth. Metals* **157** (2007) 726–732.

[59] Y. Ohmori, M. Uchida, K. Muro, and K. Yoshino, *Effects of alkyl chain length and carrier confinement layer on characteristics of poly(3-alkylthiophene) electroluminescent diodes*, *Solid State Commun.* **80** (1991) 605–608.

[60] Z. Bao, Y. Feng, A. Dodabalapur, V. R. Raju, and A. J. Lovinger, *High-performance plastic transistors fabricated by printing techniques*, *Chemistry of Materials* **9** (1997) 1299–1301.

[61] S.-A. Chen and J.-M. Ni, *Structure/properties of conjugated conductive polymers. 1. neutral poly(3-alkythiophene)s*, *Macromolecules* **25** (1992) 6081–6089.

[62] A. Assadi, C. Svensson, M. Willander, and O. Inganäs, *Field-effect mobility of poly(3-hexylthiophene)*, *Applied Physics Letters* **53** (1988) 195–197.

[63] J. Paloheimo, H. Stubb, P. Yli-Lahti, and P. Kuivalainen, *Field-effect conduction in polyalkylthiophenes*, *Synthetic Metals* **41** (1991) 563–566.

[64] C. Dimitrakopoulos and D. Mascaro, *Organic thin-film transistors: A review of recent advances*, *IBM Journal of Research and Development* **45** (2001) 11–27.

[65] Z. Bao, A. Dodabalapur, and A. J. Lovinger, *Soluble and processable regioregular poly(3-hexylthiophene) for thin film field-effect transistor applications with high mobility*, *Applied Physics Letters* **69** (1996) 4108–4110.

[66] G. Xu, Z. Bao, and J. T. Groves, *Langmuir-Blodgett films of regioregular poly(3-hexylthiophene) as field-effect transistors*, *Langmuir* **16** (2000) 1834–1841.

[67] R. González and N. J. Pinto, *Electrospun poly(3-hexylthiophene-2,5-diyl) fiber field effect transistor*, *Synthetic Metals* **151** (2005) 275–278.

[68] S. Lee, G. D. Moon, and U. Jeong, *Continuous production of uniform poly(3-hexylthiophene) (P3HT) nanofibers by electrospinning and their electrical properties*, *J. Mater. Chem.* **19** (2009) 743–748.

[69] T. Shimomura, T. Takahashi, Y. Ichimura, S. Nakagawa, K. Noguchi, S. Heike, and T. Hashizume, *Relationship between structural coherence and intrinsic carrier transport in an isolated poly(3-hexylthiophene) nanofiber*, *Phys. Rev. B* **83** (2011) 115314–1–10.

[70] P. Vanlaeke, A. Swinnen, I. Haeldermans, G. Vanhoyland, T. Aernouts, D. Cheyns, C. Deibel, J. D'Haen, P. Heremans, J. Poortmans, and J. Manca, *P3HT/PCBM bulk heterojunction solar cells: Relation between morphology and electro-optical characteristics*, *Solar Energy Materials and Solar Cells* **90** (2006) 2150–2158.

[71] M. T. Dang, L. Hirsch, and G. Wantz, *P3HT:PCBM, best seller in polymer photovoltaic research*, *Advanced Materials* **23** (2011) 3597–3602.

[72] K. Yoshino, Y. Manda, K. Sawada, M. Onoda, and R. Sugimoto, *Anomalous dependences of luminescence of poly(3-alkylthiophene) on temperature and alkyl chain length*, *Solid State Commun.* **69** (1989) 143–146.

[73] K. C. Park and K. Levon, *Order-disorder transition in the electroactive polymer poly(3-dodecylthiophene)*, *Macromolecules* **30** (1997) 3175–3183.

[74] I. F. Perepichka, D. F. Perepichka, H. Meng, and F. Wudl, *Light-emitting polythiophenes*, *Adv. Mater.* **17** (2005) 2281–2305.

[75] W. Xu, L. Li, H. Tang, H. Li, X. Zhao, and X. Yang, *Solvent-induced crystallization of poly(3-dodecylthiophene): Morphology and kinetics*, *J. Phys. Chem. B* **115** (2011) 6412–6420.

[76] Y. Guo, , Y. Jin, and Z. Su, *Spectroscopic study of the microstructure and phase transition of regioregular poly(3-dodecylthiophene)*, *Soft Matter* **8** (2012) 2907–2914.

[77] M. L. Hammock, A. Chortos, B. C.-K. Tee, J. B.-H. Tok, and Z. Bao, *The evolution of electronic skin (e-skin): A brief history, design considerations, and recent progress*, *Advanced Materials* **25** (2013) 5997–6038.

[78] H. F. Okorn-Schmidt, *Characterization of silicon surface preparation processes for advanced gate dielectrics*, *IBM J. Res. Dev.* **43** (1999) 351–326.

[79] X. G. Zhang, *Electrochemistry of Silicon and its Oxide*. Kluwer Academic, New York, 2004.

[80] J. K. Bal and S. Hazra, *Interfacial role in room-temperature diffusion of Au into Si substrates*, *Phys. Rev. B* **75** (2007) 205411–1–6.

[81] J. K. Bal and S. Hazra, *Time-evolution growth of Ag nanolayers on differently-passivated Si(001) surfaces*, *Phys. Rev. B* **79** (2009) 155412–1–6.

[82] P. Chatterjee, S. Hazra, and H. Amenitsch, *Substrate and drying effect in shape and ordering of micelles inside CTAB-Silica mesostructured films*, *Soft Matter* **8** (2012) 2956–2964.

[83] W. Kern, *The evolution of silicon wafer cleaning technology*, *Journal of The Electrochemical Society* **137** (1990) 1887–1892.

[84] C. J. Lawrence, *The mechanics of spin coating of polymer films*, *Physics of Fluids* **31** (1988) 2786–2795.

[85] A. G. Emslie, F. T. Bonner, and L. G. Peck, *Flow of a viscous liquid on a rotating disk*, *Journal of Applied Physics* **29** (1958) 858–862.

[86] A. Acrivos, M. J. Shah, and E. E. Petersen, *On the flow of a non-Newtonian liquid on a rotating disk*, *Journal of Applied Physics* **31** (1960) 963–968.

[87] S. A. Jenekhe and S. B. Schuldt, *Coating flow of non-Newtonian fluids on a flat rotating disk*, *Industrial & Engineering Chemistry Fundamentals* **23** (1984) 432–436.

[88] D. Meyerhofer, *Characteristics of resist films produced by spinning*, *J. Appl. Phys.* **49** (1978) 3993–3997.

[89] B. T. Chen, *Investigation of the solvent-evaporation effect on spin coating of thin films*, *Polym. Eng. Sc.* **23** (1983) 399–403.

[90] J. Nielsen and D. McMorrow, *Elements of Modern X-ray Physics*. John Wiley & Sons, Ltd., 2001.

[91] J. Daillant and A. Gibaud, eds., *X-Ray and Neutron Reflectivity: Principles and Applications*. Springer, Paris, 1999.

[92] M. Tolan, *X-Ray Scattering from Soft Matter Thin Films*. Springer, 1999.

[93] D. Griffiths, *Introduction to Electrodynamics*. Prentice Hall, Upper Saddle River, New Jersey, 1999.

[94] H. Kiessig, *Interferenz von röntgenstrahlen an dünnen schichten*, *Annalen der Physik* **10** (1931) 769–788.

[95] L. G. Parratt, *Surface studies of solids by total reflection of X-rays*, *Phys. Rev.* **95** (1954) 359–369.

[96] S. K. Sinha, E. B. Sirota, S. Garoff, and H. B. Stanley, *X-ray and neutron scattering from rough surfaces*, *Phys. Rev. B* **38** (Aug, 1988) 2297–2311.

[97] V. Holý, J. Kuběna, I. Ohlídal, K. Lischka, and W. Plotz, *X-ray reflection from rough layered systems*, *Phys. Rev. B* **47** (Jun, 1993) 15896–15903.

[98] J. Basu and M. Sanyal, *Ordering and growth of Langmuir-Blodgett films: X-ray scattering studies*, *Physics Reports* **363** (2002) 1–84.

[99] J. R. Levine, J. B. Cohen, Y. W. Chung, and P. Georgopoulos, *Grazing-incidence small-angle X-ray scattering: New tool for studying thin film growth*, *Journal of Applied Crystallography* **22** (1989) 528–532.

[100] W. C. Marra, P. Eisenberger, and A. Y. Cho, *X-ray total-external-reflection— Bragg diffraction: A structural study of the GaA-Al Interface*, *Journal of Applied Physics* **50** (1979) 6927–6933.

[101] I. K. Robinson and D. J. Tweet, *Surface X-ray diffraction*, *Rep. Prog. Phys.* **55** (1992) 599–651.

[102] R. Feidenhans'l, *Surface structure determination by X-ray diffraction*, *Surface Science Reports* **10** (1989) 105–188.

[103] G. Renaud, R. Lazzari, and F. Leroy, *Probing surface and interface morphology with grazing incidence small angle X-ray scattering*, *Surface Science Reports* **64** (2009) 255–380.

[104] D. Thiaudière, O. Proux, J.-S. Micha, C. Revenant, J.-R. Regnard, and S. Lequien, *Structural and morphological studies of Co/SiO_2 discontinuous multilayers* , *Physica B: Condensed Matter* **283** (2000) 114–118.

[105] F. Gonella, E. Cattaruzza, G. Battaglin, F. D'Acapito, C. Sada, P. Mazzoldi, C. Maurizio, G. Mattei, A. Martorana, A. Longo, and F. Zontone, *Double implantation in silica glass for metal cluster composite formation: A study by synchrotron radiation techniques*, *Journal of Non-Crystalline Solids* **280** (2001) 241–248.

[106] M. Schmidbauer, T. Wiebach, H. Raidt, M. Hanke, R. Köhler, and H. Wawra, *Ordering of self-assembled $Si_{1-x}Ge_x$ islands studied by grazing incidence small-angle X-ray scattering and atomic force microscopy*, *Phys. Rev. B* **58** (1998) 10523–10531.

[107] J. Stangl, V. Holý, P. Mikulík, G. Bauer, I. Kegel, T. H. Metzger, O. G. Schmidt, C. Lange, and K. Eberl, *Self-assembled carbon-induced germanium quantum dots studied by grazing-incidence small-angle X-ray scattering*, *Applied Physics Letters* **74** (1999) 3785–3787.

[108] S. V. Roth, G. Herzog, V. Körstgens, A. Buffet, M. Schwartzkopf, J. Perlich, M. M. A. Kashem, R. Döhrmann, R. Gehrke, A. Rothkirch, K. Stassig, W. Wurth, G. Benecke, C. Li, P. Fratzl, M. Rawolle, and P. Müller-Buschbaum, *In situ observation of cluster formation during nanoparticle solution casting on a colloidal film*, *J. Phys.: Condens. Matter* **23** (2011) 254208.

[109] S. Joshi, P. Pingel, S. Grigorian, T. Panzner, U. Pietsch, D. Neher, M. Forster, and U. Scherf, *Bimodal temperature behavior of structure and mobility in high molecular weight P3HT thin films*, *Macromolecules* **42** (2009) 4651–4660.

[110] P. Müller-Buschbaum, J. Gutmann, M. Stamm, R. Cubitt, S. Cunis, G. von Krosigk, R. Gehrke, and W. Petry, *Dewetting of thin polymer-blend films examined with GISAS*, *Physica B: Condensed Matter* **283** (2000) 53–59.

[111] Z. Di, D. Posselt, D.-M. Smilgies, R. Li, M. Rauscher, I. I. Potemkin, and C. M. Papadakis, *Stepwise swelling of a thin film of lamellae-forming poly(styrene-b-butadiene) in cyclohexane vapor*, *Macromolecules* **45** (2012) 5185–5195.

[112] S. Hazra, *Morphology and structure of Gold-Lithium niobate thin film: A laboratory source X-ray scattering study*, *Appl. Surf. Sci.* **253** (2006) 2154–2157.

[113] A. Hofmann, *The Physics of Synchrotron Radiation*. Cambridge University Press, New York, 2004.

[114] P. Chatterjee and S. Hazra, *The hydrophilic/hydrophobic nature of a Cl-terminated Si surface*, *Soft Matter* **9** (2013) 9799–9806.

[115] P. Chatterjee and S. Hazra, *Time evolution of a Cl-terminated Si surface at ambient conditions*, *J. Phys. Chem. C* **118** (2014) 11350–11356.

[116] G. Binnig and H. Rohrer, *Scanning tunneling microscopy*, *Surface Science* **126** (1983) 236–244.

[117] G. Binnig, H. Rohrer, C. Gerber, and E. Weibel, *Surface studies by scanning tunneling microscopy*, *Phys. Rev. Lett.* **49** (1982) 57–61.

[118] C. J. Chen, *Introduction to Scanning Tunneling Microscopy*. Oxford University Press, New York, 1993.

[119] R. Wiesendanger, *Scanning Probe Microscopy and Spectroscopy—Methods and Applications*. Cambridge University Press, United Kingdom, 1994.

[120] G. Binnig, C. F. Quate, and C. Gerber, *Atomic force microscope*, *Phys. Rev. Lett.* **56** (1986) 930–933.

[121] P. Eaton and P. West, *Atomic Force Microscopy*. Oxford University Press, 2010.

[122] G. Binnig, C. Gerber, E. Stoll, T. R. Albrecht, and C. F. Quate, *Atomic resolution with atomic force microscope*, *Europhysics Letters* **3** (1987) 1281.

[123] E. Meyer, *Atomic force microscopy*, *Progress in Surface Science* **41** (1992) 3–49.

[124] N. Jalili and K. Laxminarayana, *A review of atomic force microscopy imaging systems: Application to molecular metrology and biological sciences*, *Mechatronics* **14** (2004) 907–945.

[125] Y. Martin, C. C. Williams, and H. K. Wickramasinghe, *Atomic force microscope-force mapping and profiling on a sub 100-Å scale*, *Journal of Applied Physics* **61** (1987) 4723–4729.

[126] M. Senthilkumar, N. Sahoo, S. Thakur, and R. Tokas, *Characterization of microroughness parameters in gadolinium oxide thin films: A study based on extended power spectral density analyses*, *Applied Surface Science* **252** (2005) 1608–1619.

[127] M. Bass, ed., *Handbook of Optics, Volume 1: Fundamentals, Techniques and Design*. McGraw-Hill, Inc., USA, 1995.

[128] H. Tian, G. Ribeill, C. Xu, C. E. Reece, and M. J. Kelley, *A novel approach to characterizing the surface topography of niobium superconducting radio frequency (SRF) accelerator cavities* , *Applied Surface Science* **257** (2011) 4781–4786.

[129] C. Xu, H. Tian, C. E. Reece, and M. J. Kelley, *Topographic power spectral density study of the effect of surface treatment processes on niobium for superconducting radio frequency accelerator cavities*, *Phys. Rev. ST Accel. Beams* **15** (2012) 043502–1–18.

[130] C. N. R. Rao, *Ultraviolet and Visible Spectroscopy—Chemical Applications*. Butterworth & Co. (Publisbers) Ltd., London, 1961.

[131] B. J. Clark, T. Frost, and M. A. Russell, eds., *UV Spectroscopy : Techniques, Instrumentation, Data Handling*. Chapman & Hall, London, 1993.

[132] M. Kasha, *Energy transfer mechanisms and the molecular exciton model for molecular aggregates*, *Radiation Research* **20** (1963) 55–70.

[133] K. S. Schmitz, *An Introduction to Dynamic Light Scattering by Macromolecules*. Academic Press Inc., San Diego, 1990.

[134] B. J. Berne and R. Pecora, *Dynamic Light Scattering—with applications to Chemistry, Biology and Physics*. John Wiley and Sons, Inc., New York, 1975.

[135] S. Lee, J. Y. Lee, and H. Lee, *Solvent effects on the characteristics of conductive and luminescent polymers*, *Synthetic Metals* **101** (1999) 248–249.

[136] C.-K. Shin and H. Lee, *Effect of alkyl side-chain length and solvent on the luminescent characteristics of poly(3-n-alkylthiophene)*, *Synthetic Metals* **140** (2004) 177–181.

[137] M. Al-Ibrahim, O. Ambacher, S. Sensfuss, and G. Gobsch, *Effects of solvent and annealing on the improved performance of solar cells based on poly(3-hexylthiophene): Fullerene*, *Applied Physics Letters* **86** (2005) 201120–1–3.

[138] W.-H. Baek, H. Yang, T.-S. Yoon, C. Kang, H. H. Lee, and Y.-S. Kim, *Effect of P3HT:PCBM concentration in solvent on performances of organic solar cells*, *Solar Energy Materials and Solar Cells* **93** (2009) 1263–1267.

[139] C. Kwong, A. Djurišić, P. Chui, K. Cheng, and W. Chan, *Influence of solvent on film morphology and device performance of poly(3-hexylthiophene):TiO2 nanocomposite solar cells*, *Chemical Physics Letters* **384** (2004) 372–375.

[140] B. Meredig, A. Salleo, and R. Gee, *Ordering of poly(3-hexylthiophene) nanocrystallites on the basis of substrate surface energy*, *ACS Nano* **3** (2009) 2881–2886.

[141] D. M. DeLongchamp, B. M. Vogel, Y. Jung, M. C. Gurau, C. A. Richter, O. A. Kirillov, J. Obrzut, D. A. Fischer, S. Sambasivan, L. J. Richter, and E. K. Lin, *Variations in semiconducting polymer microstructure and hole mobility with spin-coating speed*, *Chem. Mater.* **17** (2005) 5610–5612.

[142] I. Roy and S. Hazra, *Poor solvent and thermal annealing induced ordered crystallites in poly(3-dodecylthiophene) films*, *RSC Adv.* **5** (2015) 665–675.

[143] P. J. Brown, D. S. Thomas, A. Kohler, J. S. Wilson, J.-S. Kim, C. M. Ramsdale, H. Sirringhaus, and R. H. Friend, *Effect of interchain interactions on the absorption and emission of poly(3-hexylthiophene)*, *Phys. Rev. B* **67** (2003) 064203–1–16.

[144] J. Clark, C. Silva, R. H. Friend, and F. C. Spano, *Role of intermolecular coupling in the photophysics of disordered organic semiconductors: Aggregate emission in regioregular polythiophene*, *Phys. Rev. Lett.* **98** (2007) 206406–1–4.

[145] I. Roy and S. Hazra, *Solvent dependent ordering of poly(3-dodecylthiophene) in thin films*, *Soft Matter* **11** (2015) 3724–3732.

[146] L. Y. Wong, R. Q. Png, F. B. S. Silva, L. L. Chua, D. V. M. Repaka, S. Chen, X. Y. Gao, L. Ke, S. J. Chua, A. T. S. Wee, and P. K. H. Ho, *Interplay of processing, morphological order, and charge-carrier mobility in polythiophene thin films deposited by different methods: Comparison of spin-cast, drop-cast, and inkjet-printed films*, *Langmuir* **26** (2010) 15494–15507.

[147] J. Catalán, *Toward a generalized treatment of the solvent effect based on four empirical scales: Dipolarity (sdp, a new scale), polarizability (sp), acidity (sa), and basicity (sb) of the medium*, *J. Phys. Chem. B* **113** (2009) 5951–5960.

[148] G. M. Newbloom, S. M. Hoffmann, A. F. West, M. C. Gile, P. Sista, H.-K. C. Cheung, C. K. Luscombe, J. Pfaendtner, and L. D. Pozzo, *Solvatochromism and conformational changes in fully dissolved poly(3-alkylthiophene)s*, *Langmuir* **31** (2015) 458–468.

[149] Y. Fu, C. Lin, and F.-Y. Tsai, *High field-effect mobility from poly(3-hexylthiophene) thin-film transistors by solvent vapor-induced reflow*, *Org. Electr.* **10** (2009) 883–888.

[150] N. Kiriy, E. Jähne, H.-J. Adler, M. Schneider, A. Kiriy, G. Gorodyska, S. Minko, D. Jehnichen, P. Simon, A. A. Fokin, and M. Stamm, *One-dimensional aggregation of regioregular polyalkylthiophenes*, *Nano Lett.* **3** (2003) 707–712.

[151] Y. D. Park, H. S. Lee, Y. J. Choi, D. Kwak, J. H. Cho, S. Lee, and K. Cho, *Solubility-induced ordered polythiophene precursors for high-performance organic thin-film transistors*, *Advanced Functional Materials* **19** (2009) 1200–1206.

[152] Z. Yu, H. Yan, K. Lu, Y. Zhang, and Z. Wei, *Self-assembly of two-dimensional nanostructures of linear regioregular poly(3-hexylthiophene)*, *RSC Adv.* **2** (2012) 338–343.

[153] M. Chang, D. Choi, B. Fu, and E. Reichmanis, *Solvent based hydrogen bonding: Impact on poly(3-hexylthiophene) nanoscale morphology and charge transport characteristics*, *ACS Nano* **7** (2013) 5402–5413.

[154] K. Yazawa, Y. Inoue, T. Yamamoto, and N. Asakawa, *Twist glass transition in regioregulated poly(3-alkylthiophene)*, *Phys. Rev. B* **74** (2006) 094204–1–12.

[155] S. Malik and A. K. Nandi, *Crystallization mechanism of regioregular poly(3-alkylthiophene)s*, *J. Polym. Sci. B* **40** (2002) 2073–2085.

[156] Y. Takizawa, T. Shimomura, and T. Miura, *Simulation study of the initial crystallization processes of poly(3-hexylthiophene) in solution: Ordering dynamics of main chains and side chains*, *J. Phys. Chem. B* **117** (2013) 6282–6289.

[157] W. Dierckx, W. D. Oosterbaan, J.-C. Bolsee, W. Maes, D. Vanderzande, and J. Manca, *Poly(3-alkylthiophene) nanofibers for optoelectronic devices*, *J. Mater. Chem. C* **2** (2014) 5730–5746.

[158] A. A. Rudov, E. S. Patyukova, I. V. Neratova, P. G. Khalatur, D. Posselt, C. M. Papadakis, and I. I. Potemkin, *Structural changes in lamellar diblock copolymer thin films upon swelling in nonselective solvents*, *Macromolecules* **46** (2013) 5786–5795.

[159] T. Kim, J. Hwang, W. Hwang, J. Huh, H.-C. Kim, S. Kim, J. Hong, E. Thomas, and C. Park, *Hierarchical ordering of block copolymer nanostructures by solvent annealing combined with controlled dewetting*, *Advanced Materials* **20** (2008) 522.

[160] E. J. W. Crossland, K. Rahimi, G. Reiter, U. Steiner, and S. Ludwigs, *Systematic control of nucleation density in poly(3-hexylthiophene) thin films*, *Advanced Functional Materials* **21** (2011) 518–524.

[161] B. A. Gregg, *Evolution of photophysical and photovoltaic properties of perylene bis(phenethylimide) films upon solvent vapor annealing*, *The Journal of Physical Chemistry* **100** (1996) 852–859.

[162] G. Lu, L. Li, and X. Yang, *Achieving perpendicular alignment of rigid polythiophene backbones to the substrate by using solvent-vapor treatment*, *Advanced Materials* **19** (2007) 3594–3598.

[163] V. Ruiz, P. G. Nicholson, S. Jollands, P. A. Thomas, J. V. Macpherson, , and P. R. Unwin, *Molecular ordering and 2d conductivity in ultrathin poly(3-hexylthiophene)/gold nanoparticle composite films*, *The Journal of Physical Chemistry B* **109** (2005) 19335–19344.

[164] P. G. Nicholson, V. Ruiz, J. V. Macpherson, and P. R. Unwin, *Enhanced visible photoluminescence in ultrathin poly(3-hexylthiophene) films by incorporation of Au nanoparticles*, *Chem. Commun.* (2005) 1052–1054.

PUBLICATIONS

1. **I. Roy** and S. Hazra, *Poor solvent and thermal annealing induced ordered crystallites in poly(3-dodecylthiophene) films*, *RSC Adv.* **5** (2015) 665–675.

2. **I. Roy** and S. Hazra, *Solvent dependent ordering of poly(3-dodecylthiophene) in thin films*, *Soft Matter* **11** (2015) 3724–3732.

3. **I. Roy** and S. Hazra, *Structural modifications of spin-cast poly(3-dodecylthiophene) films under solvent vapor and thermal annealing*, *(Manuscript in progress)*.